

Design and Fabrication of Microfluidic Valves Using poly(*N*-isopropylacrylamide)

by

Nathan Edward Reticker-Flynn

B.S. Mechanical Engineering
Tufts University, 2006

SUBMITTED TO THE DEPARTMENT OF MECHANICAL ENGINEERING IN PARTIAL
FULFILLMENT OF THE REQUIREMENTS FOR THE DEGREE OF

MASTER OF SCIENCE IN MECHANICAL ENGINEERING
AT THE
MASSACHUSETTS INSTITUTE OF TECHNOLOGY
JUNE 2008

©2008 Massachusetts Institute of Technology.
All rights reserved.

Signature of Author: _____

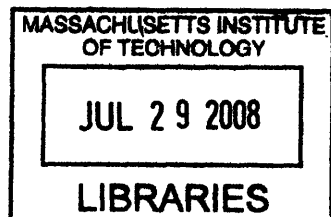
Department of Mechanical Engineering
May 21, 2008

Certified by: _____

Sang-Gook Kim
Associate Professor of Mechanical Engineering
Thesis Supervisor

Accepted by: _____

Lallit Anand
Chairman, Committee on Graduate Students
Department of Mechanical Engineering



ARCHIVES

Design and Fabrication of Microfluidic Valves Using poly(*N*-isopropylacrylamide)

by

Nathan Edward Reticker-Flynn

Submitted to the Department of Mechanical Engineering on May 21, 2008 in Partial Fulfillment of the Degree of Master of Science in Mechanical Engineering

Abstract

A compact printable microfluidic valve composed of poly(*N*-isopropylacrylamide) has been designed, fabricated, and tested. The design of the valve consists of filling microwells with poly(NIPAAm) and bonding PDMS channels above them. This filling is achieved using thermal inkjet printing of a prepolymer solution and subsequent polymerization using UV irradiation. When the gel is swollen, it blocks flow from passing through the channel. Upon heating, the gel shrinks and allows flow in the channel.

Poly(NIPAAm) is a thermosensitive hydrogel that exhibits an inverse temperature expansion behavior. When the temperature of the swollen gel is raised above a lower critical solution temperature (LCST) of approximately 32°C, the gel becomes hydrophobic. This change in hydrophobicity results in expulsion of the water molecules from within the hydrogel network, thus resulting in shrinking of the gel. By adding magnetic nanoparticles to the hydrogel and exposing it to an external magnetic field, volumetric change of the hydrogel can be locally and externally induced. External heating of the magnetic nanoparticles, however, is not included in this thesis.

In order to ensure shrinkage that is predictable in favor of flow control, microanchor structures have been designed, modeled, and fabricated at the bottom of the microwells. These microanchors hold the poly(NIPAAm) at the bottom of the plug such that the shrinkage of the gel always acts to open the flow channel at the top yielding a minimum pressure drop. Design decisions were made using the principles of Axiomatic Design in order to minimize the response time and pressure drops in the valve. Modeling of the underlying mechanisms is described along with the application of these models to the final device.

Results of fabrication suggest the feasibility while also eliciting possible improvements to the fabrication process. Profilometry measurements of the swollen and shrunken valves reveal flow control operation as intended. Additionally, design and modeling of magnetic heating using mixed-in nanoparticles is presented. A fabrication plan designed to include this mechanism is proposed.

Thesis Supervisor: Sang-Gook Kim

Title: Associate Professor of Mechanical Engineering

Acknowledgments

This thesis would not have been possible to produce were it not for the assistance, guidance, and support of a variety of individuals. While I cannot possibly thank all of the individuals that have helped me over the past two years, I will try to thank at least the most prominent ones.

The support and guidance of my advisor, Prof. Kim, has been essential to the completion of this project and to my growth as an engineer. I have learned a great deal in his lab and owe him a lot of thanks for the opportunities that he has provided me. Additionally, the support of Dr. Hyungwoo Lee has been very helpful throughout the duration of this project.

I would also like to thank Soohyung Kim for helping me image the magnetic nanoparticles using the TEM and Stephen Bathurst for teaching me how to use the HP POEM system. Additionally, I would like to thank my other past and current labmates Arman Hajati, Zach Traina, Dr. Michael DeVolder, Heon Ju Lee, and Jordan Peck for their useful discussions and general friendship.

A variety of other people lent me assistance throughout this project to whom I am much indebted. Shahriar Khushrushahi has helped me tremendously on this project from the first days by providing me with many resources on NIPAAm and magnetic heating along with supplies when I needed them. In general, I would like to thank all of the MTL staff and in particular Kris Payer for his useful discussions on etching glass, and Kurt Broderick for teaching me how to do virtually everything I know about micromachining. His guidance, utility, and friendliness are what keep the MTL running as smoothly as it does.

I would like to thank my family and friends for their unwavering support. The love and support that I have received from Mom, Dad, Julia, and Emily has been essential to my success in my studies and in life in general. Finally, I owe thanks to my idols both in the scientific and non-scientific worlds for giving me inspiration: Albert Einstein, Richard Feynman, G.I. Taylor, Paul Pierce, Manny Ramirez, and Bill Belichick.

Table of Contents

Abstract	3
Acknowledgments	4
Table of Contents	5
Glossary of Symbols	7
List of Figures	10
1. Introduction	12
1.1. Motivation and Device Design.....	12
1.2. Microfluidics.....	16
1.2.1. History.....	16
1.2.2. Scaling Benefits.....	19
1.2.3. Valves in Microfluidics.....	21
1.3. Hydrogels.....	24
1.3.1. Background of Hydrogels.....	24
1.3.2. Theory of Swelling.....	26
1.4. Magnetic Nanoparticles.....	27
2. Background Modeling	30
2.1. Solid and Fluid Mechanics.....	30
2.1.1. Fluid Dynamics: Navier-Stokes and Low Reynolds Number Flows.....	30
2.1.1.1. Navier-Stokes.....	30
2.1.1.2. Viscous Flows in Microfluidics.....	33
2.1.2. Mechanics and Kinetics of Gels.....	37
2.1.3. Volume Phase Transitions in Gels Exhibiting LCST Behavior.....	40
2.1.4. Flow Through Porous Media.....	47
2.1.5. Compaction of Porous Media.....	53
2.2. Magnetic Heating.....	58
2.2.1. Heat Generation by Magnetic Particles.....	58
2.2.1.1. Power Dissipation.....	58
2.2.1.2. Relaxation Time Constants.....	60
2.2.2. Magnetic Field Generation Using a Planar MEMS Magnetic Coil.....	62
2.2.2.1. On-Axis Magnetic Field Strength.....	63
2.2.2.2. Off-Axis Magnetic Field Strength.....	68
2.3. Heat Transfer.....	72
2.3.1. General Heat Transfer Mechanisms.....	72
2.3.2. Heat Transfer in the Hydrogel.....	74
2.3.3. Heat Transfer from Joule Heating of the Magnetic Coil.....	75
2.4. Rate Limiting Mechanisms and Time Response of Swelling.....	80
2.5. Lumped Element Modeling.....	82
2.5.1. Background of Lumped Element Modeling.....	82
2.5.2. The Fluidic Domain.....	84
2.5.3. The Thermal Domain.....	85
2.5.4. Viscoelasticity as a Lumped Element System.....	88
2.5.5. Coupling.....	89

2.6. Oxygen inhibition.....	90
3. Systems Approach to the Design of the Device.....	95
3.1. Principles of Axiomatic Design.....	95
3.2. Top Level Functional Requirements.....	97
3.3. Original Design.....	98
3.4. Further Decomposition and Intermediate Designs.....	100
3.4.1. Redefining DP_3	100
3.4.2. Second Level of Decomposition.....	101
3.4.3. Third Level of Decomposition.....	103
3.4.4. Intermediate Valve Designs and Reformulation of $DP_{1,1}$	105
3.4.5. Decoupling the Magnetic Field FRs and DPs.....	107
3.4.6. Manufacturing FRs and DPs.....	110
3.5. Complexity and Predictable Shrinking.....	111
3.6. Final Design.....	112
4. Device Modeling.....	116
4.1. Oxygen Inhibition.....	116
4.2. Fluid Flow.....	117
4.2.1. Analytical Solutions.....	117
4.2.2. CFD Solutions.....	118
4.2.3. Stresses on the Gel and Anchors.....	120
4.3. Magnetic Heating.....	123
4.3.1. Magnetic Nanoparticles.....	123
4.3.2. MEMS Magnetic Coil.....	124
5. Fabrication.....	130
5.1. Original Design Fabrication.....	130
5.2. Final Device Fabrication.....	136
5.2.1. Process Flow.....	136
5.2.2. Fabrication Details and Results.....	139
5.2.2.1. Wet Etching of Glass.....	139
5.2.2.2. Printing.....	145
5.2.2.3. Polymerization.....	151
5.2.2.4. Channel Bonding.....	153
5.2.3. Prepolymer Solutions.....	154
6. Experimental Results and Discussion.....	156
6.1. Original Design.....	156
6.2. Revised Design.....	157
7. Future Work and Design Iterations.....	164
7.1. Magnetic Nanoparticles.....	164
7.2. Alternative Fabrication Process.....	165
7.3. Tests in Applications.....	168
8. Conclusion.....	170
Appendices.....	172
Appendix 1 – In-Channel Polymerization.....	173
Appendix 2 – Fe ₃ O ₄ Nanoparticle Data Sheet.....	176
Appendix 3 – 2,2-Dimethoxy-2-phenylacetophenone Data.....	177
Appendix 4 – MJB3 Custom Chuck for Aligning PDMS/Glass Slide Structures.....	179

References.....180

Glossary of Symbols

- A – Area (2.5.3), System Matrix (3.1, 3.4)
 a – Off Axis Distance of Gel from Coil (2.2.2.2)
 B – Magnetic Flux Density (2.2.1.1, 2.2.2.1, 2.2.2.2)
 C – Concentration (2.1.1.1)
 C_{O_2} – Concentration of Oxygen (2.6)
 C_T – Thermal Capacitance (2.5.3)
 C_{wafer} – Thermal Capacitance of Wafer (2.5.3, 4.3.2)
 C_{wall} – Concentration of Oxygen at Channel Wall (2.6)
 c_p – Specific Heat (2.3.1, 2.3.2, 2.3.3, 2.5.3)
 D – Coefficient of Mass Diffusion (2.1.1.1, 2.4, 2.6, 4.1, 5.1)
 D_T – Thermal Diffusivity (2.3.1, 2.3.2, 2.3.3, 2.4)
 d – Distance between the Plane of the Coil and the Gel (2.2.2.1, 2.2.2.2, 3.4.5, 4.3.2)
 DP – Design Parameter (3.1, 3.2, 3.4, 3.6)
 E – Electric Field (2.2.2.1)
 e – Effort (2.5.1)
 F – Free Energy (2.1.3)
 F_{12} – Radiation Form Factor (2.5.3)
 F_{el} – Free Energy of Elasticity (2.1.3)
 $F_{hydrophobic}$ – Free Energy of Hydrophobic Interactions (2.1.3)
 F_M – Free Energy of Mixing (2.1.3)
 f – Friction Factor (2.1.2), Number of Ionic Groups between Crosslinks (2.1.3),
Frequency (2.2.1.1, 4.3.1), Flow (2.5.1)
 FR – Functional Requirement (3.1, 3.2, 3.4)
 G – Gibbs Free Energy (1.3.2), Shear Modulus (2.1.2, 2.1.5)
 G – Gravitation/Body Acceleration (2.1.1.1)
 H – Enthalpy (1.3.2, 2.1.3), Longitudinal Modulus (2.1.5), Magnetic Field Strength
(2.2.1.1, 2.2.2.1, 3.4.5, 4.3.1), Transfer Function for Thermal Circuit (2.5.3)
 H_M – Enthalpy of Mixing (2.1.3)
 h – Channel Height (2.1.1.2, 2.1.4, 2.5.2, 4.2.1), Convective Heat Transfer Coefficient
(2.3.1, 2.5.3)
 I – Electric Current (2.2.2.1, 2.2.2.2, 2.3.3, 2.5.3, 3.4.5, 4.3.2), Information Content (3.1)
 J – Electric Current Density (2.2.2.1, 2.5.3)
 K – Hydraulic Permeability (2.1.4, 2.1.5)
 k – Reaction Rate Constant (2.6, 4.1, 5.1)
 k_B – Boltzmann Constant (2.1.3, 2.2.1.2, 2.6)
 L – Characteristic Length (1.2.2, 2.1.4, 2.1.5, 2.3.2, 2.4, 2.5.3, 2.6, 5.1), Channel Length
(2.5.2, 4.2.1)
 L_c – Length of Magnetic Coil (4.3.2)
 L_p – Penetration Length of Oxygen in Prepolymer (2.6, 4.1)
 M – Magnetization
 N – Number of Turns in Magnetic Coil (2.2.2.1, 2.2.2.2, 3.4.5, 4.3.2)
 N_A – Avogadro's Number (2.6)
 N_x – Degree of Polymerization (2.1.3)
 P – Pressure (2.1.1.2, 2.5.2, 4.2.1), Power (2.2.1.1, 4.3.1), Probability of Success (3.1)

p – Pressure (2.1.1.1, 2.1.1.2, 2.1.4, 2.1.5), Generalized Momentum (2.5.1)
 Q – Volume flow rate (2.1.1.2, 2.1.4, 2.5.2, 4.2.1), Heat (2.2.1.1, 2.3.1)
 q – Generalized Displacement (2.5.1)
 q'' – Heat Flux (2.3.1, 2.5.3)
 R – Generation of Mass (2.1.1.1, 2.6), Radius of Magnetic Coil (2.2.2.1, 2.2.2.2, 3.4.5, 4.3.2), Electrical Resistance (2.3.3, 2.5.3), Gas Constant (2.6)
 R_{air} – Thermal Resistance of Air (2.5.3, 4.3.2)
 R_e – Electrical Resistance (4.3.2)
 R_{fluid} – Fluidic Resistance (2.1.4)
 R_H – Hydrodynamic Radius (2.2.1.2)
 R_{Pois} – Fluidic Resistance for Poiseuille Flow (2.5.2)
 R_{w-h} – Fluidic Resistance when $w \sim h$ (2.5.2)
 R_{wafer} – Thermal Resistance of Wafer (2.5.3, 4.3.2)
 R_T – Thermal Resistance (2.5.3)
 Re – Reynolds Number (1.2.2)
 r – Solute Radius (2.6)
 r_{coil} – Radial Location on Coil (2.2.2.1, 2.2.2.2)
 S – Entropy (1.3.2, 2.1.3)
 S_M – Entropy of Mixing (2.1.3)
 s – Laplace Transform of Time Derivative (2.5.3)
 T – Temperature (1.3.2, 2.1.3, 2.2.1.2, 2.3.1, 2.3.2, 2.3.3, 2.5.3, 2.6)
 t – Time (2.1.1.1, 2.1.5, 2.2.1.1, 2.2.2.1, 2.3.1, 2.3.3, 2.6)
 t_w – Wafer Thickness (2.3.3, 4.3.2)
 \tilde{t} – Nondimensional Time (2.1.1.1)
 U – Velocity (1.2.2, 2.1.4, 2.1.5), Energy (2.2.1.1)
 u – Displacement of Solid (2.1.5)
 V – Electrical Potential (2.5.3)
 V_H – Hydrodynamic Volume (2.2.1.2)
 \underline{v} – Velocity (2.1.1.1, 2.1.4)
 \underline{v}_s – Velocity of Solid (2.1.5)
 \tilde{v} – Nondimensional Velocity (2.1.1.1)
 v_1 – Molar Volume of Solvent (2.1.3)
 v_u – Molar Volume of Monomer Unit (2.1.3)
 ∇ – Volume (2.3.3, 2.5.3)
 W – Work (2.2.1.1)
 w – Channel Width (2.1.1.2, 2.1.4, 2.5.2, 4.2.1)
 w_c – Width of Magnetic Coil (4.3.2)
 Z_{eq} – Equivalent Impedance (2.5.3)

α – Angle between Axis and Position Vector (2.2.2.1)
 α_R – Thermal Coefficient of Resistance (2.3.3)
 χ – Flory Interaction Parameter (2.1.3), Magnetic Susceptibility (2.2.1.1, 4.3.1)
 ϵ – Emissivity (2.3.1)
 ϵ_0 – Electrical Permittivity of Free Space (2.2.2.1)
 ϵ_{ij} – Strain Tensor (2.1.5)
 δ_{ij} – Kronecker Delta (2.1.5)

κ – Bulk Modulus (2.1.2, 2.1.5), Anisotropy Constant (2.2.1.2), Thermal Conductivity (2.3.1, 2.3.2, 2.5.3)
 λ – 2nd Lamé Coefficient (2.1.5)
 μ – Dynamic Viscosity (1.2.2, 2.1.1.1, 2.1.1.2, 2.1.4, 2.5.2, 2.6, 4.2.1), Chemical Potential (2.1.3), Magnetic Permeability (2.2.2.1, 2.2.2.2)
 μ_0 – Magnetic Permeability of Free Space (2.2.1.1, 2.2.2.1, 2.2.2.2, 4.3.1)
 μ_{el} – Chemical Potential from Elasticity (2.1.3)
 η – Dynamic Fluid Viscosity (2.2.1.2)
 Π – Osmotic Pressure (2.1.3)
 Π_M – Osmotic Pressure from Mixing (2.1.3)
 Π_{el} – Osmotic Pressure from Elasticity (2.1.3)
 Π_{ion} – Osmotic Pressure from Ionic Groups (2.1.3)
 ϕ – Volume Fraction (2.1.2)
 ω – Angular Frequency (2.2.1.1)
 ρ – Mass Density (1.2.2, 2.3.1, 2.3.2, 2.3.3, 2.5.3), Fraction of Monomer Units Connected via Crosslinks (2.1.3)
 ρ_e – Electric Charge Density (2.2.2.1)
 ρ_t – Fraction of Chains with Crosslinks at only One End
 σ_e – Electrical Conductivity (2.5.3)
 $\sigma_{ij}, \underline{\underline{\sigma}}$ – Stress Tensor (2.1.5)
 σ_{SB} – Stefan-Boltzmann Constant (2.3.1, 2.5.3)
 τ – Characteristic Time (2.1.2, 2.3.2), Time Constant (2.2.1.1, 2.2.1.2, 4.3.1)
 τ_B – Time Constant of Brownian Relaxation (2.2.1.2)
 τ_{cond} – Characteristic Time of Heat Conduction (2.4)
 τ_N – Time Constant of Néel Relaxation (2.2.1.2)
 τ_{shrink} – Characteristic Time of Shrinking due to Mass Diffusion (2.4)

List of Figures

- 1.1 – Template design for valves
- 1.2 – Valve design concept
- 1.3 – Fabrication of channels using soft lithography
- 1.4 – Interfaces between miscible fluids
- 1.5 – Controlled microfluidic interfaces
- 1.6 – Various early microfluidic valves
- 1.7 – Different types of common microfluidic valves
- 1.8 – Quake valves
- 1.9 – Large-scale integration of Quake valves
- 1.10 – Unique patterns exhibited by gels
- 1.11 – Chemical structure of NIPAAm monomer
- 1.12 Heating of hydrogels with magnetic nanoparticles
- 1.13 – Length changes in cylindrical poly(NIPAAm) rods due to heating from nanoparticles
- 2.1 – Velocity profile for Poiseuille flow
- 2.2 – Swelling of hydrogels in the presence of water
- 2.3 – Diffusion coefficient of various poly(NIPAAm) gels as a function of temperature
- 2.4 – Discontinuous volume phase transitions in poly(NIPAAm)
- 2.5 – Volume phase transition in nonionic poly(NIPAAm)
- 2.6 – Flow through a porous gel spanning the width of a channel
- 2.7 – Velocity profile of flow through porous media
- 2.8 – Compaction of porous media
- 2.9 – Dependence of nanoparticle heat generation on size and frequency
- 2.10 – In-plane magnetic coil geometry
- 2.11 – 3D magnetic coil geometry
- 2.12 – Geometry for determining cross-products in coil
- 2.13 – 3D off-axis magnetic coil geometry
- 2.14 – In-plane off-axis magnetic coil geometry
- 2.15 – Techniques for modeling heat transfer from coil
- 2.16 – Time response of heat transport and mass transport in poly(NIPAAm)
- 2.17 – Circuit representation of lumped element model of the thermal domain
- 2.18 – Lumped element model for viscoelastic solids
- 2.19 – Relationships between the various domains of the overall system
- 2.20 – Balance of reaction rates in polymerization
- 2.21 – Oxygen concentration as a function of distance from the wall
- 3.1 – Stages of fabrication of original design
- 3.2 – poly(NIPAAm) valves created by photopatterning in PDMS channels
- 3.3 – Intermediate design principle
- 3.4 – Various valve design that satisfy $DP_{1,1,1}$
- 3.5 – Dependence of magnetic field strength on increasing n and R for a constant value of R/n
- 3.6 – Unpredictability of position of shrunken gel
- 3.7 – 3D views of valve design

- 3.8 – Cross-sectional view of valve operation
- 4.1 – Oxygen inhibition layer
- 4.2 – CFD velocity distributions around the open valve
- 4.3 – CFD pressure distributions across the open valve
- 4.4 – CFD pressure on poly(NIPAAm) plug
- 4.5 – Adhesion forces of various evaporated metals on glass
- 4.6 – FEA analysis of the stresses on the gold film
- 4.7 – Step response of thermal circuit
- 4.8 – Dependencies of magnetic field strength on the various parameters
- 4.9 – Relative magnetic field strength as a function of distance off axis
- 5.1 – Fabrication process for the original design
- 5.2 – Valves fabricated using the original valve design
- 5.3 – Polymerization of poly(NIPAAm) in a rectangular glass capillary
- 5.4 – Heating poly(NIPAAm) in channels
- 5.5 – Aspect ratio problems in PDMS bonding
- 5.6 – Process flow for cleanroom-based portion of fabrication
- 5.7 – PDMS channel design fabricated using standard soft lithography
- 5.8 – Final process steps
- 5.9 – Isotropic wet etching of glass
- 5.10 – SEM of overetching
- 5.11 – Comparison of diameters of masks and final holes
- 5.12 – Characterization of lateral etch rates of 1:1 HF:DI Water on glass
- 5.13 – Radius of anchor as a function of etch time
- 5.14 – Etching of hard mask
- 5.15 – Overetching of chromium
- 5.16 – Improved etch isotropy
- 5.17 – SEM of one anchor after removal of a rectangular portion of the chrome-gold layer
- 5.18 – HP TIPS controller
- 5.19 – HP POEM thermal ink-jet printer setup
- 5.20 – Nonuniformity of SU-8
- 5.21 – Effects of prepolymer drying
- 5.22 – Desired profile of NIPAAm prepolymer after printing
- 5.23 – Printing process images
- 5.24 – Effect of exposure energy on swelling ratio
- 5.25 – Alignment device schematic
- 6.1 – Effects of continuous vs. interval expose
- 6.2 – Polymerization of poly(NIPAAm) in microwell
- 6.3 – Optical imaging of shrinkage
- 6.4 – Surface profile for three sample wells before and after heating
- 6.5 – Surface wetting of NIPAAm prepolymer solution
- 6.6 – Final fabricated prototype
- 6.7 – Optical images of radial shrinkage
- 7.1 – TEM image of Iron-Oxide nanoparticles in NIPAAm prepolymer solution
- 7.2 – Revised fabrication process flow

1. Introduction

Throughout the past two decades there has been a large rise in interest in microfluidic devices. The technology stemmed from the existing MEMS (Microelectromechanical Systems) technology, and has become attractive to scientists and researchers, particularly in the life sciences, due to the scaling benefits that occur with fluid flows at these size scales. Central to the design and utilization of microfluidic devices is valve structures used to control the flow. The main purpose of this thesis is to provide a new design for microfluidic valves that aims to resolve many of the issues with current valves that inhibit widespread use of these devices by many life science researchers and users. This chapter will briefly describe the importance of microfluidics and what technology currently exists for valves. It will establish motivation for this project and describe why the design presented in this thesis will be able to outperform current valves in many aspects.

1.1 Motivation and Device Design

A variety of microfluidic valves have been presented over the past few decades and are discussed in more detail in Section 1.2.3. The current state of the art, however, utilizes the deflection of flexible elastomeric materials to open and close channels. The simplest, and often most effective, method for creating microfluidic channels is to use a molding process whereby a silicone (PDMS) is cast from a silicon or SU-8 mold and then bonded to glass. Since PDMS is a flexible material, it can be used as a valve structure. By placing perpendicular channels adjacent to each other such that they are separated by only a small layer of PDMS one can create a valve. One channel contains the working fluid, while the other contains compressed air. When the pressure in the air channel is increased, the membrane deflects causing the channel with the working fluid to be pinched off thus preventing flow [1]. These structures, known as “Quake” valves are simple to make using multiple layers of PDMS, but have a series of drawbacks. Perhaps the most significant drawback is the reliance upon external equipment such as air compressors. While the devices themselves are small and inexpensive, their reliance upon bulky external

equipments limits their use in remote areas or doctors' offices. Additionally, the valves are often arrayed and controlled in a multiplexed fashion [2]. This limits the ability to individually actuate valves, as entire rows or columns of valves usually need to be actuated all at once.

The design presented in this thesis aims to achieve a variety of goals to improve upon current designs:

- Elimination of the dependence upon bulky external equipment
- Ease of fabrication for the end-user to allow for rapid prototyping by doctors and scientists without access to or training in micromachining facilities
- Individual actuation through electronic control
- Remote actuation for biomedical applications

The specific functional requirements and design parameters of the valves are discussed in more detail in Chapter 3.

In order to achieve these goals, a design is presented wherein poly(*N*-isopropylacrylamide), a thermosensitive hydrogel, is used as an actuation mechanism for the valves. This hydrogel shrinks when raised above a transition temperature. Using poly(NIPAAm) removes the dependence upon external equipment such as air compressors for the Quake valves or high voltage supplies for electroosmotic switching. Heating of the gel is all that is needed for actuation of the valve.

It is important that the valves be easy to use and fabricate by scientists and doctors who may not have access to cleanroom facilities. This allows for rapid prototyping and fabrication of a device. To achieve this goal, the design presented consists of valves that are arrayed on a separate substrate (Fig. 1.1). Users can use this template substrate to design their devices. They can use conventional soft lithography to create their channels. Wherever they want a valve, they just have to have their channel cross specific points on the template.

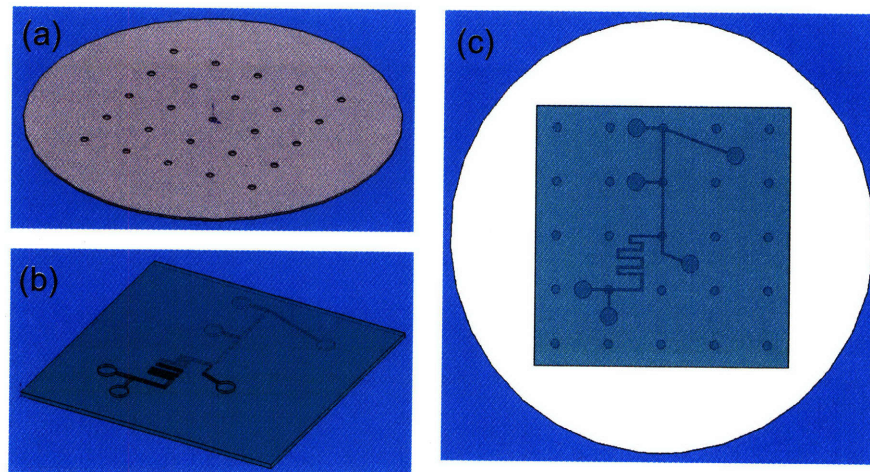


Fig. 1.1 – Template design allows for easy fabrication by the end-user: (a) template contains an array of possible valve locations; (b) user fabricates single-layer PDMS channels using soft lithography; (c) user bonds PDMS to template such that valves are aligned with channels in desired locations.

These valves can be actuated individually using controlled local heating. This heating can be provided using Joule heating or magnetic heating and controlled electronically. This is a great improvement over the Quake valves where entire rows or columns of valves have to be actuated at once.

Finally, these valves present the possibility of remote actuation using the magnetic heating. Perhaps, the most useful application of this is implantable microfluidic chips for drug delivery. Traditionally, these chips would require actuation using an electrical signal [3]. Using external magnetic fields, no interconnects would have to pass through the body, and no implanted batteries would be required.

There currently exists in the literature microfluidic poly(NIPAAm) valves [4-7]. While these valves achieve some of the aforementioned goals, their applications are limited both because of their means of fabrication and the channel materials that the valves are used in (they never use PDMS or soft lithography). Furthermore, there is no known poly(NIPAAm) valves in the literature that utilize magnetic nanoparticles as an actuation mechanism.

The design of the proposed valve consists of a microwell into which the prepolymer solution is filled. The gel is then polymerized by UV light rather than a RedOx reaction

in order to ensure that there are no remaining chemicals after the polymerization. PDMS channels are bonded on top of the template substrate that contains the microwell. The channels are designed such that there is a discontinuity at the location of the well. When the poly(NIPAAm) is in its swollen state, no fluid can pass through (Fig. 1.2(a)). When it shrinks, however, it creates a gap between the bottom of the PDMS and the top of the hydrogel. This allows fluid to flow into the well and into the other part of the channel (Fig. 1.2(b)).

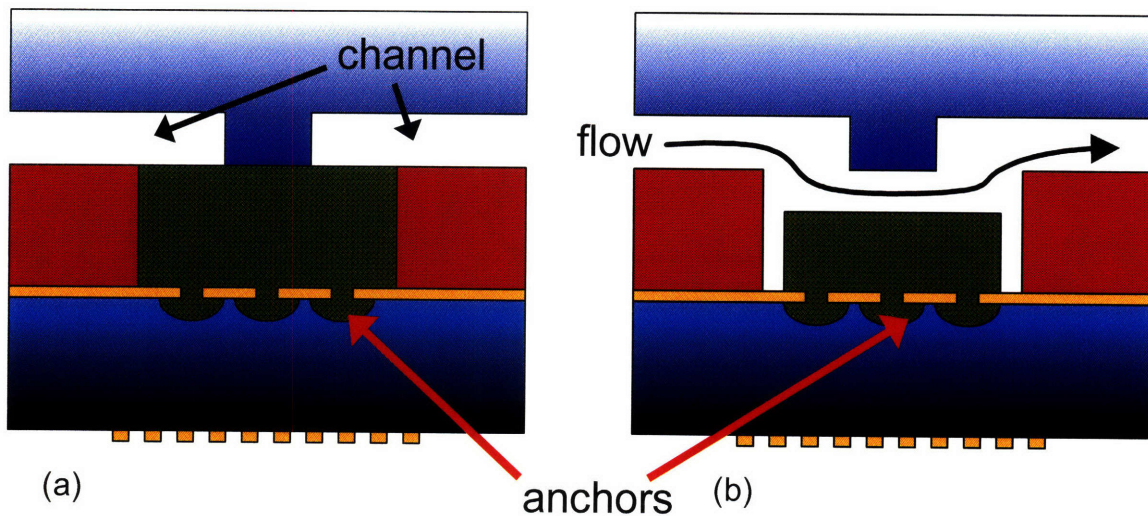


Fig. 1.2 – Valve design: (a) swollen poly(NIPAAm) prevents fluid from flowing from the left side of the channel to the right; (b) shrinking of the gel allows fluid to flow past the discontinuity.

One of the key elements of this design are the anchor structures at the bottom of the well. These anchor structures are necessary for ensuring that the shrinkage is predictable. In their absence, the gel would be allowed to move freely with the flow and would likely be pushed up into the channel causing it to be blocked. By using anchors at the bottom center of the well, it ensures that the shrinkage is always downward and towards the center. This controlled shrinkage also helps to minimize the pressure drop and reduce the information content of the design (these aspects are discussed in more detail later in this thesis). The details of the modeling of these anchors are discussed further in Section 4.2.3.

Using this valve design, the aforementioned goals can be achieved. The remainder of this thesis will discuss the various aspects considered in designing the valve. Background modeling is presented to justify design decisions and to generate the important equations used in deciding the design parameters. Axiomatic Design is employed to generate the principles of how the valve operates and to decouple the design components. Additional modeling that utilizes the equations generated in the background modeling chapter is performed to analyze the specific design choices made using the Axiomatic Design approach. Finally, fabrication and testing of the device is presented along with a discussion of future work that needs to be performed.

1.2 Microfluidics

1.2.1 History

While microfluidic systems have been around for a long time, they really began to accrue attention in the early 1990's. While devices such as inkjet printers that use microfluidics have had commercial success, the majority of the advances in the field have yet to see commercialization. A variety of domains are included under the umbrella of microfluidics including explosive thermofluidic flows (e.g. inkjet printers), gas flows (e.g. microturbine engine), and slow liquid flows.

One of the biggest advancements in the field of microfluidics was the introduction of their use to the life sciences. In 1990 Figeys *et al.* introduced the concept of "lab on a chip" [8], and in 1992, Manz *et al.* introduced on-chip capillary electrophoresis [9]. The scaling benefits of controlling fluids at such size scales became immediately apparent, and a variety of researchers began pursuing their uses in the life sciences.

Whitesides describes the field of microfluidics as the product of molecular analysis, biodefence, molecular biology, and microelectronics [10]. Interest in chromatography and capillary electrophoresis drove the use of microfluidics for analysis. With the rise of

biological weapons and defense threats, microfluidics was a natural approach to tackling these issues. Furthermore, sequencing and genomics was achieving great strides at the same time. The advancements in microfluidics, such as PCR-on-chip, allowed for advantages and new discoveries in the fields of molecular biology. Finally, what made all of this possible were the advancements in technology for micromachining. Initiated by the integrated circuit (IC) industry and advanced by the microelectromechanical systems (MEMS) community, a variety of fabrication tools were available that allowed researchers to take advantage of microfluidics.

In addition to the technologies provided by the MEMS and IC industries, one of the most important contributions was the introduction of poly(dimethylsiloxane) (PDMS) as a material for microfluidics by the Whitesides group [11, 12]. PDMS is an inexpensive optically clear inexpensive flexible elastomer that can be molded on silicon or other micromachining materials. It can then be covalently bonded to glass using oxygen plasma. This process has been dubbed “soft lithography” [13, 14] and is depicted in Fig. 1.3.

PDMS revolutionized the field of microfluidics for many reasons. Perhaps most important are the cost benefits. PDMS is inexpensive and extremely easy to fabricate. It has the ability to mold almost any contour even in extremely high aspect ratio features. Its ability to be bonded to glass was another huge benefit. Also, because it is a soft elastomer, it can deform easily. This is often desired for the applications of pumps and valves.

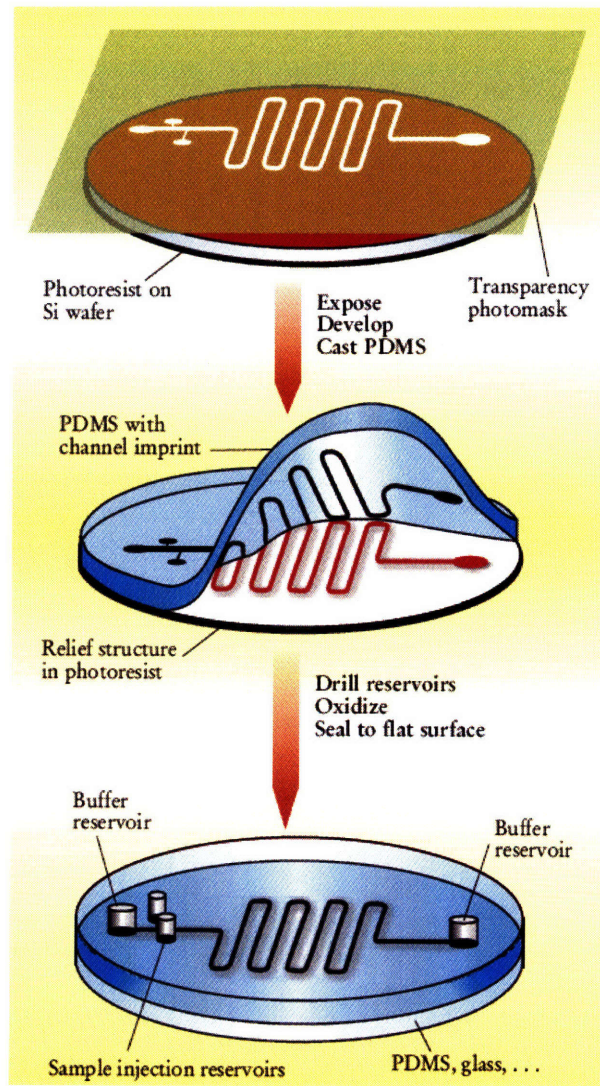


Fig. 1.3 – Fabrication of channels using soft lithography: photoresist is patterned on silicon wafer; PDMS is poured onto wafer and cured; cured PDMS is peeled off and exposed to oxygen plasma; PDMS is bonded to glass or other PDMS [12].

1.2.2 Scaling Benefits

Perhaps the most important quantity to consider when discussing microfluidics is the Reynolds Number. The Reynolds number is defined as

$$\text{Re} \equiv \frac{\rho UL}{\mu} \quad (1.1)$$

where ρ is the density, μ is the dynamic viscosity, U is a characteristic velocity, and L is a characteristic length. It represents the a comparison of the importance of the inertial terms to the viscous terms and is the result of scaling the Navier-Stokes equation (this is done in Section 2.1.1). Due to the small length scales and relatively small velocities in microfluidic devices, the Reynolds Number is usually very low. From a mathematical perspective, this means that the inertial terms (the left side of the Navier-Stokes equation) can be ignored. In physical terms it means that flows are laminar and that no mixing occurs outside of diffusion.

In addition to laminar flow, the small size scales present a regime where diffusion is much more important. Diffusive time constants usually scale as the length squared (see Sec. 2.1.2). Since length scales in microfluidic channels are so small, diffusion plays a much larger role and can be utilized for techniques such as mixing and separation where they would not be practical at the macroscale.

Finally, the high surface area to volume ratios result in the fact that surface forces tend to dominate over body forces. Additionally, heat transfer occurs over much shorter timescales since the thermal capacitance is so low. This is one of the main reasons why PCR can be performed more efficiently at the microscale [15]. Since surface forces are dominant at small size scales the effects of surface tension become much more important. These effects can be good and bad. On the one hand, capillary forces can be used to drive flow or move fluids. On the other hand, bubble formation can be become a huge problem. It is often very difficult to get rid of these bubbles since surface tension causes them to stick to channel walls.

Some of the most important benefits of these scaling effects are the utilizations of various microfluidic interfaces. The importance of these interfaces has been discussed extensively in the literature [16]. Perhaps the most famous device is a t-junction wherein two miscible fluids meet and flow parallel to each other (Fig. 1.4(a)). As they pass down the length of the channel the only mixing that occurs is due to diffusion. This is because turbulent mixing is not possible at these Reynolds Numbers. Thus, one can measure the

diffusivity of a solute since the velocity and diffusion length is known from the device. Expanding upon this device, researchers designed the H-filter. This device allows one to separate solutes based upon their diffusivities. Since smaller solutes diffuse faster than larger ones, they will diffuse into the parallel buffer stream faster and can be separated from the original solution (Fig. 1.4(b)).

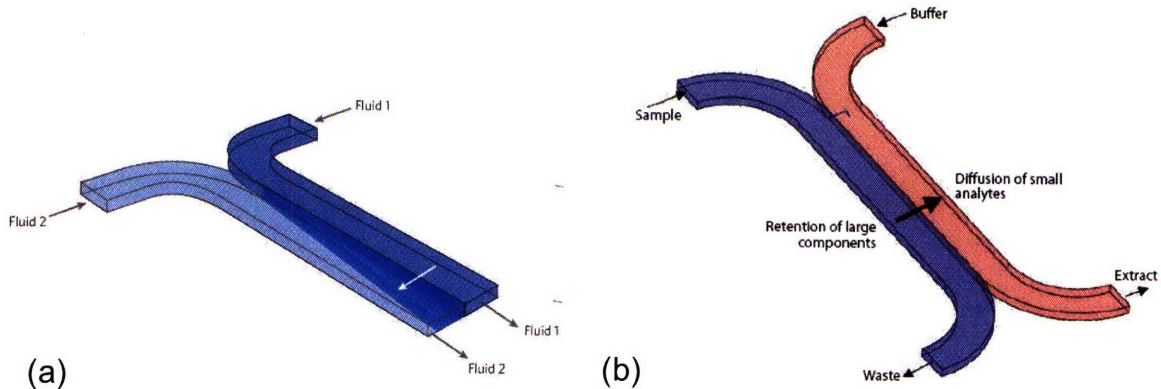


Fig. 1.4 – Interfaces between miscible fluids: (a) diffusivity measurements can be made using t-junctions by effectively visualizing time as space [16]; (b) H-filters allow one to separate two different solutes in a solution based upon their diffusivities [17].

Other phenomena such as the creation of droplets at t-junctions or using flow focusing of two immiscible fluids have been well characterized [18-20]. These droplets can be used for cell encapsulation or transport of molecules. Additionally, interfaces of concentration gradients can be created [21] as well as zero-flow interfaces for studying cell signaling [16].

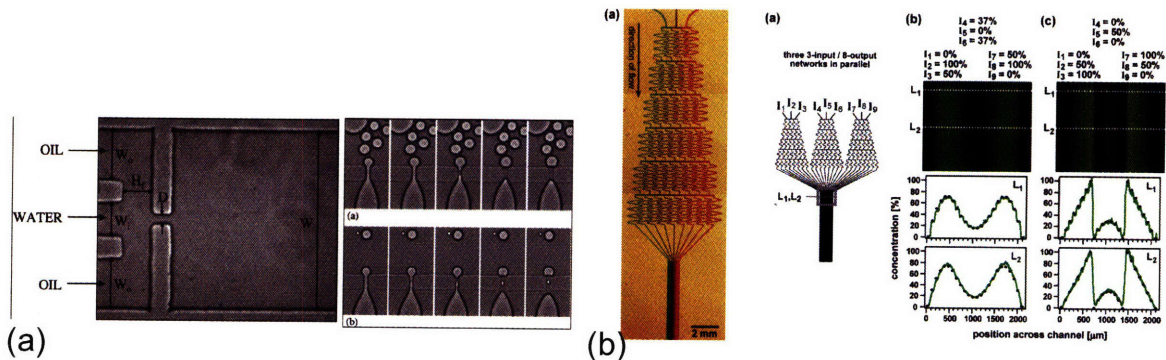


Fig. 1.5 – Control over microfluidic interfaces can result in many different phenomena: (a) creation of microdroplets using two immiscible fluids [19]; (b) establishment of complex concentration gradients to study transport and mimic real biological systems [21].

1.2.3 Valves in Microfluidics

The ultimate goal of many researchers in the field of microfluidics is the advent of the “micro-total analysis system” (μ TAS). Such systems would be able to achieve a full analysis of a solution from start to finish. This might include separating DNA from whole blood, amplifying the DNA, performing electrophoresis and separation, etc. In order for these systems and many other microfluidic systems to operate, they need valves. Since almost all microfluidic systems contain valves, it is no surprise that they have been the focus of much of the literature over the lifetime of microfluidics.

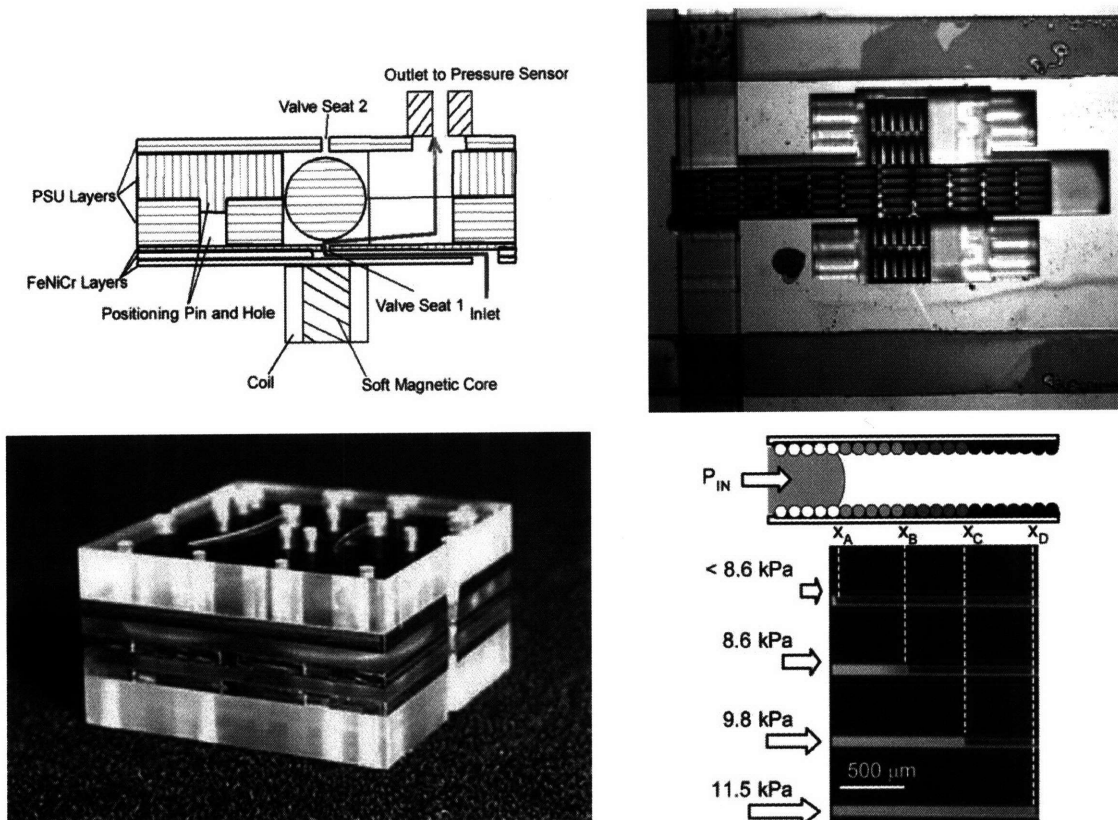


Fig. 1.6 – Various early microfluidic valves: (a) magnetic [23]; (b) electrolytic bubble formation [24]; (c) piezoelectric valve composed of nine layers[25]; (d) fluid flow controlled by surface wettability [26].

Following the traditional actuation mechanisms of the MEMS industry, the first valves were primarily driven by electrostatic [22] and magnetostatic [23] mechanisms. These valves tended to be bulky and require extensive amounts of micromachining. Thermal and electrochemical valves were also fabricated that used bubble formation to their

advantage to actuate valves using a concept similar to that of the thermal inkjet printers [24]. Piezoelectric valves were designed [25] that used stack piezos and provided faster response times and could withstand higher pressures. Unfortunately, fabrication complexities and size made them impractical for use in inexpensive microfluidic devices. Other valves have been designed that take advantage of surface interactions and wettability to create valves with not moving parts [26]. These valves, however, require careful tailoring for each fluid used and have significant pressure limitations.

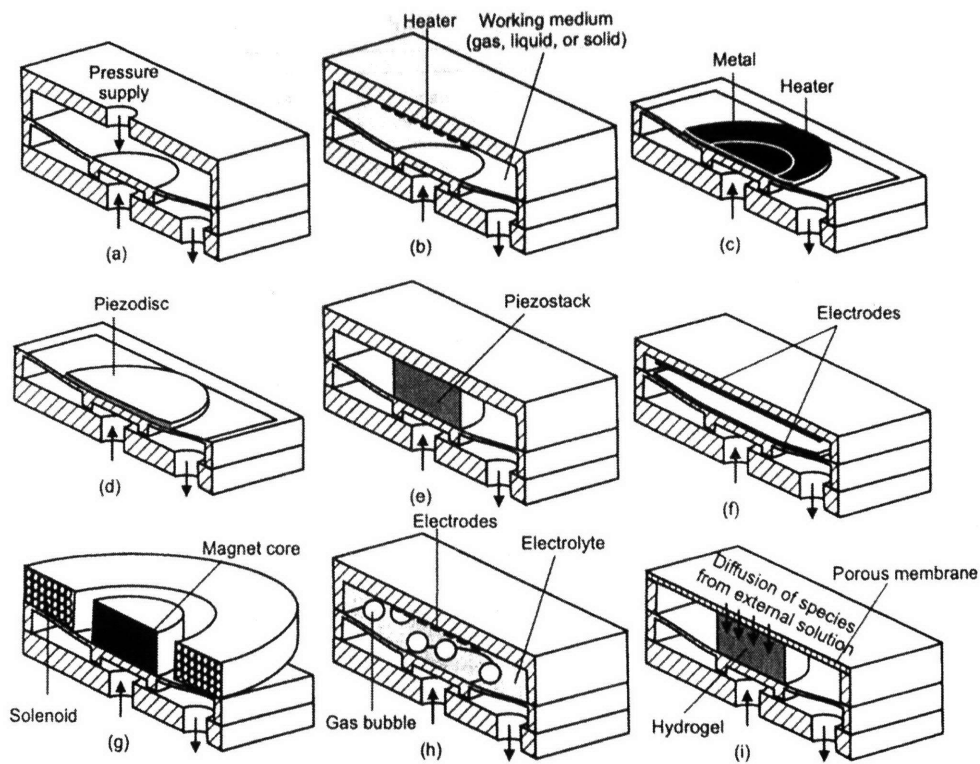


Fig. 1.7 – Different types of common microfluidic valves: (a) pneumatic; (b) thermopneumatic; (c) thermomechanical; (d) piezoelectric; (e) piezoelectric; (f) electrostatic; (g) electromagnetic; (h) electrochemical; (i) chemical [27].

Nguyen discusses many of the conventional valves used in microfluidics [27]. These valves are shown in Fig. 1.7. In addition to these valves, a variety of more unconventional valves have been presented in the literature including paraffin [28] and ice [29] phase-change valves which allow for simple heating of a material above its phase transition temperature to cause actuation. While these valves are easily actuated, they can obviously only be used once.

The most significant valves used in microfluidics today take advantage of the flexible nature of PDMS. These valves were designed by the Quake group while he was a professor at California Institute of Technology and are known throughout the industry as “Quake Valves” [1, 2]. The general principle behind the valves is similar to that of stepping on a garden hose. Two non-intersecting channels lie orthogonal to each other with one above the other and a thin layer of PDMS between them (Fig. 1.8). The bottom channel contains the working fluid while the top channel contains compressed air. By increasing the pressure in the top channel, the bottom of the channel will deflect causing the adjacent channel to be pinched closed.

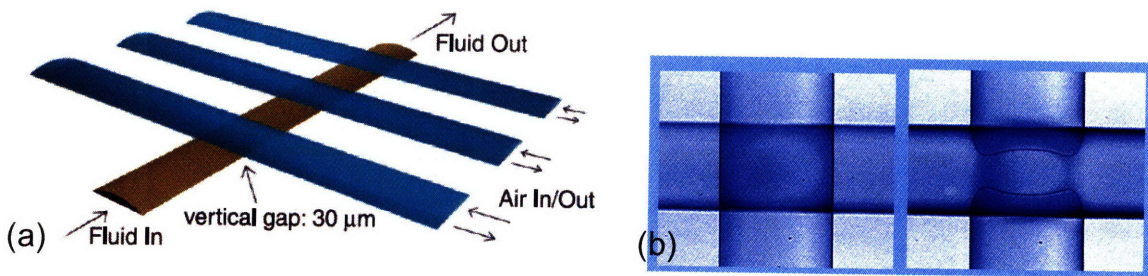


Fig. 1.8 – Quake valves: compressed air in the top channel causes deflection of the membrane between the channels and closing of the channel with the working fluid. [1, 30]

These valves are extremely easy to fabricate since they are based upon soft lithography. Furthermore, they can be scaled up for large microfluidic devices [2]. This is shown in Fig. 1.9 where a large multiplexed device is designed for analysis. Because one cannot add additional layers for each valve, however, this valve design is usually limited to actuating whole columns or rows. Additionally, the use of air compressors or other air pressure sources is largely undesirable for use in commercial devices. Some of the biggest advantages of microfluidic devices are their disposability and the opportunity to use them in places like doctors’ offices, the battlefield, and third world countries where access to sophisticated labs is not available. Reliance upon extensive external equipment such as air compressors severely limits the commercial application of these valves.

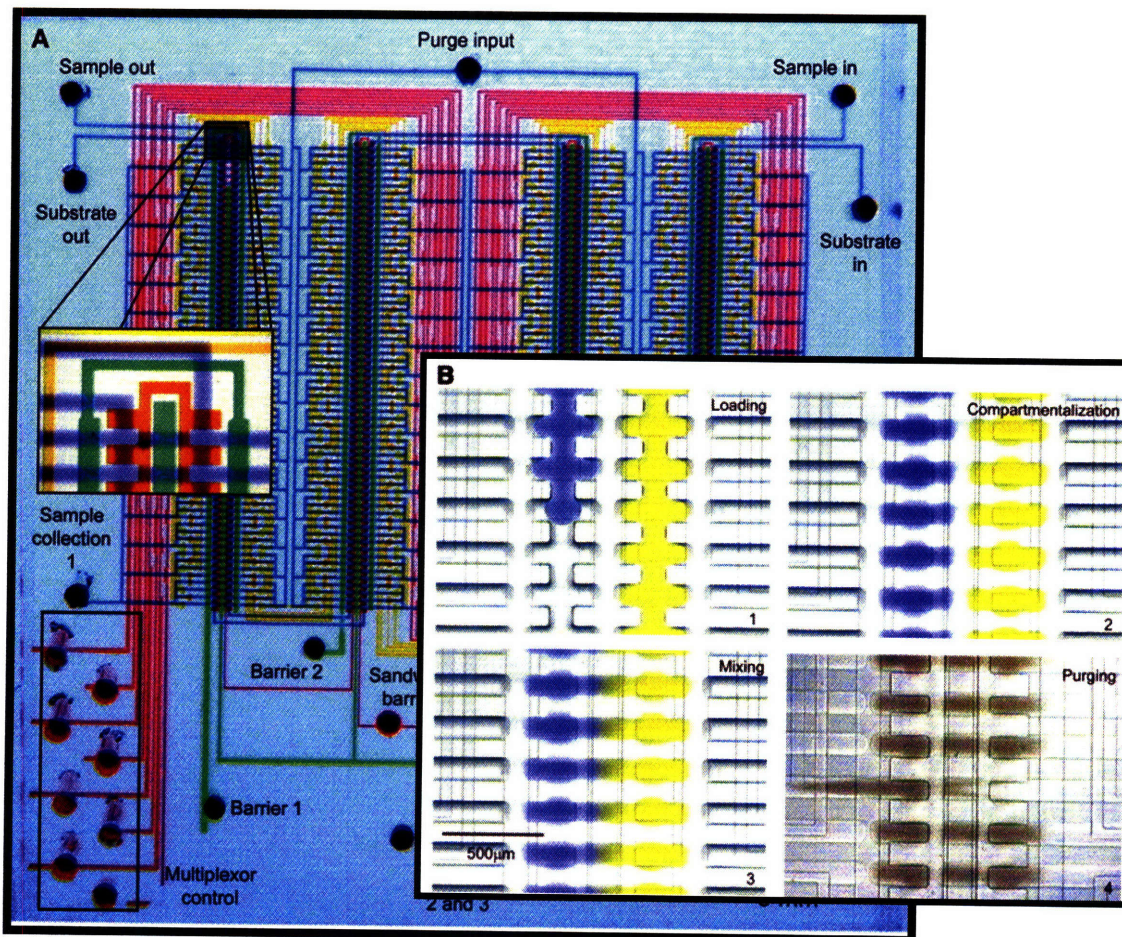


Fig. 1.9 – Quake valves can be scaled up for use in large-scale multiplexed analysis systems [2].

This dilemma is part of what is often referred to as “chip-to-lab interfacing.” While the benefits of microfluidic chips have been largely established and the techniques for fabricating them have been well developed, they have yet to see any real commercial success [10]. This is most likely due to the limitations that come from interfacing with them in a practical manner. Control of the valves can be the most limiting factor. Addressing this pressing concern will likely result in products that can be commercialized much more readily.

1.3 Hydrogels and poly(NIPAAm)

1.3.1 Background of Hydrogels

Hydrogels are polymer networks composed of crosslinked chains that are capable of large degrees of swelling due to the filling of their interstitial spaces with water. They can be both natural and synthetic and are used widely throughout the field of tissue engineering primarily in the form of scaffolds. This is due to the fact that their geometry and general chemistry is very similar to that of tissue. Their biocompatibility makes them very attractive not only as scaffolds, but also for drug delivery. Over the past few decades there has been much discussion and advancement in this application [31-40].

Hydrogels swell in water because the polymer chains are hydrophilic. The water molecules are attracted to the chains. The crosslinks keep the gels together, and prevent the chains from dispersing. Instead the gels swell as the water molecules fill up the spaces between the chains. In general, the swelling can be described as a diffusive process [41]. In addition to their swelling behavior, they can be combined with other structures to form unique copolymers (Fig. 1.10) [42].

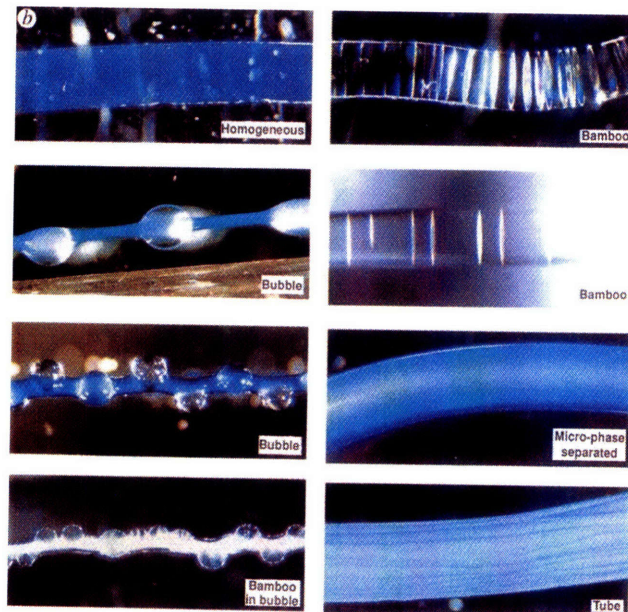


Fig. 1.10 – Unique patterns exhibited by gels undergoing changes in phase [42].

One subset of hydrogels that is particularly interesting is stimuli-responsive hydrogels. These are hydrogels that exhibit changes in their swelling behavior in response to changes in their environment. These can be changes in things such as pH, pI, or

temperature. This thesis will focus on the last of these and their application to valve structures in microfluidics.

1.3.2 Theory of Swelling

N-isopropylacrylamide (NIPAAm) is a hydrogel that exhibits an inverse temperature-volume relationship. This thermosensitive hydrogel has a lower critical solution temperature (LCST) above which the gel becomes hydrophobic (~32°C). When this occurs, the water molecules are expelled from within the network. Because the gel is crosslinked, rather than precipitating out the NIPAAm, the poly(NIPAAm) gel shrinks. This behavior was first recorded by Hirokawa and Tanaka [43], although similar behavior had been seen in other types of gels before.

A variety of theories have been proposed that are both qualitative and quantitative to describe the mechanisms behind this behavior [43-60]. Varying degrees of complexity can be added to the models; however, they are all generally based upon thermodynamic principles. The NIPAAm monomer is composed of both hydrophilic and hydrophobic groups (Fig. 1.11). When immersed in an aqueous solvent, the hydrophilic groups form hydrogen bonds with the water since this interaction lowers the free energy, where the Gibbs free energy is defined as:

$$G = H - TS \quad (1.2)$$

Here, G is the Gibbs free energy, H is the enthalpy, S is the entropy, and T is the absolute temperature. The hydrogen bonds contribute to the decrease in enthalpy of mixing. Alternatively, the hydrophobic groups require ordering of the water molecules around them and thus the interaction results in negative entropy. This, in turn, results in an increase in free energy. Furthermore, the resultant bond orientations also increase the entropy. As temperature increases, the entropic term becomes more dominant to a point (the LCST) where it is larger than the enthalpic term. This results in a weakening and eventual destruction of the hydrogen bonds. At the same time, the hydrophobic

interactions increase resulting in folding of the gel and subsequent shrinking [56],[53],[44, 52, 60].

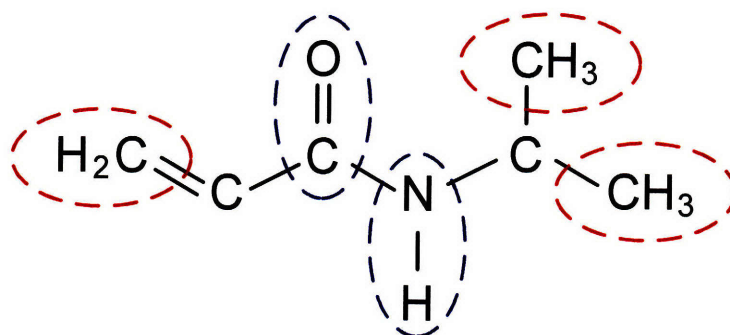


Fig. 1.11 – Chemical structure of NIPAAm monomer. Red ovals denote hydrophobic groups, and blue ovals denote hydrophilic groups.

1.4 Magnetic Nanoparticles

There are a variety of ways to generate heat and cause shrinking of poly(NIPAAm) gels. One can raise the temperature of the gel by raising the temperature of the fluid that it is in, by resistive (Joule) heating, or even through the use of magnetic nanoparticles. One can generate heat from magnetic nanoparticles by subjecting them to oscillating magnetic fields. The use of this heating with nanoparticles has been of great interest to researchers for use in hyperthermia applications and with thermosensitive hydrogels along with other biomedical applications [61-66]. The designs fabricated in thesis do not include magnetic nanoparticles as the heating mechanisms. However, it is important to discuss them since they will undoubtedly be included in future iterations of the device.

Iron-oxide nanoparticles are superparamagnetic nanoparticles that have been widely used due to their biocompatibility. Lao and Ramanujan used Fe_3O_4 nanoparticles to generate heat inside polyvinyl alcohol (PVA) hydrogel [64]. They demonstrated the time response of the heating of the gel due to various field strengths at 375kHz (Fig. 1.12). In general, higher field strengths resulted in faster heating. The gels used in this study were approximately 7-8cm in diameter. By shrinking the gels to the microscale, one would

expect much shorter timescales since the heat conduction scales as the length squared (Section 2.3.2).

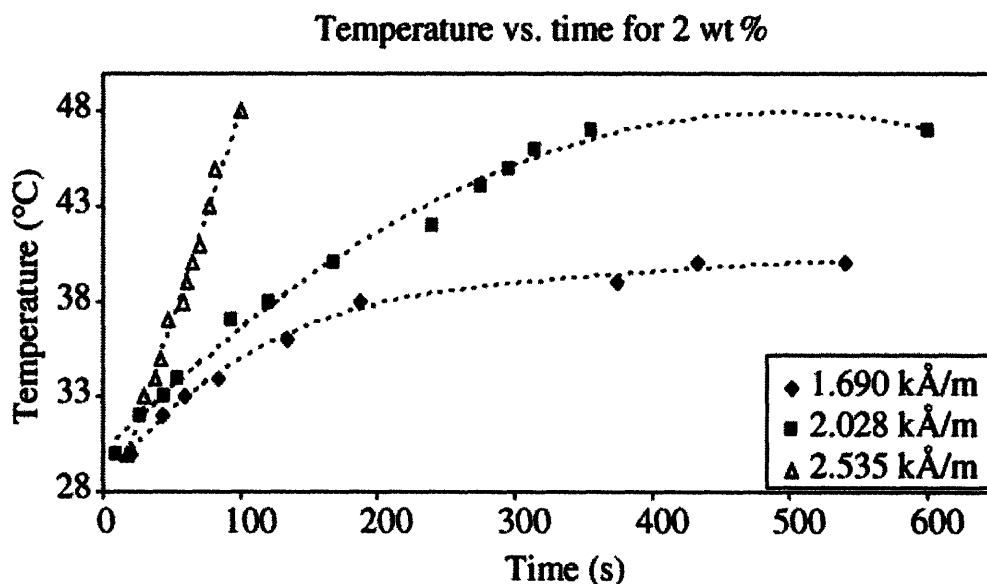


Fig. 1.12 – Heating of PVA gels as a function of time for various field strengths with 2wt% nanoparticles [64]. Increasing the wt% of nanoparticles also increases the response time (not shown).

Kato *et al.* used magnetic nanoparticles in poly(NIPAAm) gels to make chemomechanical actuators [63]. By subjecting cylindrical gel rods containing $\gamma\text{-Fe}_2\text{O}_3$ nanoparticles to oscillating magnetic fields, he measured length changes as a function of temperature (Fig. 1.13) as well stress-strain curves below and above the LCST.

Thus, heating and actuation of hydrogels and poly(NIPAAm) using magnetic nanoparticles has been demonstrated throughout the literature. As was discussed at the beginning of this chapter, the application of this actuation mechanism to poly(NIPAAm) valves presents a wide range of advantages over conventional microfluidic valves.

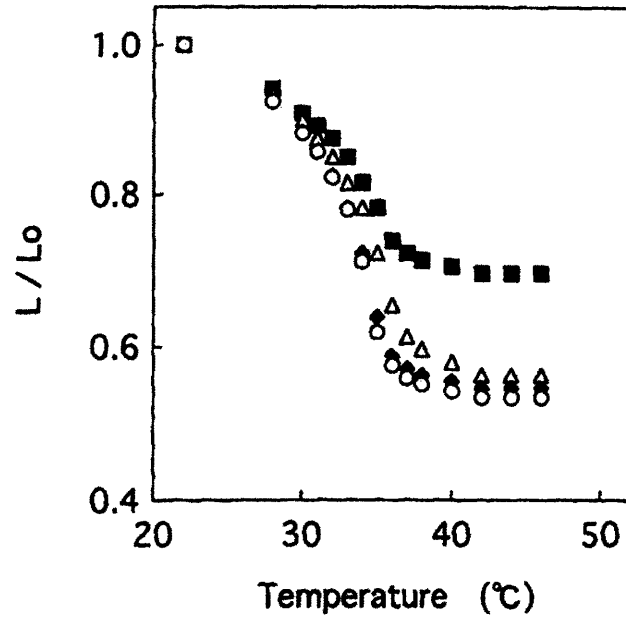


Fig. 1.13 – Length changes in cylindrical poly(NIPAAm) rods due to heating from nanoparticles [63]. The amount of $\gamma\text{-Fe}_2\text{O}_3$ is circles: 0%; diamonds: 8%; triangles: 16%; and squares: 24%.

2. Background Modeling

The purpose of this chapter is to provide the reader with the necessary modeling that used throughout the remainder of the thesis. Many of the design decisions made are based upon scaling arguments and more developed models discussed throughout this chapter. The design of these valves spans across many physical domains including fluid mechanics, solid mechanics, polymer mechanics, chemistry, electromagnetism, heat transfer, and mass transport. While many of the governing equations of the system are derived, the focus of this chapter is on the modeling techniques used to determine the design parameters along with models that demonstrate which parameters can be neglected. In a system whose domains are so highly coupled, it is important to develop these models in order to fully decouple the system and allow the designer to have some way of determining an effective design prior to its fabrication.

2.1 Solid and Fluid Mechanics

2.1.1 Fluid Dynamics: Navier-Stokes and Low Reynolds Number Flows

2.1.1.1 Navier-Stokes

The governing equation related to the motion of Newtonian fluids is the well known Navier-Stokes equation:

$$\rho \frac{D\mathbf{v}}{Dt} = -\nabla p + \mu \nabla^2 \mathbf{v} + \frac{\mu}{3} \nabla(\nabla \cdot \mathbf{v}) + \rho \mathbf{G} \quad (2.1)$$

where $D\mathbf{v}/Dt$ is the material derivative, and is defined as

$$\frac{D\underline{v}}{Dt} = \frac{\partial \underline{v}}{\partial t} + (\underline{v} \cdot \nabla) \underline{v} \quad (2.2)$$

For incompressible fluids, the Navier-Stokes equation is reduced to the following by applying continuity ($\nabla \cdot \underline{v} = 0$):

$$\rho \frac{D\underline{v}}{Dt} = -\nabla p + \mu \nabla^2 \underline{v} + \rho \underline{G} \quad (2.3)$$

Scaling arguments can be made to determine the relevant importance of the various terms of the equation. This is essential as the Navier-Stokes equation has no analytical solution in its complete form. First, one can define the following nondimensional terms:

$$\tilde{\underline{v}} = \frac{\underline{v}}{U} \quad (2.4)$$

$$\tilde{\nabla} = \nabla L \quad (2.5)$$

$$\tilde{t} = \frac{tU}{L} \quad (2.6)$$

Here, U represents some characteristic velocity such as the maximum velocity or the mean velocity. L is a characteristic length. In the application of pipe flow, it is usually beneficial to compare the inertial terms to the viscous terms. By examining Eq. 2.3, one can note that the equation closely resembles Fick's diffusion equation:

$$\frac{DC}{Dt} = D \nabla^2 C + R \quad (2.7)$$

D is the diffusion coefficient. Thus, the Navier-Stokes equation can be thought of as a form of the diffusion equation where it is momentum that is diffusing. Since momentum diffuses across the diameter of the channel in pipe flow, one should use the diameter as the characteristic length when scaling the Navier-Stokes equation. Finally, there is no obvious time constant with which to use to nondimensionalize t , so instead, one can

create a time constant from the other characteristic constants. Inserting equations 2.4, 2.5, and 2.6 into Eq. 2.3 results in:

$$\rho \left[\frac{\partial(U\tilde{v})}{\partial(\tilde{t}L/U)} + \left(U\tilde{v} \cdot \frac{\tilde{\nabla}}{L} \right) U\tilde{v} \right] = -\frac{\tilde{\nabla}}{L} p + \mu \frac{\tilde{\nabla}^2}{L^2} (U\tilde{v}) + \rho \underline{G} \quad (2.8)$$

which reduces to:

$$\frac{\rho U^2}{L} \frac{D\tilde{v}}{D\tilde{t}} = -\frac{\tilde{\nabla}}{L} p + \frac{\mu U}{L^2} \tilde{\nabla}^2 \tilde{v} + \rho \underline{G} \quad (2.9)$$

$$\frac{D\tilde{v}}{D\tilde{t}} = -\frac{1}{\rho U^2} \tilde{\nabla} p + \frac{\mu}{\rho UL} \tilde{\nabla}^2 \tilde{v} + \rho \underline{G} \quad (2.10)$$

The important nondimensional term that arises is known as the Reynolds number:

$$\text{Re} = \frac{\rho UL}{\mu} \quad (2.11)$$

This number can be used to compare the relative importance of the inertial terms to the viscous terms. For high Reynolds number flows, the viscous terms are negligible and the Navier-Stokes equation can be simplified to Bernoulli's Equation along a streamline:

$$\frac{1}{2} \rho v^2 + \rho gh + p = \text{const.} \quad (2.12)$$

For flows with Reynolds numbers much less than one, the Navier-Stokes equation simplifies to Stokes's Equation:

$$0 = -\nabla p + \mu \nabla^2 \underline{v} + \rho \underline{G} \quad (2.13)$$

When other external forces (e.g. electromagnetic, gravitational, centrifugal, etc.) are negligible, this simplifies to:

$$\nabla p = \mu \nabla^2 \underline{v} \quad (2.14)$$

By using this form of the governing equation in conjunction with continuity, one can find many analytical solutions to viscous dominated fluid flow problems.

2.1.1.2 Viscous Flow in Microfluidics

For meso- and macro-scale fluid flow, Bernoulli's equation is usually used for liquids generally assumed to be inviscid (e.g. water). At the micro- and nano-scale, however, Bernoulli's equation does not apply. Despite using fluids like water, the Reynolds number is usually still much less than one since the dimensions and velocities are so small. This mandates the use of Stokes's equation, and has many interesting implications for the fluid behavior.

Turbulent flow is characterized as flow having Reynolds numbers above 4000. In this flow regime eddies, vortices, and recirculating flows are common. This form of chaotic fluid flow is often the most effective way to generate mixing between two fluids. Because flows in microfluidic channels are inherently low Reynolds number, these forms of turbulent mixing do not occur.

Microfluidic flows are characterized by internal flows in channels. It is often essential to know the velocity profiles and pressure drops across a given length of straight channel. To find this profile, one can solve Stokes's Equation (Eq. 2.14) using the no-slip boundary condition. The no-slip boundary condition simply states that the fluid velocity at the interface of the fluid and a non-moving body must be zero. There is some question as to the validity of this condition at extremely small length scales and at the interfaces between fluids and polymers, but for the majority of situations it is valid.

First, one can rewrite Stokes's Equation in the two-dimensional Cartesian form:

$$\frac{\partial p}{\partial x_1} = \mu \left(\frac{\partial^2 v_1}{\partial x_1^2} + \frac{\partial^2 v_1}{\partial x_2^2} \right) \quad (2.15)$$

$$\frac{\partial p}{\partial x_2} = \mu \left(\frac{\partial^2 v_2}{\partial x_1^2} + \frac{\partial^2 v_2}{\partial x_2^2} \right) \quad (2.16)$$

A variety of other assumptions need to be made. The first is that the fluid is Newtonian, and is already implicit in Stokes's Equation. Next, one should assume that the flow is fully-developed. This ensures that the velocity profile is constant along the pipe and thus $\partial v / \partial x_1 = 0$. This assumption simplifies the equations to:

$$\frac{\partial p}{\partial x_1} = \mu \frac{\partial^2 v_1}{\partial x_2^2} \quad (2.17)$$

$$\frac{\partial p}{\partial x_2} = \mu \frac{\partial^2 v_2}{\partial x_2^2} \quad (2.18)$$

It is also important to assume that the fluid is incompressible. One can then apply the incompressible form of the continuity equation:

$$\frac{\partial v_2}{\partial x_2} = 0 \quad (2.19)$$

This results in:

$$\frac{\partial p}{\partial x_2} = 0 \quad (2.20)$$

Thus, the pressure does not vary in the x_2 direction, allowing Equation 2.17 to be rewritten as:

$$\frac{dp}{dx_1} = \mu \frac{d^2 v_1}{dx_2^2} \quad (2.21)$$

Since the velocity has no dependence on the x_1 direction and the pressure has no dependence on the x_2 direction, one can integrate twice to determine the velocity profile:

$$v_1(x_2) = \frac{1}{2\mu} \frac{dp}{dx_1} x_2^2 + C_1 x_2 + C_2 \quad (2.22)$$

Recognizing that the velocity profile should be symmetric about the central axis, one can apply a symmetry boundary condition on the derivative of the velocity:

$$\left. \frac{dv_1}{dx_2} \right|_{x_2=0} = 0 = \frac{1}{\mu} \frac{dp}{dx_1} (0) + C_1 \Rightarrow C_1 = 0 \quad (2.23)$$

Applying the aforementioned no-slip boundary condition results in:

$$v_1 \Big|_{x_2=\frac{h}{2}} = 0 = \frac{1}{2\mu} \frac{dp}{dx_1} \left(\frac{h}{2}\right)^2 + C_2 \Rightarrow C_2 = -\frac{h^2}{8\mu} \frac{dp}{dx_1} \quad (2.24)$$

Thus, the velocity profile can be expressed as:

$$v_1(x_2) = \frac{h^2}{8\mu} \frac{dp}{dx_1} \left[4 \left(\frac{x_2}{h} \right)^2 - 1 \right] \quad (2.25)$$

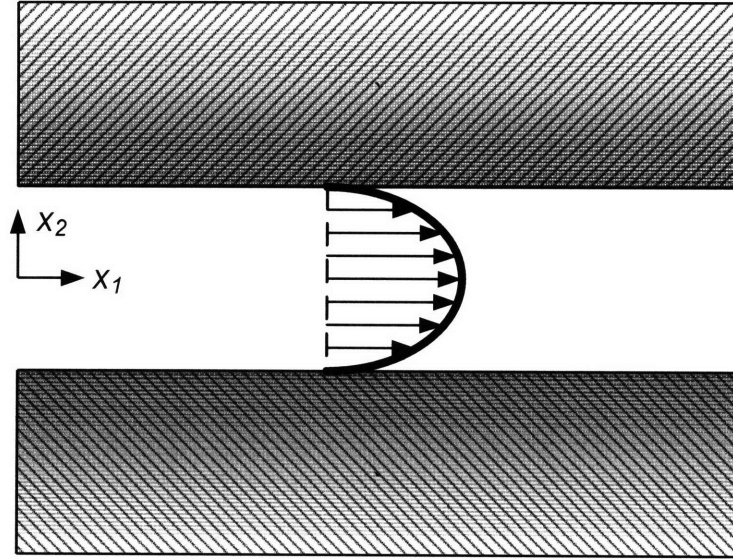


Fig. 2.1 – Velocity profile. Internal flows of this profile are known as Poiseuille flow.

The velocity profile is parabolic (Fig. 2.1). This type of flow is known as Poiseuille flow, and is characteristic of most flows in microfluidic devices. One can determine the average velocity, U , by integrating over the height of the channel:

$$U = \frac{1}{h} \int_{-\frac{h}{2}}^{\frac{h}{2}} v_1(x_2) dx_2 = \frac{h}{8\mu} \frac{dp}{dx_1} \int_{-\frac{h}{2}}^{\frac{h}{2}} \left[4 \left(\frac{x_2}{h} \right)^2 - 1 \right] dx_2 \quad (2.26)$$

$$U = -\frac{h^2}{12\mu} \frac{dp}{dx_1} \quad (2.27)$$

The pressure dependence upon the distance down the channel can be found in terms of the average velocity by integration:

$$\frac{dp}{dx_1} = -\frac{12\mu U}{h^2} \Rightarrow p(x_1) = -\int \frac{12\mu U}{h^2} dx_1 \quad (2.28)$$

$$p(x_1) = -\frac{12\mu U}{h^2} x_1 + C \quad (2.29)$$

Since pressure is a relative quantity, one can define inlet pressure ($x_1 = 0$) to be P_1 . This results in the following expression for the pressure:

$$p|_{x_1=0} = P_1 = -\frac{12\mu U}{h^2}(0) + C \Rightarrow C = P_1 \quad (2.30)$$

$$p(x_1) = P_1 - \frac{12\mu U}{h^2} x_1 \quad (2.31)$$

Often times, the volume flow rate is known rather than the velocity in the channel. This is the case for microfluidic flows driven by automated syringe pumps. The volume flow rate, Q , is simply the velocity integrated over the cross sectional area of the channel:

$$Q = \iint_A v_1(x_2) dA = Uhw \Rightarrow Q = -\frac{h^3 w}{12\mu} \frac{dp}{dx_1} \quad (2.32)$$

where w is the width of the channel. The pressure drop can be rewritten in terms of the volume flow rate as:

$$p(x_1) = P_1 - \frac{12\mu Q}{h^3 w} x_1 \quad (2.33)$$

This expression for the pressure drop will prove useful when developing a lumped element model for the system in Section 2.5.2. It is interesting to note the strong dependence upon channel height when determining the pressure drop across a length of channel. It can be shown (although it is not done so here) that the parabolic profile develops across the smallest channel dimension. Across the larger dimension (here taken to be the width), momentum diffuses over the same length, and thus the center of the profile is flat. Because of this geometry, it is essential that the height, h , of Eq. 2.33 be taken to be the smaller of the two cross-sectional channel dimensions.

2.1.2 Mechanics and Kinetics of Gels

Modeling of the kinetics of gels is an important topic for any systems that use hydrogels and has been pursued since the 1960s [67]. Most of these models are based upon diffusion. The original one presented by Buckley[67] was incorrect due to the fact that it treated the swelling kinetics as diffusion of the solvent molecules rather than the network. The most common description was formulated by Tanaka in 1978 [41].

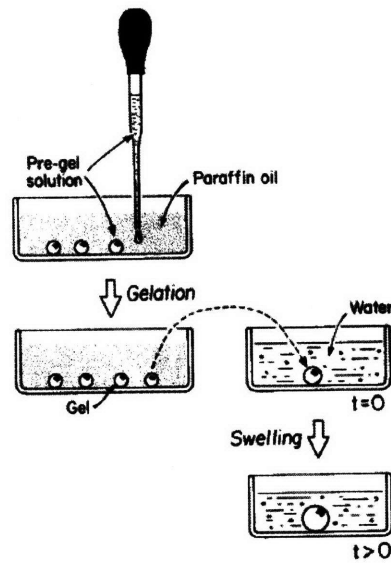


Fig. 2.2 – Swelling of hydrogels in the presence of water [41].

The equation of motion for a gel is that of Fickian diffusion (Eq. 2.7) [41, 58]. In the context of spherical gels this reduces to:

$$\frac{\partial u}{\partial t} = D \frac{\partial}{\partial r} \left\{ \frac{1}{r^2} \left[\frac{\partial}{\partial r} (r^2 u) \right] \right\} \quad (2.34)$$

where u is the local displacement, and D is the coefficient of diffusion of the network in the solvent. Exact solutions to this equation of motion depend on the geometry and boundary conditions. These solutions, however, are not the focus of this thesis. Rather, the governing equations are presented as a means of evaluating approximate response times and gaining insight into scaling factors. Scaling of this equation gives the following relationship for the response time of the swelling:

$$\tau \sim \frac{R^2}{D} \quad (2.35)$$

where R is a characteristic length (e.g. the radius), and τ is the time constant. The second power dependence on length implies that swelling timescales can be greatly decreased by reducing the sizes of the gels.

In order to determine the swelling of the gel, one must know the diffusion coefficient of the network in solution. This diffusivity is dependent upon a variety of factors, but is primarily due to the degree of crosslinking in the gel. The degree of crosslinking is related to the volume fraction, ϕ . Thus, diffusivity is proportional to the volume fraction as [68]:

$$D \propto \phi^{3/4} \quad (2.36)$$

It can also be expressed in terms of the material properties as [41, 58, 68]:

$$D = \frac{\kappa + \frac{4}{3}G}{f} \quad (2.37)$$

where κ is the bulk modulus, G is the shear modulus, and f is the friction factor between the chains and the solvent. One can see that this inherently implies that the crosslinking directly affects the moduli of the gel as well. The diffusion coefficient for poly(NIPAAm) is dependent upon temperature as is shown in Fig. 2.3 [68], and is on the order of $10^7 \text{ cm}^2/\text{s}$.

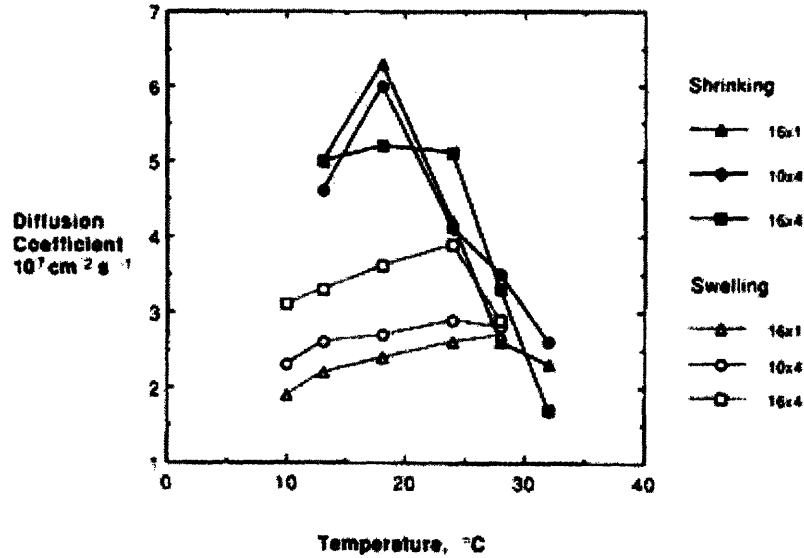


Fig. 2.3 – Diffusion coefficient of various poly(NIPAAm) gels as a function of temperature [68]. While the diffusivity changes significantly over the temperature range for shrinking, all coefficients are on the order of $10^7 \text{ cm}^2/\text{s}$.

Thus, for gels with characteristic lengths on the order of millimeters it can take hours for gels to reach equilibrium or even 50% of equilibrium (it would take about 1.9 hrs for a gel with $D = 10^7 \text{ cm}^2/\text{s}$ and a thickness of 1 mm). Microscale gels, however, can operate orders of magnitude faster due to the strong size dependence suggesting that even millisecond response could be possible [68].

2.1.3 Volume Phase Transitions in Gels Exhibiting LCST Behavior

Throughout the literature, a variety of descriptions of the swelling mechanisms of volume transition gels have been presented [43-60]. To date, there is still some debate over the true origins of the swelling phenomena. Some claim that the shrinking is the result of the dissolution of hydrogen bonds while others claim that it is the hydrophobic interactions that govern the shrinking. In reality, it is likely a combination of both effects.

A variety of models have been presented throughout the literature that propose to explain the LCST behavior exhibited in gels such as poly(NIPAAm). While they differ greatly, they mostly share the same four terms that affect the free energy: changes in the free

energy of mixing, changes in the free energy of elasticity, effects of osmotic pressure, and other specific interactions (e.g. hydrophobic interactions)[55].

The most basic model, though widely accepted as inaccurate, is known as the Flory-Huggins model [45]. This theory begins with the following expression for the change in free energy, ΔF :

$$\Delta F = \Delta F_M + \Delta F_{el} \quad (2.38)$$

where ΔF_M is the change in free energy of mixing [58],

$$\Delta F_M = \Delta H_M - T\Delta S_M \quad (2.39)$$

$$\Delta F_M = k_B T [(1 - \phi) \ln(1 - \phi) + \chi \phi(1 - \phi)] \quad (2.40)$$

and ΔF_{el} is the change in free energy of elasticity

$$\Delta F_{el} = \frac{3k_B T}{2N_x} \left[\left(\frac{\phi_0}{\phi} \right)^{2/3} - 1 - \ln \left(\frac{\phi_0}{\phi} \right) \right] \quad (2.41)$$

Here, ϕ is the volume fraction of polymers, N_x is the degree of polymerization in the portions of the chains between crosslinks, and χ is the Flory interaction parameter and is a measure of the interaction energy of the solvent divided by the thermal energy, $k_B T$.

$$\chi = \frac{\Delta H - T\Delta S}{k_B T} \quad (2.42)$$

While these expressions are not derived here, it is obvious to note that the elastic component comes from equipartition of energy in statistical mechanics. Thus, one should note that the Gaussian Chain model is assumed here where there are no energy penalties for interactions between the chain segments. The use of this simplistic model is one of the

shortcomings of the Flory-Huggins model since these polymer networks do not behave like ideal Gaussian chains.

These equations describe the free energy in a site of volume a^3 . Thus, one can determine the osmotic pressure as follows:

$$\Pi = \Pi_M + \Pi_{el} = -\frac{1}{a^3} \frac{\partial(\Delta F/\phi)}{\partial(1/\phi)} \quad (2.43)$$

where,

$$\Pi_M = -\frac{k_B T}{a^3} [\phi + \ln(1-\phi) + \chi\phi^2] \quad (2.44)$$

$$\Pi_{el} = \frac{k_B T \phi_0}{a^3 N_x} \left[\frac{1}{2} \left(\frac{\phi}{\phi_0} \right) - \left(\frac{\phi}{\phi_0} \right)^{1/3} \right] \quad (2.45)$$

Additionally, there is the possibility that the gel contains ionic groups. Such is the case with poly(NIPAAm) when a copolymer such as acrylic acid (AAc) is included. What results is a Donnan potential whose effects contribute to the osmotic pressure.

$$\Pi_{ion} = \frac{k_B T \phi_0 f}{a^3 N_x} \left(\frac{\phi}{\phi_0} \right) \quad (2.46)$$

where f is the number of ionic groups between the crosslinks. Thus, the total osmotic pressure is

$$\Pi = \frac{k_B T}{a^3} \left\{ \frac{\phi_0}{N_x} \left[\left(f + \frac{1}{2} \right) \left(\frac{\phi}{\phi_0} \right) - \left(\frac{\phi}{\phi_0} \right)^{1/3} \right] - \phi - \ln(1-\phi) - \chi\phi^2 \right\} \quad (2.47)$$

Assuming small values of ϕ , one can expand the natural logarithm terms using a power series:

$$\Pi = \frac{k_B T}{a^3} \left\{ \frac{\phi_0}{N_x} \left[\left(f + \frac{1}{2} \right) \left(\frac{\phi}{\phi_0} \right) - \left(\frac{\phi}{\phi_0} \right)^{\frac{1}{3}} \right] + \left(\frac{1}{2} - \chi \right) \phi^2 + \frac{\phi^3}{3} + \frac{\phi^4}{4} + K \right\} \quad (2.48)$$

$$\Pi = \frac{k_B T}{a^3} \left\{ - \left(\frac{\phi_0}{N_x} \right) \left(\frac{\phi}{\phi_0} \right)^{\frac{1}{3}} + \left(\frac{\phi_0}{N_x} \right) \left(f + \frac{1}{2} \right) \left(\frac{\phi}{\phi_0} \right) + A \phi_0^2 \left(1 - \frac{\Theta}{T} \right) \left(\frac{\phi}{\phi_0} \right)^2 + \frac{\phi_0^3}{3} \left(\frac{\phi}{\phi_0} \right)^3 + K \right\} \quad (2.49)$$

where, from Eq. 2.42,

$$A = \frac{k_B + 2\Delta S}{2k_B} \quad (2.50)$$

$$\Theta = \frac{2\Delta H}{k_B + 2\Delta S} \quad (2.51)$$

At equilibrium, the osmotic pressure is taken to be zero (although this assumption neglects mechanical stresses imposed by the crosslinks). This allows one to determine the temperature dependence upon the swelling ratio by noting that $\phi_0/\phi \equiv V/V_0$.

$$T|_{\Pi=0} = \frac{A\phi^2\Theta}{\left(\frac{\phi_0}{N_x} \right) \left[\left(f + \frac{1}{2} \right) \left(\frac{\phi}{\phi_0} \right) - \left(\frac{\phi}{\phi_0} \right)^{\frac{1}{3}} \right] - \phi - \ln(1-\phi) + \left(A - \frac{1}{2} \right) \phi^2} \quad (2.52)$$

The results of this model are presented against experimental measurements of poly(NIPAAm) with sodium acrylate is shown in Fig 2.4 [47]. The most obvious shortcoming of this model is its inability to predict discontinuous volume phase transitions in gels without ionic groups. This is because the only discontinuities arise from

the Donnan term. Interestingly, the model presented by Hirotsu and Tanaka (and later Shibaya and Tanaka [58]), directly contradicts their earlier experimental findings!

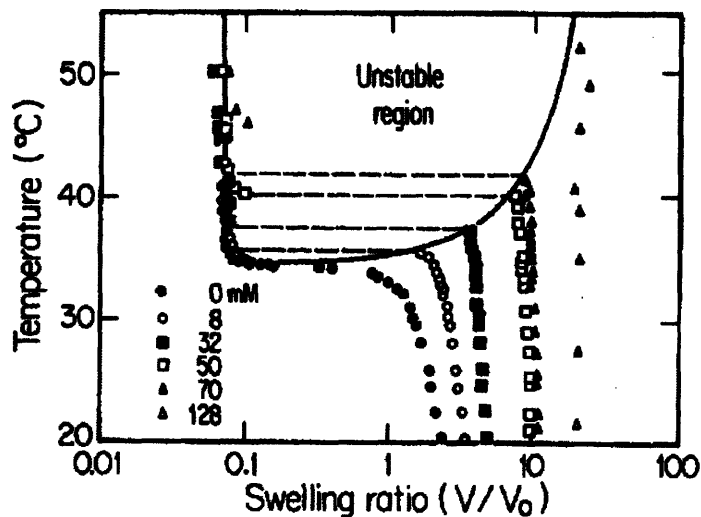


Fig 2.4 – Discontinuous volume phase transitions in poly(NIPAAm) shown for increasing amounts of ionizable groups (sodium acrylate). Note that no discontinuity is shown for the case of no ionizable groups [47].

In Hirokawa and Tanaka’s 1984 paper [43], they presented results showing a clear discontinuous volume phase transition for unmodified poly(NIPAAm) (Fig. 2.5). Ultimately, it is clear that the simple Flory-Huggins model presented and utilized by the Tanaka group along with many others does not sufficiently predict the behavior of poly(NIPAAm) and other LCST gels.

Additionally, part of the discrepancy comes from the fact the gel is treated as incompressible, which is obviously not the case. This assumption was made by Flory in his derivation of the ΔF_{el} term.

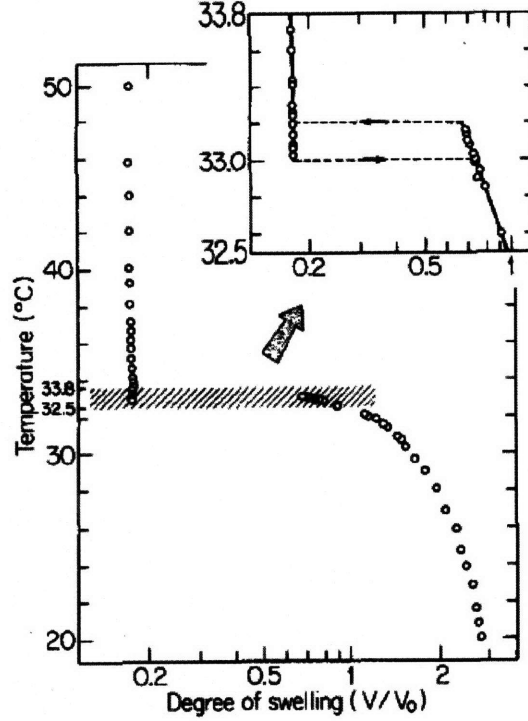


Fig. 2.5 – Volume phase transition in nonionic poly(NIPAAm)[43]. A clearly discontinuous phase transition is visible despite later papers by the author that seem to neglect these previously published results.

To improve upon the model Prange *et al.* no longer assumed incompressibility [51]. Instead, they include a partition function that represents hydrogen bonds according to lattice theory. The resultant expression for the change in chemical potential, μ , for the elastic component is described as:

$$\Delta\mu_{el} = \frac{k_B T}{N_x} \left\{ \frac{v_1}{v_u} \phi_0 (\rho - \rho_t) \left[\left(\frac{\phi}{\phi_0} \right)^{1/3} - \frac{\phi}{2\phi_0} \right] \right\} \quad (2.53)$$

where v_1 is the molar volume of solvent, v_u is the molar volume of monomer unit, ρ is the fraction of monomer units that are connected via crosslinks, and ρ_t is the fraction of chains in the network terminated by a crosslink only on one end, which do not contribute to elasticity.

While this model improves upon the Flory-Huggins model, it still uses the assumption of Gaussian chains [55]. Nonetheless, it does predict the discontinuous phase transition in the absence of ionic species. Lee *et al.* improved the model further by modifying the mixing term[50].

None of the aforementioned models, however, incorporate the hydrophobic interactions that likely affect the shrinking phenomena. Otake *et al.* show experimentally the importance of these interactions [53]. They suggest that the thermal mixing of molecules modeled by Tanaka with the Flory-Huggins model is useful for modeling the swelling at low temperatures, but that the shrinking at high temperatures corresponds to the hydrophobic interactions. In a later submitted, but earlier published paper they attempt to model these interactions[52]. In addition to the free energy of mixing, elasticity, and osmotic pressure, they add a term for the hydrophobic interactions.

$$\Delta F_{hydrophobic} = C_a + C_b T + C_c T^2 \quad (2.54)$$

where C_a , C_b , and C_c “are system dependent parameters.”

Additionally, they discard the mixing term presented by Tanaka, and instead propose the use of a term that includes elongation. They also alter the mixing and osmotic pressure terms to yield a free energy expression that is completely different than those previously presented. Rather than redefine all of the variables, their expression is shown below in terms of the variables as they define them.

$$\begin{aligned} \frac{\Delta G}{k_B T} = & \frac{3}{2} \left[n \ln \frac{(1 + \alpha\lambda)^{1+\alpha\lambda} (1 - \alpha\lambda)^{1-\alpha\lambda}}{(1 + \lambda)^{1+\lambda} (1 - \lambda)^{1-\lambda}} - N_{sc} \ln \alpha \right] + B_0 \phi_0 (T_r - 1) \left(\frac{1}{\alpha^3} - 1 \right) \\ & + [C_0 (T_r - 1) + C_1] \phi_0^2 \left(\frac{1}{\alpha^6} - 1 \right) - fm \ln(N_s + m) + (C_a + C_b + C_c) \frac{N_b p}{N_a k T} \end{aligned} \quad (2.55)$$

The exact relationship is not the focus here, but rather it is suggested that one recognize the overall form and number of fitting parameters. While the paper claims to more

accurately model the phase transition, the number of fitting parameters alone makes one wonder about the true utility of the model.

Additional models that further modify the original Flory-Huggins model have also been presented. The first modification is to simply alter the Flory interaction parameter to include a dependence on the volume fraction [57, 59]:

$$\chi = \frac{\Delta H - T\Delta S}{k_B T} + \chi_2 \phi \quad (2.56)$$

Here, χ_2 is an empirical parameter. Other models that attempt to include the effects of the hydrogen bonds present a separate form of χ that is a separable function of both temperature and volume fraction [46, 49]:

$$\chi = D(T)B(\phi) \quad (2.57)$$

where

$$B(\phi) = \frac{1}{1 - b\phi} \quad (2.58)$$

$$D(T) = \frac{z}{2} \left[\frac{\zeta + 2\zeta_{12}}{RT} + 2 \ln \left(\frac{1 + s_{12}}{1 + s_{12} \exp[\zeta_{12}/(RT)]} \right) \right] \quad (2.59)$$

Here, b is an empirical parameter, z is the lattice coordination number, ζ is the interchange energy, ζ_{12} is the difference in segmental interaction energy for non-specific interactions and specific interactions, and s_{12} is the degeneracy of those interactions.

2.1.4 Flow Through Porous Media

Because hydrogels are porous, they are by definition permeable to water. Thus, while, a valve made using poly(NIPAAm) will largely block the flow in a microfluidic channel, a small portion of liquid can be transported through the gel by both diffusive and pressure driven flows. One measure of the permeability of a porous medium is known as the hydraulic permeability, K . As was the case with the diffusivity, the permeability is largely controlled by the degree of crosslinking. By increasing the amount of crosslinking, the permeability decreases. Thus, the designer must carefully control the balance between the characteristics he cares about. By increasing the crosslinking, she increases the diffusivity (Eq. 2.36), thus decreasing the actuation time. Additionally, the modulus is increased resulting in a stronger gel. The problem, however, is that the swelling ratio is decreased when the crosslinking is increased. Thus, careful control of the crosslinking is needed.

Typically, flow through porous media is characterized using Darcy's Law. Darcy's Law relates the fluid velocity through the gel to the pressure as follows:

$$\nabla p = -\frac{\nu}{K} \quad (2.60)$$

Darcy's Law, however, cannot be used for the situation of a gel situated within a channel. This is because it does not allow for the use of the no-slip boundary condition. Instead, one should use Brinkman's Equation [69], which is a combination of Stokes' Equation and Darcy's Law:

$$\mu \nabla^2 \underline{v} - \frac{\nu}{K} \underline{v} - \nabla p = 0 \quad (2.61)$$

To determine the effects of the porosity of the gel on flow through the channel, the differential equation is solved for the two-dimensional geometry shown below (Fig. 2.6):

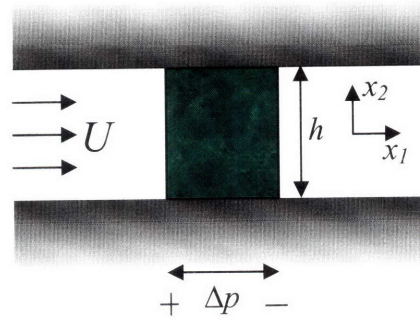


Fig. 2.6: Flow through a porous gel spanning the width of a channel

Here, fully developed flow is assumed. This assumption may be suspect as it is likely that the gel thickness is on the same order as the channel height; however, it greatly simplifies the modeling as variations in the velocity with respect to the x_1 direction can be neglected ($\partial v_1 / \partial x_1 = 0$). Additionally, it is assumed that there is no pressure variation across the height of the channel ($\partial p / \partial x_2 = 0$).

Applying these assumptions, the Brinkman equation reduces to the form:

$$\frac{\partial^2 v_1}{\partial x_2^2} - \frac{v_1}{\mu K} = \frac{1}{\mu} \frac{dp}{dx_1} \quad (2.62)$$

Since the pressure has no dependence on the x_2 direction, this is a non-homogeneous linear second-order ordinary differential equation with a general solution of the form:

$$v_1 = A_1 \exp(\omega x_2) + A_2 \exp(-\omega x_2) - K \frac{dp}{dx_1} \quad (2.63)$$

where,

$$\omega = \sqrt{\frac{1}{\mu K}} \quad (2.64)$$

Note that Eq. 2.62 is an ODE because the pressure has no dependence on the x_2 direction. The constants can be determined by employing the no-slip boundary conditions,

$$v_1(x_2 = \pm h/2) = 0 \quad (2.65)$$

and from symmetry:

$$\left. \frac{dv_1}{dx_2} \right|_{x_2=0} = 0 \quad (2.66)$$

These conditions yield:

$$A_1 = A_2 \equiv A \quad (2.67)$$

$$A = K \frac{dp}{dx_1} \left(\frac{1}{\exp\left(\frac{h\omega}{2}\right) + \exp\left(-\frac{h\omega}{2}\right)} \right) \quad (2.68)$$

Thus the velocity through the gel can be expressed as:

$$v_1 = K \frac{dp}{dx_1} \left[\frac{\exp(\omega x_2) + \exp(-\omega x_2)}{\exp\left(\frac{h\omega}{2}\right) + \exp\left(-\frac{h\omega}{2}\right)} - 1 \right] \quad (2.69)$$

This velocity distribution is shown in Figure 2.7 for a range of K values. As expected, lower K values result in higher fluidic resistances, and ultimately, much less fluid flow.

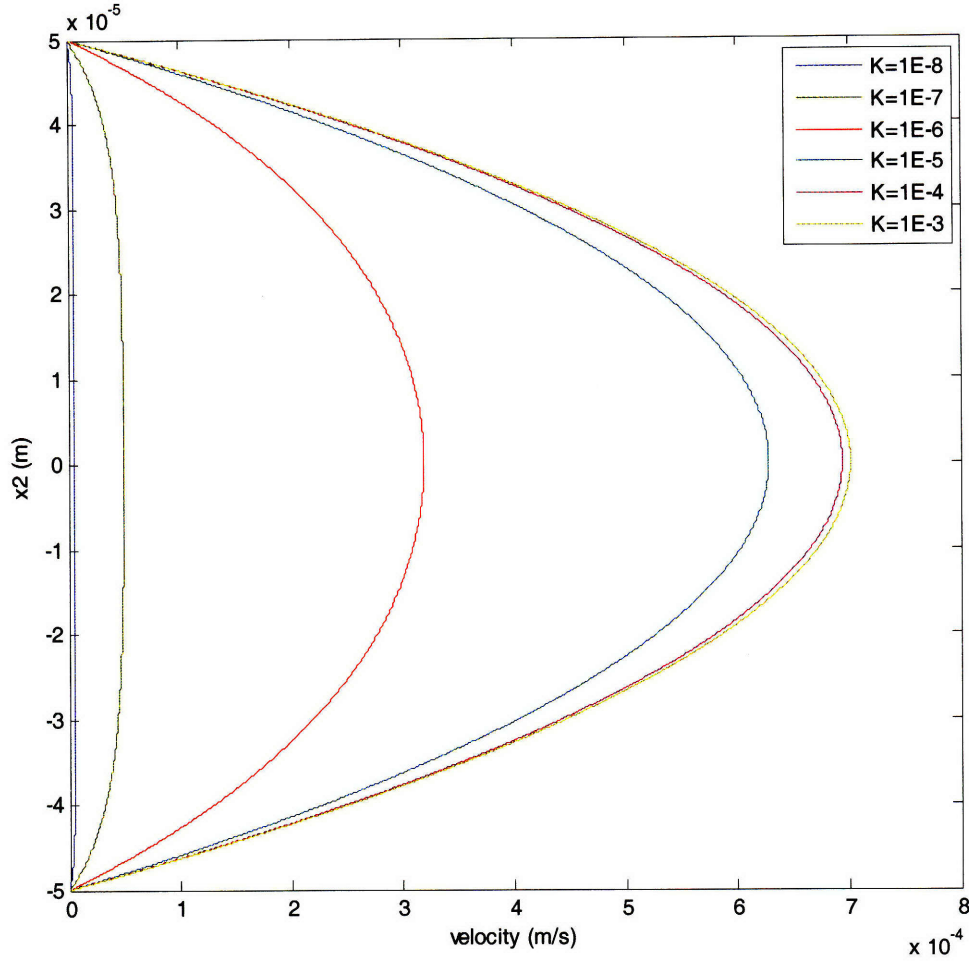


Fig. 2.7: Velocity profile of flow through porous media of various hydraulic conductivity values. Gels with higher hydraulic conductivities result in larger velocities. Values for this graph are based on the viscosity of water, a 100 μ m channel height, and a dp/dx_2 value of -500 Pa/m.

The volume flow is determined by integrating the velocity over the cross sectional area of the channel. Assuming that $\frac{dp}{dx_1}$ can be expressed as $\frac{\Delta p}{L}$ (where L is the gel length), the volume flow can be determined from the following integral:

$$Q = \int_{-\frac{h}{2}}^{\frac{h}{2}} v_1 w dx_2 = \int_{-\frac{h}{2}}^{\frac{h}{2}} \left[K \frac{\Delta p}{L} \left(\frac{\exp(\omega x_2) + \exp(-\omega x_2)}{\exp\left(\frac{h\omega}{2}\right) + \exp\left(-\frac{h\omega}{2}\right)} - 1 \right) \right] w dx_2 \quad (2.70)$$

This results in:

$$Q = \frac{\Delta p w K}{L} \left[\frac{2 \left(\exp\left(\frac{h\omega}{2}\right) - \exp\left(-\frac{h\omega}{2}\right) \right)}{\omega \left(\exp\left(\frac{h\omega}{2}\right) + \exp\left(-\frac{h\omega}{2}\right) \right)} - h \right] = \frac{\Delta p w K}{L} \left[\frac{2}{\omega} \tanh\left(\frac{h\omega}{2}\right) - h \right] \quad (2.71)$$

From this equation, one can define a fluidic resistance that relates pressure drop to volume flow through porous media in a channel. This is useful for lumped element modeling discussed later in this thesis. As is discussed in further detail in Section 2.5.2, one can define a fluidic resistance in a way that is analogous to Ohm's Law:

$$\Delta p = QR_{fluid} \quad (2.72)$$

For one-dimensional low Reynolds number flow through a porous rectangular channel, the fluidic resistance can be determined from Eq. 2.71:

$$R_{fluid} = \frac{L}{wK} \left[\frac{2}{\omega} \tanh\left(\frac{h\omega}{2}\right) - h \right]^{-1} \quad (2.73)$$

This model, however, is a significant simplification compared to the actual design. Because the design employs cylindrical geometry and a change in flow direction, the velocity and pressure gradients vary in all three dimensions. Also, as mentioned before, the assumption of fully-developed flow is likely not valid as the size of the hydrogel is on the same order as that of the channels. In order to get a better understanding of the flows through the actual valves, CFD methods must be employed as the Brinkman Equation cannot be simplified to a form that has an analytical solution. Nonetheless, the one-dimensional model presents a rough approximation of the results one might expect to see in the actual device.

It is interesting to note that the resistance is inversely proportional to the permeability. Thus, as is expected, increasing the crosslinking in the gel results in less fluid flow

through it. This is desirable in the application of a valve. As previously mentioned, however, this increase also reduces the amount of shrinking exhibited by the gel.

2.1.5 Compaction of Porous Media

Hydrogels tend to have much lower elastic moduli than conventional valve materials. Additionally, they are, by definition, poroelastic due to their crosslinked structure that is filled with water. Thus, stresses applied to the gels can cause them to become compressed and deformed more easily than viscoelastic solids like PDMS or other common valve materials. To model the deformation of the gel we will assume the setup shown in Fig. 2.8 where a mesh-like stop is placed behind the gel preventing solid movement in the positive x_2 direction, but allowing fluid flow. The resultant one-dimensional diffusion-like model is derived from a combination of the generalized Hooke's Law, conservation of mass, conservation of momentum, and Darcy's Law. Here Darcy's Law is used to simplify the model and eliminate possible solid movement and stresses in the x_2 direction. A more accurate depiction could be derived using Brinkman's Equation instead that would result in shear stresses and a two-dimensional deformation of the gel. Nonetheless, the one-dimensional model is useful for determine the approximate degree of compaction of the gel and general estimates of the allowable fluid flows.

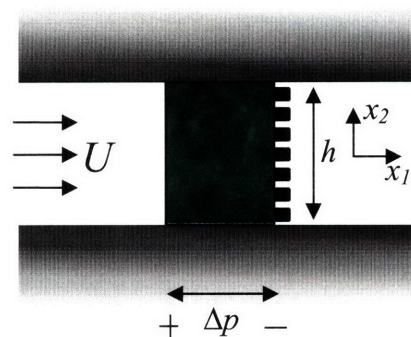


Fig. 2.8: Flow through a porous gel spanning the width of a channel with one side fixed

The total stress on the gel can be determined from the generalized Hooke's Law by including a term for the hydrostatic pressure:

$$\sigma_{ij}^{(T)} = 2G\varepsilon_{ij} + \lambda\delta_{ij}\varepsilon_{kk} - p\delta_{ij} \quad (2.74)$$

Here, $\sigma^{(T)}$ is the total stress, ε is the strain, G and λ are the first and second Lamé parameters respectively, δ_{ij} is the Kronecker delta, and p is the pressure. The first subscript refers to the face and the second refers to the direction. The Einstein summation convention is also used. Reducing this expression to one dimension results in:

$$\sigma_{11} = 2G\varepsilon_{11} + \lambda\varepsilon_{11} - p \quad (2.75)$$

G is often referred to as the shear modulus. Additionally, λ can also be rewritten in terms of the shear modulus and the bulk modulus, κ :

$$\lambda = \kappa - \frac{2}{3}G \quad (2.76)$$

Furthermore, it is common in tissue engineering to perform confined compression tests, whereby the sides and the bottom of the gel are prevented from expanding. This test results in a measurement of what is known as the “Longitudinal Modulus”. The longitudinal modulus, H , can be expressed as

$$H = 2G + \lambda \quad (2.77)$$

Substituting back into Eq. 2.75 results in

$$\sigma_{11} = H\varepsilon_{11} - p \quad (2.78)$$

As mentioned previously, Darcy’s law related the pressure to the fluid flow by the hydraulic conductivity:

$$\nabla p = -\frac{U}{K} \quad (2.79)$$

Here, \underline{U} is the local velocity of the fluid. In one-dimension this results in

$$U_1 = -K \frac{dp}{dx_1} \quad (2.80)$$

When only fluid motion is allowed, conservation of mass for an incompressible fluid is usually written as the divergence of the fluid velocity equating zero. However, because we are interested in motion of the solid, one should incorporate this motion into the mass conservation equation resulting in:

$$\nabla \cdot \underline{U} = -\nabla \cdot \underline{v}_s \quad (2.81)$$

where v_s is the velocity of the solid. In one-dimension this results in the following expression:

$$\frac{\partial U_1}{\partial x_1} = -\frac{\partial v_{s1}}{\partial x_1} = -\frac{\partial}{\partial x_1} \left(\frac{\partial u_1}{\partial t} \right) \quad (2.82)$$

Here, u is the displacement of the solid. Integrating over space results in:

$$U_1 = -\frac{\partial u_1}{\partial t} + U_0 \quad (2.83)$$

where U_0 is the initial fluid velocity. Finally, conservation of momentum can be expressed as

$$\nabla \cdot \underline{\underline{\sigma}}^{(r)} = 0 \quad (2.84)$$

In one dimension, all of the shear stresses are neglected and the expression is reduced to:

$$\frac{\partial \sigma_{11}}{\partial x_1} = 0 \quad (2.85)$$

Differentiating Eq. 2.78 results in

$$\frac{\partial \sigma_{11}}{\partial x_1} = H \frac{\partial \varepsilon_{11}}{\partial x_1} - \frac{\partial p}{\partial x_1} \quad (2.86)$$

The strain of the gel can be expressed in terms of the displacement of the gel as

$$\varepsilon_{ij} = \frac{1}{2} \left(\frac{\partial u_i}{\partial x_j} + \frac{\partial u_j}{\partial x_i} \right) \quad (2.87)$$

Combining equations 2.85, 2.86, and 2.87 results in

$$0 = H \frac{\partial^2 u_1}{\partial x_1^2} - \frac{\partial p}{\partial x_1} \quad (2.88)$$

Substituting Eq. 2.80 for the pressure gradient results in

$$-\frac{U_1}{K} = H \frac{\partial^2 u_1}{\partial x_1^2} \quad (2.89)$$

Incorporating the fluid velocity (Eq. 2.83) results in

$$\frac{\partial u_1}{\partial t} = HK \frac{\partial^2 u_1}{\partial x_1^2} + U_0 \quad (2.90)$$

This is the constitutive equation for the gel displacement. One should note that it takes the same form as a conventional diffusion equation where it is the solid that is diffusing. The “diffusivity” is equal to the product of the longitudinal modulus and the hydraulic permeability.

Using this equation one can determine the degree of compaction. First, steady state is assumed resulting in the time derivative going to zero:

$$0 = HK \frac{\partial^2 u_1}{\partial x_1^2} + U_0 \quad (2.91)$$

From integration, the displacement can be determined as follows:

$$d^2u_1 = -\frac{U_0}{HK} dx_1^2 \quad (2.92)$$

$$du_1 = -\frac{U_0}{HK} x_1 dx_1 + A \quad (2.93)$$

$$u_1 = -\frac{U_0}{2HK} x_1^2 + Ax_1 + B \quad (2.94)$$

The x_1 -axis is defined such that the right side of the gel is at $x_1 = 0$, and the left side is at $x_1 = -L$. Using this geometry, one can determine the following boundary conditions:

$$u_1 \Big|_{x_1=0} = 0 \quad (2.95)$$

$$\frac{du_1}{dx_1} \Big|_{x_1=-L} = 0 \quad (2.96)$$

These conditions result from the fact there is no displacement of the gel at $x_1 = 0$ and no strain at $x_1 = -L$. From them, one can determine the constants of integration to be:

$$A = -\frac{U_0 L}{HK} \quad (2.97)$$

$$B = 0 \quad (2.98)$$

Thus, the gel displacement and strain functions of position can be expressed as:

$$u_1 = -\frac{U_0}{HK} \left(\frac{x_1^2}{2} + Lx_1 \right) \quad (2.100)$$

$$\varepsilon_{11} = \frac{du_1}{dx_1} = -\frac{U_0}{HK} (x_1 + L) \quad (2.101)$$

To determine the total amount of compaction of the gel, one can integrate the strain over its length:

$$\Delta L = \int_0^L -\frac{U_0}{HK}(x_1 + L)dx_1 \quad (2.102)$$

$$\Delta L = -\frac{3U_0L^2}{2HK} \quad (2.103)$$

$$\frac{\Delta L}{L} = -\frac{3U_0L}{2HK} \quad (2.104)$$

As one might expect, the percent change in length increases with increased fluid velocity and decreases with increased longitudinal modulus and permeability. It is interesting to note, however, that it also increases with gel size. This suggests that larger gels will experience larger percentage change in length than smaller ones. Therefore, one should reduce the length of the gel in the direction of the flow in order to reduce the percentage compaction that the gel will experience.

2.2 Magnetic Heating

As was discussed in Section 1.4, heating of the poly(NIPAAm) by means of magnetic fields presents a variety of advantages to other methods in the application of microfluidic valves. This section focuses on the modeling of these mechanisms in terms of both power dissipation of the particles (2.2.1) and generation of the magnetic field using a planar MEMS magnetic coil (2.2.2).

2.2.1 Heat Generated by Magnetic Particles

2.2.1.1 Power Dissipation

In order to determine the heat generated by the magnetic nanoparticles, it is necessary to model their power dissipation. The analysis that follows is roughly based upon that carried out by Rosensweig [70]. The modeling begins with the statement of the first law of thermodynamics:

$$\delta U = \delta Q + \delta W \quad (2.105)$$

For adiabatic processes, $\delta U = 0$, and from electromagnetic theory we have:

$$\delta U = \underline{H} \cdot d\underline{B} \quad (2.106)$$

Here, \underline{H} is the magnetic field strength (magnetic field intensity) and \underline{B} is the magnetic flux density (magnetic field). \underline{B} and \underline{H} are related to each other through the magnetization, \underline{M} , by

$$\underline{B} = \mu_0(\underline{H} + \underline{M}) \quad (2.107)$$

where μ_0 is the magnetic permeability of free space ($4\pi \times 10^{-7}$). Combining Equations 2.106 and 2.107 yields the following expression for the increase in internal energy:

$$\Delta U = -\mu_0 \oint \underline{M} \cdot d\underline{H} \quad (2.108)$$

Since the magnetic field strength is oscillating, H can be expressed as

$$H(t) = H_0 \cos \omega t = \text{Re}[H_0 \exp(i\omega t)] \quad (2.109)$$

M is related to H through the complex magnetic susceptibility:

$$M = \chi H \quad (2.110)$$

where χ can be expressed in terms of its real and imaginary parts as[71]

$$\chi = \chi' + i\chi'' \quad (2.111)$$

Thus, the magnetization is

$$M(t) = \text{Re}[\chi H_0 \exp(i\omega t)] = H_0 (\chi' \cos \omega t + \chi'' \sin \omega t) \quad (2.112)$$

Inserting Equations 2.109 and 2.112 into Equation 2.108 yields

$$\Delta U = 2\mu_0 H_0^2 \chi'' \int_0^{2\pi/\omega} \sin^2 \omega t dt \quad (2.113)$$

The energy per cycle (Eq. 2.113) is then multiplied by the frequency ($f = \omega/2\pi$) to determine the power dissipation:

$$P = f\Delta U = \mu_0 \pi H_0^2 \chi'' f \quad (2.114)$$

From Debye relaxation, the susceptibility can be expressed as a function of frequency:

$$\chi = \frac{\chi_0}{1+i\omega\tau} = \frac{\chi_0}{1+\omega^2\tau^2} - i \frac{\omega\tau}{1+\omega^2\tau^2} \chi_0 \quad (2.115)$$

From inspection of Equations 2.111 and 2.115, one recognizes that the loss component of the susceptibility, χ'' , can be expressed as:

$$\chi'' = \frac{\omega\tau}{1+\omega^2\tau^2} \chi_0 \quad (2.116)$$

Combining this equation with the power dissipation equation (Eq. 2.114), results in

$$P = \mu_0 \pi H_0^2 f \chi_0 \frac{2\pi f \tau}{1+(2\pi f \tau)^2} \quad (2.117)$$

2.2.1.2 Relaxation Time Constants

The effective time constant, τ , that governs the power dissipation is comprised of two components [72, 73]. The first loss mechanism is known as Brownian Relaxation and refers to the fact that the nanoparticle must rotate within the fluid to align its magnetic moment to that of the applied field. The associated time constant for this relaxation can be expressed as

$$\tau_B = \frac{3\eta V_H}{k_B T} \quad (2.118)$$

Here, η is the viscosity of the fluid, k_B is the Boltzmann constant, T is the temperature, and V_H is the hydrodynamic volume which is related to the second area moment of inertia. This can be reduced to[61]

$$\tau_B = \frac{8\pi\eta R_H^3}{k_B T} \quad (2.119)$$

where R_H is the hydrodynamic radius.

Alternatively, the loss mechanism can in be the form of Néel Relaxation. This loss comes from when the magnetic moment within the particle itself realigns with the applied magnetic field. This is usually results when the frequency is too high for the particle to have enough time to rotate with the magnetic field. The time constant can be expressed as

$$\tau_N = \frac{\sqrt{\pi}}{2} \tau_0 \frac{\exp \Gamma}{\Gamma^{3/2}} \quad (2.120)$$

where

$$\Gamma = \kappa \frac{4\pi R^3}{3k_B T} \quad (2.121)$$

and κ is the anisotropy constant.

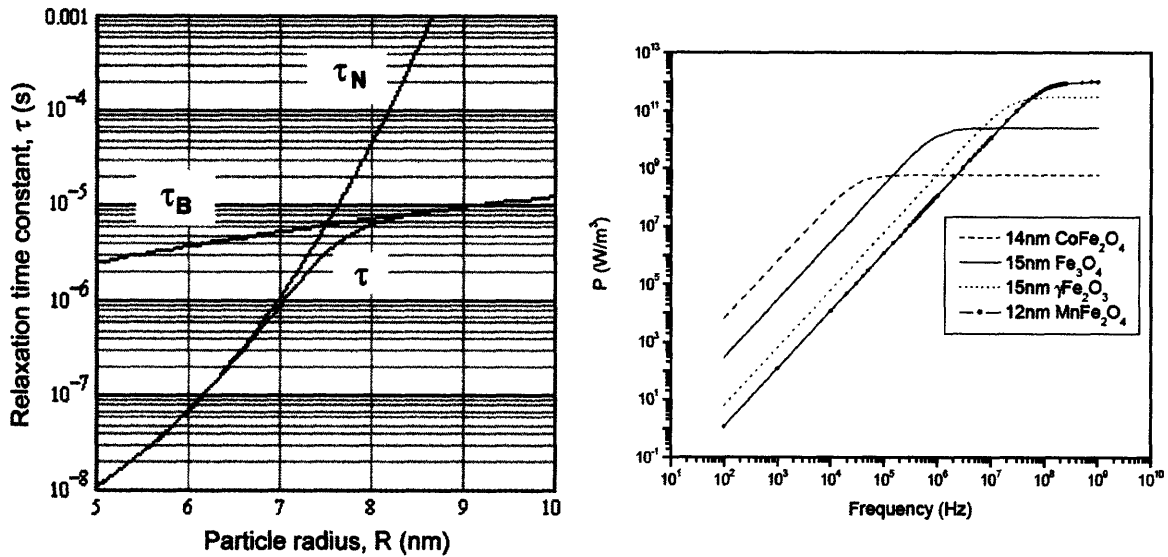


Fig. 2.9 – Dependence of loss mechanisms upon particle radius and magnetic field frequency. Néel Relaxation dominates at (a) small radii[70] and (b) high frequencies[61].

The effective time constant can be expressed as the two loss mechanisms in parallel.

Thus, the effective time constant is

$$\tau = \frac{\tau_B \tau_N}{\tau_B + \tau_N} \quad (2.122)$$

The relative importance of the two loss mechanisms depends on the frequency at which the magnetic field is oscillating. At high frequencies, Néel Relaxation dominates, whereas at low frequencies, the opposite is true. Also, since the dependence on particle radius is stronger in the case of Néel Relaxation, the particle size also affects the relative importance of the relaxation constants. Figure 2.9 shows these dependencies.

2.2.2 Magnetic Field Generation Using a Planar MEMS Magnetic Coil

In order to generate the heat dissipation from the magnetic nanoparticles, an oscillating magnetic field must be generated with sufficient strength as to generate temperature

changes in a reasonable amount of time. A variety of techniques could be employed in the generation of this field. For devices that are controlled entirely on-chip, it is desirable to have the coil patterned right onto the device. Additionally, the close proximity to the nanoparticles allows for the use of smaller currents and voltages to generate the same fields at the location of the nanoparticles.

One of the limitations of conventional microfabrication techniques is that the designs and fabrications are inherently two-dimensional due to the limitations of standard photolithographic techniques. Because of this limitation, it is in the interest of the designer to fabricate in-plane magnetic coils. Since such coils are not normally utilized at the macroscale, their modeling is not readily available. What follows in this section is a derivation of the equations necessary to model the magnetic field strengths for these geometries.

2.2.2.1 On-Axis Magnetic Field Strength

In determining the magnetic field strength, one must define the geometry of the magnetic coil. The geometry specified in the following analysis is shown in Figures 2.10 and 2.11. There are a variety of geometrical parameters that one can vary when designing the magnetic coil including the out-of-plane thickness of the coil, the outer radius of the coil, R , and the number of turns in the coil, N . For modeling purposes, the width of the coil, w , is set to be equivalent to the gap between adjacent rings of the coil, thus, it is not an independent parameter. Additionally, the coil radius, r_{coil} , is set to increase linearly with the angle, θ , according to the following expression:

$$r_{coil}(\theta) = \frac{R}{2\pi N} \theta \quad (2.123)$$

where θ can vary from 0 to $2\pi N$.

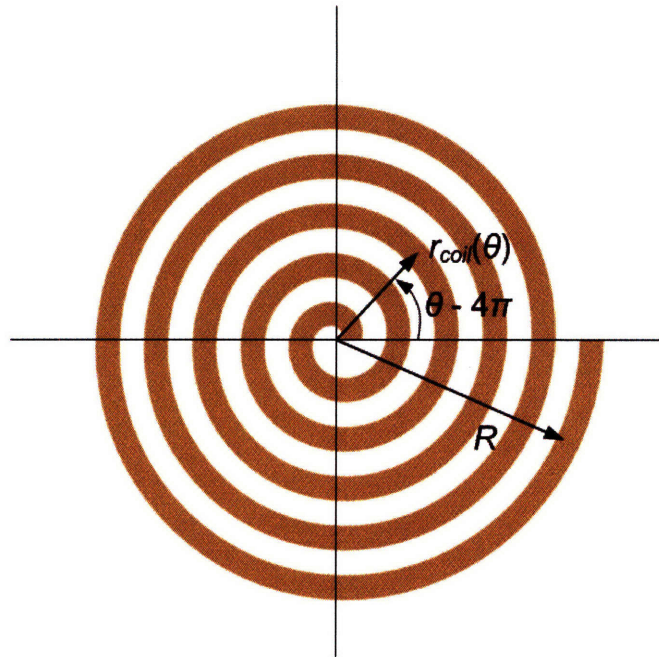


Fig. 2.10 – Magnetic coil dimensions with $N = 5$. θ varies from 0 to $2\pi N$ and r_{coil} varies from 0 to R where R is the outer radius of the circle.

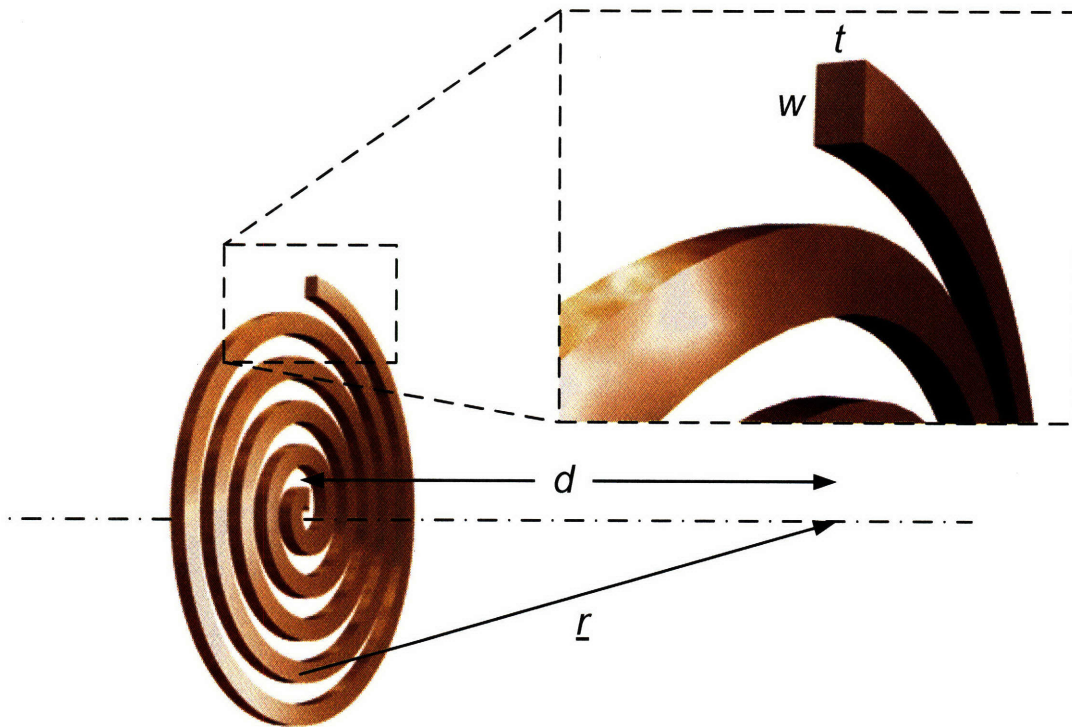


Fig. 2.11 – Magnetic coil out-of-plane dimensions. Thickness of the coil, t , is usually restricted by fabrication techniques. Distance between adjacent turns is equivalent to the width, w .

The magnetic field is determined as a function of on-axis distance, d , from the point of interest to the plane of the coil. In the actual device, this distance is largely limited by the fabrication techniques and substrates used. What follows is the derivation of the field strength based upon all of the aforementioned parameters.

The analysis starts, as good electromagnetic analyses should, with the statement of Maxwell's Equations (represented here in differential form):

$$\text{Gauss' Law for Electric Fields: } \nabla \cdot \epsilon_0 \underline{E} = \rho_e \quad (2.124)$$

$$\text{Faraday's Law of Induction: } \nabla \times \underline{E} = -\frac{\partial \underline{B}}{\partial t} \quad (2.125)$$

$$\text{Ampère's Law: } \nabla \times \underline{H} = \underline{J} + \frac{\partial \epsilon_0 \underline{E}}{\partial t} \quad (2.126)$$

$$\text{Gauss' Law for Magnetic Fields: } \nabla \cdot \underline{B} = 0 \quad (2.127)$$

where the variables are defined as follows:

\underline{E} – electric field intensity/strength

\underline{B} – magnetic flux density

\underline{H} – magnetic field intensity/strength

\underline{J} – electric current density

ρ_e – electric charge density

ϵ_0 – permittivity of free space

μ_0 – permeability of free space

One should note that the magnetic flux density and the magnetic field strength are related for linear, isotropic media by

$$\underline{B} = \mu \underline{H} \quad (2.128)$$

This allows one to convert between the field strength and the flux density by simply multiplying by the permeability. If the assumption of linear, isotropic media is not applicable, Equation 2.128 is no longer valid and one must include a magnetization term (see Eq. 2.107).

In the magnetostatic approximation, one can use Maxwell's Equations to derive a relationship between the magnetic field and the electric current. This equation is known as the Biot-Savart Law, and is expressed as

$$d\mathbf{B} = \frac{\mu_0}{4\pi} \frac{I d\mathbf{l} \times \hat{\mathbf{r}}}{r^2} \quad (2.129)$$

where I is the current, $d\mathbf{l}$ is the differential length along the coil, and $\hat{\mathbf{r}}$ is the unit vector in the direction of \mathbf{r} , and r is the magnitude of \mathbf{r} . \mathbf{r} is the vector from a given point on the coil the position of interest (see Fig. 2.11). From geometry it can be expressed in terms of the other parameters as

$$r^2 = d^2 + r_{coil}^2 = d^2 + \left(\frac{R}{2\pi N} \theta \right)^2 \quad (2.130)$$

One can express the magnitude of l in terms of known parameters as

$$l = r_{coil} \theta = \frac{R}{2\pi N} \theta^2 \quad (2.131)$$

Differentiating yields

$$dl = \frac{R}{\pi N} \theta d\theta \quad (2.132)$$

By examining Fig. 2.12, one recognizes that the angle between the z-axis and \underline{r} , α , can be expressed as

$$\alpha = \tan^{-1}\left(\frac{r_{coil}}{d}\right) = \tan^{-1}\left(\frac{R}{2\pi Nd}\theta\right) \quad (2.133)$$

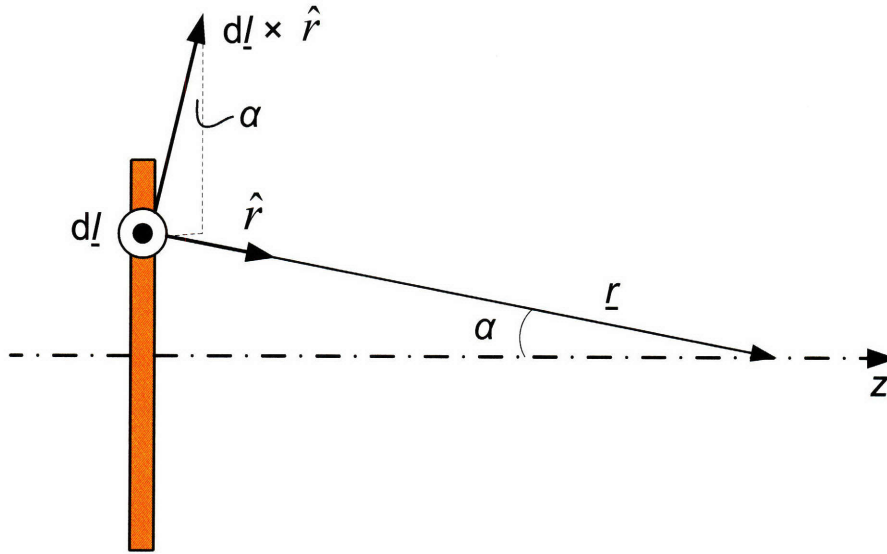


Fig. 2.12 – Geometry for determining cross-products

Thus, $d\underline{l} \times \underline{r}$ can be expressed as

$$\begin{aligned} d\underline{l} \times \underline{r} &= [dl \sin \alpha \hat{z} + dl \cos \alpha \hat{r}_{coil}] d\theta \\ d\underline{l} \times \underline{r} &= \frac{R}{\pi N} \theta \left[\sin\left(\tan^{-1}\left(\frac{R}{2\pi Nd}\theta\right)\right) \hat{z} + \cos\left(\tan^{-1}\left(\frac{R}{2\pi Nd}\theta\right)\right) \hat{r}_{coil} \right] d\theta \end{aligned} \quad (2.134)$$

where \hat{z} is the unit vector along the central axis and \hat{r}_{coil} is the radial unit vector in the plane of the coil. One can now evaluate for the magnetic flux density by integration:

$$\underline{B} = \frac{\mu_0 I}{4\pi} \int_0^l \frac{d\underline{l} \times \hat{r}}{r^2} \quad (2.135)$$

Since the integration is carried out around the coil, it is clear that the radial component of Eq. 2.134 almost exactly cancels out in the integration. This would be exact if the coil were concentric circles rather than a spiral. Because of this aspect, the radial term can be neglected.

$$\underline{B} = \frac{\mu_0 I}{4\pi} \int_0^{2\pi N} \frac{\frac{R}{\pi N} \theta \sin\left(\tan^{-1}\left(\frac{R}{2\pi N d} \theta\right)\right) \hat{z} d\theta}{d^2 + \left(\frac{R}{2\pi N} \theta\right)^2} \quad (2.136)$$

Evaluating this integral results in the following analytical expression for the magnetic flux density

$$\underline{B} = \mu_0 I \left\{ \frac{N}{R} \left[\ln(N) + 0.5 \ln\left(\left(\frac{R}{Nd}\right)^2\right) + \ln\left(1 + \sqrt{1 + \left(\frac{d}{R}\right)^2}\right) \right] - \frac{N}{R \sqrt{1 + \left(\frac{d}{R}\right)^2}} \right\} \hat{z} \quad (2.137)$$

Maintaining the assumption of linear, isotropic media, results in the following expression for the magnetic field strength:

$$\underline{H} = \frac{\mu_0}{\mu} I \left\{ \frac{N}{R} \left[\ln(N) + 0.5 \ln\left(\left(\frac{R}{Nd}\right)^2\right) + \ln\left(1 + \sqrt{1 + \left(\frac{d}{R}\right)^2}\right) \right] - \frac{N}{R \sqrt{1 + \left(\frac{d}{R}\right)^2}} \right\} \hat{z} \quad (2.138)$$

2.2.2.2 Off-axis Magnetic Field Strength

It is often of interest to the designer to know the intensity of the magnetic field at positions other than along the axis of the coil. This information gives insight into how quickly the field drops off with respect to distance off axis. Such information may be

necessary when determining if enough of field intensity is present in a dispersed area around the axis, or if it falls off quickly enough that neighboring elements do not feel its presence.

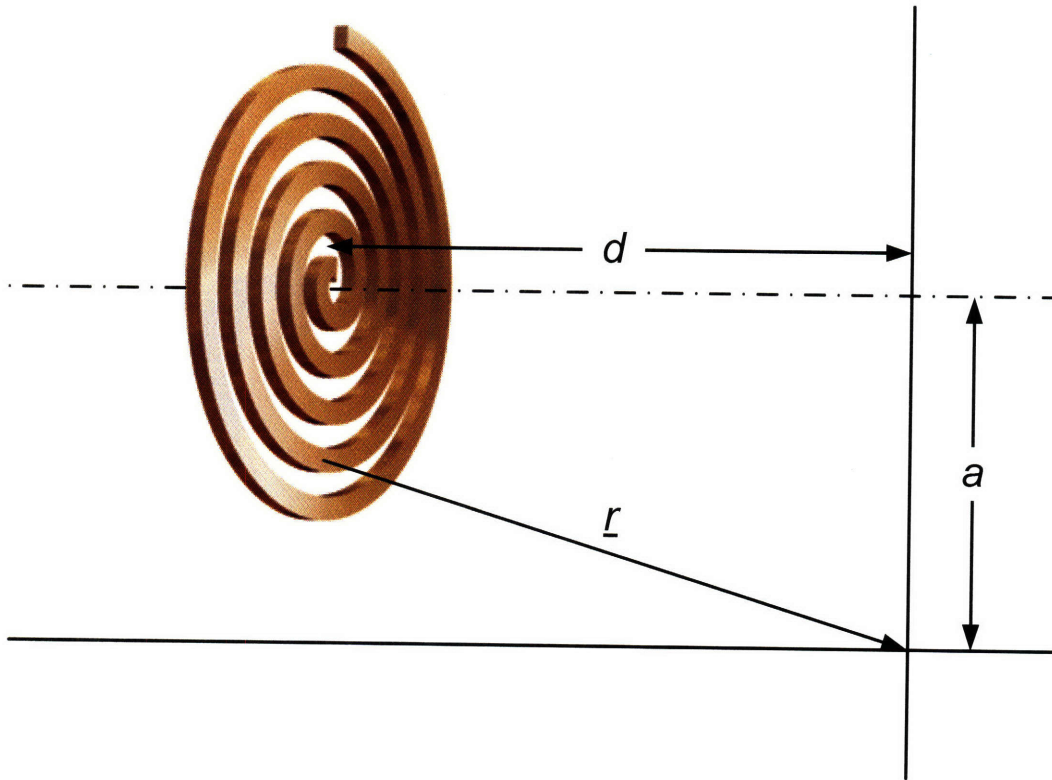


Fig. 2.13 – Off-axis magnetic coil geometry. The coil axis is displaced from the point of interest by a distance a .

The assumption applied to Eq. 2.134 that the radial components of the field could be neglected is no longer valid. This is due to the fact that they no longer cancel out when integrating around the coil since the \underline{r} vector is no longer roughly symmetric.

One can express the \underline{r} vector in Cartesian coordinates from inspection of the defined coordinate system (Fig. 2.13):

$$\underline{r} = -\hat{i}r_{coil} \cos \theta + \hat{j}(-a - r_{coil} \sin \theta) + d\hat{k} \quad (2.139)$$

$$\underline{r} = -\hat{i} \frac{R}{2\pi N} \theta \cos \theta + \hat{j} \left(-a - \frac{R}{2\pi N} \theta \sin \theta \right) + d\hat{k} \quad (2.140)$$

where \hat{i} , \hat{j} , and \hat{k} are the unit vectors along the x-, y-, and z-axes respectively. The magnitude of \underline{r} is found by taking the square root of the sum of the squares of the components:

$$|\underline{r}| = \sqrt{\left(\frac{R\theta}{2\pi N}\right)^2 \cos^2 \theta + a^2 + \frac{aR\theta}{\pi N} \sin \theta + \left(\frac{R\theta}{2\pi N}\right)^2 \sin^2 \theta + d^2} \quad (2.141)$$

$$|\underline{r}| = \sqrt{\left(\frac{R\theta}{2\pi N}\right)^2 + \frac{aR\theta}{\pi N} \sin \theta + a^2 + d^2} \quad (2.142)$$

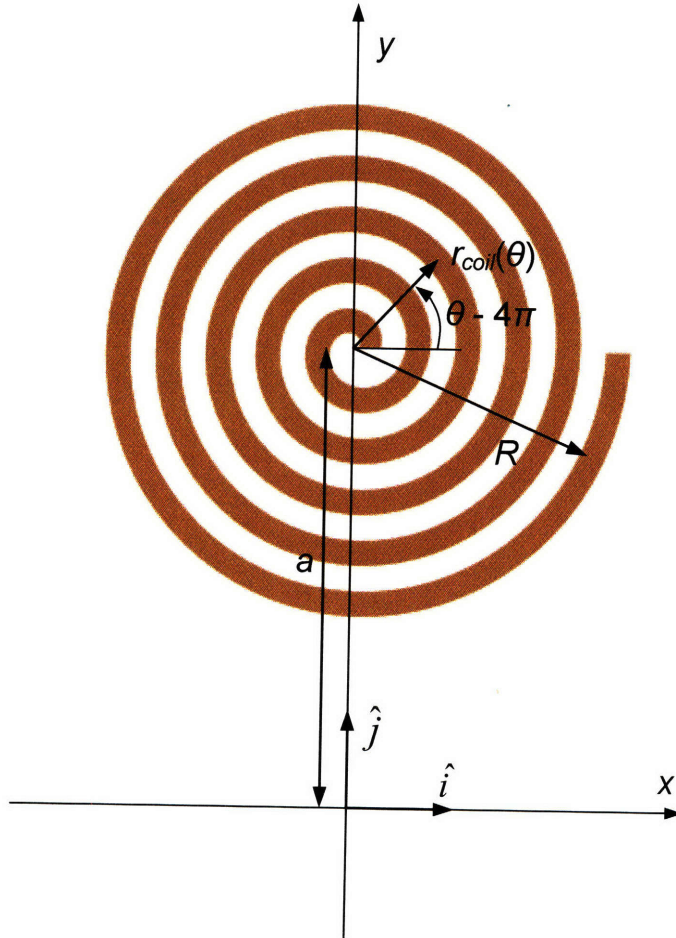


Fig. 2.14 – Displaced magnetic coil. Coil is displaced from the z-axis by a distance of a .

The differential length can be expressed as:

$$d\mathbf{l} = \left(\frac{R}{\pi N} \theta d\theta \right) (-\hat{i} \sin \theta + \hat{j} \cos \theta) \quad (2.143)$$

Next, one should determine $d\mathbf{l} \times \mathbf{r}$:

$$d\mathbf{l} \times \hat{\mathbf{r}} = \begin{vmatrix} \hat{i} & \hat{j} & \hat{k} \\ -\frac{R}{\pi N} \theta \sin \theta & \frac{R}{\pi N} \theta \cos \theta & 0 \\ \frac{R}{2\pi N} \theta \cos \theta & -a - \frac{R}{2\pi N} \theta \sin \theta & d \end{vmatrix} \quad (2.144)$$

$$d\mathbf{l} \times \hat{\mathbf{r}} = \frac{\left(\frac{R}{2\pi N} \theta \right)}{\sqrt{\left(\frac{R\theta}{2\pi N} \right)^2 + \frac{aR\theta}{\pi N} \sin \theta + a^2 + d^2}} \left[d(\hat{i} \cos \theta + \hat{j} \sin \theta) + \hat{k} \left(a \sin \theta + \frac{R}{2\pi N} \theta \right) \right] \quad (2.145)$$

Substituting these expressions into Eq. 2.129 allows one to calculate the magnetic field.

$$\mathbf{B} = \frac{\mu_0 I}{4\pi} \int_0^{2\pi N} \frac{\left(\frac{R\theta}{2\pi N} \right) \left[d(\hat{i} \cos \theta + \hat{j} \sin \theta) + \hat{k} \left(a \sin \theta + \frac{R}{2\pi N} \theta \right) \right]}{\left(\left(\frac{R\theta}{2\pi N} \right)^2 + \frac{aR\theta}{\pi N} \sin \theta + a^2 + d^2 \right)^{\frac{3}{2}}} d\theta \quad (2.146)$$

From Eq. 2.128, this equation can be related to the magnetic field strength by a factor of $1/\mu$ in the case of linear, isotropic media:

$$\underline{H} = \frac{\mu_0 I}{4\pi\mu} \int_0^{2\pi N} \frac{\left(\frac{R\theta}{2\pi N}\right) \left[d(\hat{i} \cos \theta + \hat{j} \sin \theta) + \hat{k} \left(a \sin \theta + \frac{R}{2\pi N} \theta \right) \right]}{\left(\left(\frac{R\theta}{2\pi N}\right)^2 + \frac{aR\theta}{\pi N} \sin \theta + a^2 + d^2 \right)^{\frac{3}{2}}} d\theta \quad (2.147)$$

This integral has no analytical solution. For the cases when the designer is interested in the field strength off axis, she must solve for it using numerical methods. This is done in Section 2.3.2 using MATLAB® (MathWorks).

2.3 Heat Transfer

2.3.1. General Heat Transfer Mechanisms

Heat transfer is a vastly important field throughout engineering due to the fact that there is some dissipative process involved in virtually any type of device or design. Usually, this dissipation manifests itself, at least to some degree, in heat transfer. While the purpose of this thesis is not to outline the basic principles of heat transfer, these mechanisms are the driving force behind the shrinking of the gel. Additionally, the thermal domain is coupled to all of the other domains both through dissipation and, conversely, the constitutive properties used in those domains. Thus, what follows is a brief overview of the heat transfer mechanisms so that they can be applied in subsequent sections.

There are three means by which the transport of heat can be carried out. They are conduction, convection, and radiation. Conduction is the mechanism by which molecular vibrations present at a certain temperature excite adjacent molecules with lower temperatures causing their temperatures to raise. Thus, the heat flow manifests itself through a gradient in temperature [74]:

$$q'' = -\kappa \nabla T \quad (2.148)$$

q'' is the heat flux (W/m^2) and κ is the thermal conductivity of the medium.

Convection is the method by which heat is transferred through the motion of a fluid. This can take the form of natural convection whereby differences in temperatures affect the fluid densities and induce fluid flow, or forced convection where an applied fluid flow imparts heat transfer. It is characterized by the following equation:

$$q'' = h(T_2 - T_1) \quad (2.149)$$

where h is the convective heat transfer coefficient. Often this value is not known as it depends upon many factors including fluid motion and surface geometry. For free convection, values range from 2-25 and 50-1000 $\text{W}/\text{m}^2\text{-K}$ for gases and liquids respectively. For forced convection these values range from 25-250 and 100-200000 $\text{W}/\text{m}^2\text{-K}$ [74].

Finally, radiation plays a significant role in heat transfer. Any matter that is at a finite temperature emits thermal energy in the form of radiation. Radiation does not require any medium as it manifests itself in electromagnetic waves. The heat flux can be expressed as,

$$q'' = \varepsilon \sigma_{SB} (T_2^4 - T_1^4) \quad (2.150)$$

where σ_{SB} is the Stefan-Boltzmann constant, and ε is the emissivity, which ranges from zero to one.

Conduction is usually the most dominant form of heat transfer in MEMS. Microfluidic devices, however, often include a lot of convection due to the fluid flow that is not present in conventional micromachined devices.

Since one is often concerned with a temperature distribution in a medium due to conduction, an expression should be derived that relates these quantities. Taking the divergence of Eq. 2.148 results in

$$\nabla \cdot q'' = -\nabla \cdot (\kappa \nabla T) \quad (2.151)$$

From thermodynamics,

$$Q = \rho \nabla c_p \Delta T \quad (2.152)$$

Thus, one can rewrite Eq. 2.151 in the form of a diffusion equation:

$$\frac{\partial T}{\partial t} = \left(\frac{\kappa}{\rho c_p} \right) \nabla^2 T + \frac{\mathcal{G}}{\rho c_p} = D_T \nabla^2 T + \frac{\mathcal{G}}{\rho c_p} \quad (2.153)$$

Here, it was obvious that the equation takes the form of a diffusion equation common in mass transport. Thus a thermal diffusivity, D_T , is defined as

$$D_T = \frac{\kappa}{\rho c_p} \quad (2.154)$$

This equation, which operates exactly like Fick's second law for diffusion, is extremely useful for the determination of temperature distributions and will be employed in the analyses that follow.

2.3.2 Heat Transfer in the Hydrogel

Heat is generated within the hydrogel by dissipation from the effects of the alternating magnetic fields on the nanoparticles. This power dissipation was derived in Section 2.2.1.1. Eq. 2.153 is a second order, linear, nonhomogenous partial differential equation

whose solution can be found using separation of variables. This method can be employed to find the transient temperature distribution within a cylindrical hydrogel disk.

To perform this analysis, one can make a variety of assumptions. As was shown in Section 2.1.5, there will be some amount of convection that occurs through the gel when a pressure is imposed that follows Darcy's Law. This convection is ignored following this model. A variety of assumptions such as no heat flux to the surrounding media, one-dimensional thermal diffusion, constant heat generation throughout the gel, and many more could be made to simplify the analysis with varying degrees of validity. Rather than impose these simplifications and carry out the full eigenfunction solution, a scaling analysis lends some insight into the time response of the heating.

First, we define characteristic variables: $t \sim \tau$ and $\nabla \sim 1/L$ where L is some characteristic dimension in the gel. One should usually choose a dimension over which heat is diffusing. Thus, one can rewrite Eq. 2.153 in terms of scaling relationships:

$$\frac{T}{\tau} \sim D_T \frac{T}{L^2} \Rightarrow \tau \sim \frac{L^2}{D_T} \quad (2.155)$$

Here, the power dissipation term is ignored since the parameter of interest is the characteristic time response of the gel due to conduction. Substituting the equation for thermal diffusivity (Eq. 2,154) results in:

$$\tau \sim \frac{L^2 \rho c_p}{\kappa} \quad (2.156)$$

2.3.3 Heat Transfer from Joule Heating of the Magnetic Coil

When current passes through a material that has some resistance (as all materials, save superconductors, do), energy is dissipated in the form of heat. This thermal dissipation is known as Joule heating and is the reason why cooling is often extremely important for

electronics. Such heating can be of significant concern for MEMS because the “wires” are so thin (metal film thicknesses are on the order of $\sim 50\text{nm}$ - $1\mu\text{m}$). Since the resistance scales with the area of the metal, the resistance can be high resulting in high energy dissipation ($P = I^2R$). Thus, it is important for the designer to determine the heat generated by the coil due to Joule heating to insure that neither the device area, nor the film itself gets too hot.

A variety of techniques and assumptions can be utilized to determine the temperature distribution in the device. They are depicted pictorially in Fig. 2.15. The first method, which is the most inaccurate, assumes that the coil is completely insulated from its environment, and thus there is no flux out of the sides of the coil. Additionally, it assumes that a one dimensional analysis can be used and that both ends are connected to thermal reservoirs of constant temperature. The solution is found through separation of variables of Eq. 2.153. This method is highly inaccurate since it results in extremely high temperatures under which conduction through the wafer and convection through the air would dominate.

The second approach is to make the assumption that, because the coil is so much more thermally conductive than the surrounding materials, it is at a constant temperature. It is also assumed that conduction through the wafer is the dominant transport mode over convection and radiation, and thus those modes are ignored. Additionally, one-dimensional heat transfer is again assumed. Despite these simplifications, this method is still much more accurate than the first method. It can be solved using the thermal diffusion equation with a constant temperature boundary condition on the top of the wafer, and a no-flux boundary condition at the bottom. The third method is the same as the second with the exception that convection is included on both sides of the wafer. This could be solved using a variety of methods; however, a lumped element model may be the simplest method (Section 2.5.3). Finally, finite element methods can be utilized to more exactly solve for the full three-dimensional temperature distribution.

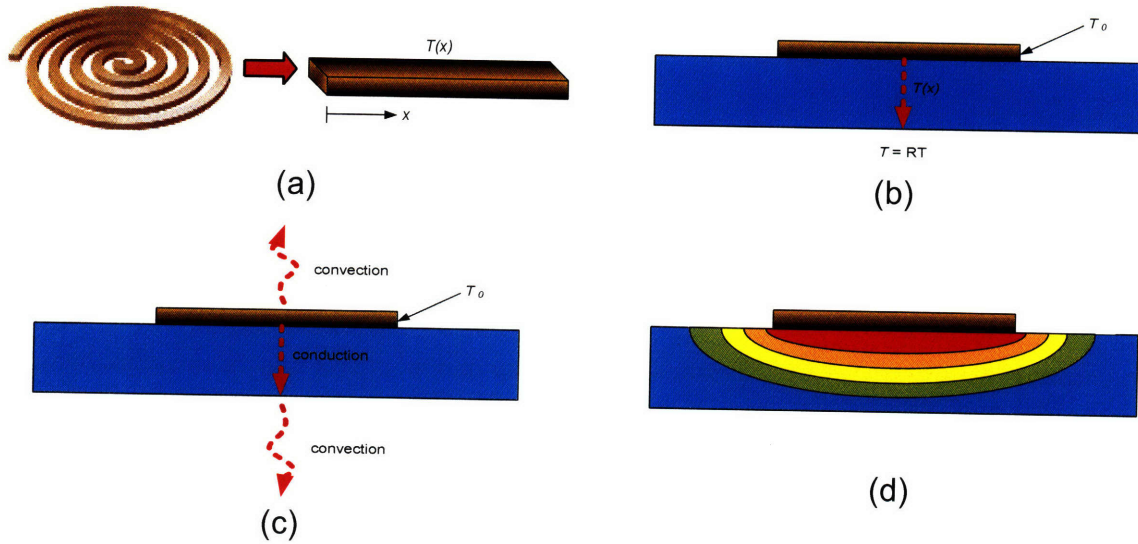


Fig. 2.15 – Four potential ways to model heat transfer from coil: (a) isolated 1D coil temperature distribution; (b) Constant temperature coil with 1D conduction through wafer; (c) same as (b), but with convection; (d) 3D FEM

The first and second methods can be analyzed using Eq. 2.153 with slightly different boundary conditions. Also, one should note that the generation term is a function of temperature. This is due to the fact that the resistance value of a material depends on temperature. It is related by the thermal coefficient of resistance, α_R , as [75]

$$R = R_0 [1 + \alpha_R (T - T_0)] \quad (2.157)$$

Here, R_0 is the resistance value of the material at temperature T_0 . Noting that the power dissipation of a resistor is $I^2 R$, one can restructure the thermal diffusion equation to the form shown below.

$$\frac{\partial T}{\partial t} = D_T \nabla^2 T + \frac{I^2 R_0}{\rho c_p \nabla} [1 + \alpha_R (T - T_0)] \quad (2.158)$$

Analyzing this equation in one-dimension and assuming steady state, results in the following expression:

$$\frac{\partial^2 T}{\partial x^2} + A^2 T = B \quad (2.159)$$

where,

$$A^2 = \frac{I^2 R_0 \alpha_R}{\rho c_p \forall D_T} \quad (2.160)$$

$$B = \frac{I^2 R_0}{\rho c_p \forall D_T} (\alpha_R T_0 - 1) \quad (2.161)$$

In the first model, it is stated that either end of the coil are connected to a thermal reservoir. Thus, the boundary conditions are $T = 0$ at $x = 0$ and $x = L$ where L is the length of the coil. While the temperature is not actually zero at those locations, temperature is a relative variable, and thus the absolute temperature is found after the analysis by adding a constant to the solution.

Eq. 2.159 is a second order, constant coefficient ODE with a solution of the following form:

$$T = C \sin(Ax + \varphi) + \frac{B}{A^2} \quad (2.162)$$

Applying the boundary conditions:

$$0 = C \sin(\varphi) + \frac{B}{A^2} \quad (2.163)$$

$$0 = C \sin(AL + \varphi) + \frac{B}{A^2} \quad (2.164)$$

Thus, one can determine the phase angle from the following expression:

$$\sin(AL + \varphi) = \sin(\varphi) \quad (2.165)$$

$$\varphi = \frac{\pi - AL}{2} \quad (2.166)$$

This results in the following value for the prefactor when substituted into Eq. 2.162:

$$C = -\frac{B}{A^2 \sin\left(\frac{\pi - AL}{2}\right)} \quad (2.167)$$

Thus, the temperature distribution can be expressed as:

$$T_{SS}(x) = \frac{(\alpha_R T_0 - 1)}{\alpha_R} \left[\frac{\sin\left(x \sqrt{\frac{I^2 R_0 \alpha_R}{\rho c_p L w t D_T}} + \frac{1}{2} \left(\pi - \sqrt{\frac{I^2 L R_0 \alpha_R}{\rho c_p w t D_T}} \right)\right)}{\sin\left(\frac{1}{2} \left(\pi - \sqrt{\frac{I^2 L R_0 \alpha_R}{\rho c_p w t D_T}} \right)\right)} + 1 \right] \quad (2.168)$$

This solution, however, is very unrealistic due to the fact that there is no conduction or convection off of the top or bottom of the coil. In reality, these effects are very important, and should be considered. Thus, the second model, which includes conduction through the wafer, is employed. Here, it is assumed that, because the coil is so thermally conductive compared to the glass wafer, it can be approximated as a constant temperature:

$$T(x=0) \equiv T_0 \quad (2.169)$$

Eq. 2.153 is again employed under the one-dimensional steady-state assumptions, but without the heat generation term:

$$D_T \frac{\partial^2 T}{\partial x^2} = 0 \quad (2.170)$$

From integration, the temperature distribution is found to be the following:

$$T = \frac{1}{2D_T} x^2 + C_1 x + C_2 \quad (2.171)$$

The boundary conditions are $T(x=0) = T_0$ and $dT/dx = 0$ at $x = t_w$ where t_w is the thickness of the wafer. The second boundary condition arises out of the assumption that there is no conduction or convection through the air, and thus there is no heat flux off of the end of the wafer. Thus, the constants of integration are,

$$C_2 = T_0 \quad (2.172)$$

$$C_1 = -\frac{t_w}{D_T} \quad (2.173)$$

Thus, the temperature distribution through the wafer is

$$T = \frac{1}{D_T} \left(\frac{x^2}{2} - t_w x \right) + T_0 \quad (2.174)$$

This model is far more accurate since conduction through the wafer is allowed. The third method includes convection and is discussed more in Section 2.5.3 where it is approached using a lumped element method. Finally, the designer should use a full three-dimensional finite element approach to get a true description of the temperature distribution in the system.

2.4 Rate Limiting Mechanisms and Time Response of Swelling

The valves proposed in this thesis utilize a variety of different actuation mechanisms that span across many of the domains. Modeling approaches to deal with this complexity are discussed throughout this chapter; however, it is important to make note of their relative significance in terms of the transient response of the valves. It is intuitive that the establishment of the electrical signals and magnetic field occur over timescales that are essentially instantaneous in comparison to the other timescales of the model. Thus, the rate limiting element in the actuation of the valves likely comes from one of the following three mechanisms: heat dissipation from the magnetic nanoparticles, heat conduction throughout the gel, or the swelling kinetics.

First, conduction of heat in the gel is compared to the swelling behavior. Convection through the gel is assumed to be negligible. This is the basic assumption made throughout this thesis in order for the valve to operate as designed. The validity of this assumption can be tested using models like the one presented in Section 2.1.4. Knowledge of the hydraulic permeability of the gel is necessary to carry out the analysis, and because this value is highly dependent on crosslinking ratio among other things, it is not performed here. Instead it is assumed that conduction is the main mode of heat transfer within the gel. From Eq. 2.153, it is known that the time for conductive heat transfer scales like

$$\tau_{cond} \sim \frac{L^2}{D_T} \quad (2.175)$$

where D_T is the thermal diffusivity of the poly(NIPAAm) gel. While there are undoubtedly many mechanisms that contribute to the swelling and shrinking of poly(NIPAAm) hydrogels, their mass transport can also be modeled to first order using a Fickian approach as was discussed in Section 2.1.2. Thus the response time roughly follows the same scaling:

$$\tau_{shrink} \sim \frac{L^2}{D} \quad (2.176)$$

where D is the diffusivity of the network in the water. Thus, to compare the relative rate constants, one only needs to compare their diffusivities. Fig. 2.16 shows experimental results presented by Gehrke for the time response of both mechanisms [68].

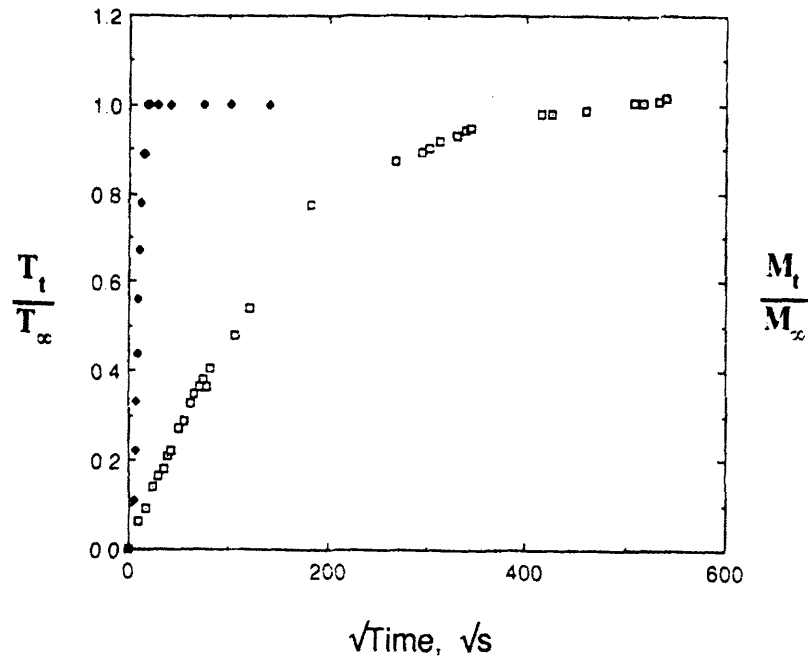


Fig. 2.16 – Time response of heat transport and mass transport in poly(NIPAAm)[68]. Closed circles are temperature and open squares are mass. The thermal diffusivity is much higher than the diffusivity of the water molecules suggesting that the swelling of the gel is the rate limiting factor.

Gehrke reports the following temperature dependent thermal diffusivity values for poly(NIPAAm) hydrogels noting that they are about four orders of magnitude higher than the mass diffusivities of the gels: $2.3 \times 10^{-3} \text{ cm}^2/\text{s}$ at 35°C and $3.0 \times 10^{-3} \text{ cm}^2/\text{s}$ at 47°C [68]. From these values and this figure, it is easy to see that the mass transport of the water molecules out of the hydrogel is rate limiting over the heat conduction through the gel.

2.5 Lumped Element Modeling

2.5.1 Background of Lumped Element Modeling

One of the most powerful tools for modeling systems both at the macroscale and microscale is known as lumped element modeling. This form of modeling allows one to simplify complex behavior by “lumping” most of the details into one parameter: the *element*. Lumped elements are discrete elements that can exchange energy with other elements [75]. The most common examples of lumped elements are found in electronics where portions of circuits and devices are lumped into elements such as resistors or capacitors. Similarly, in the mechanical domain, physical systems are often lumped into systems of springs, masses, and dashpots. These models are extremely useful for electromechanical transducers [76, 77], but can be applied to essentially any physical domain including, but not limited to, acoustics[78], fluids, and heat transfer.

Lumped element modeling is extremely powerful, not only because of the simplicity it provides, but also because of the tools it allows one to use. One can define analogous lumped electrical components for the elements in the other domains allowing for multi-domain system analysis to be performed completely through the analysis of circuits. Because so many tools, such as SPICE, exist for circuit analysis, static and transient responses to systems can be easily analyzed using computers.

Determination of how systems are lumped in the various domains depends both upon the governing physics of those domains and a choice of conventions. Just as is the case for components in electrical systems, one should define their across and through variables. These variables define what quantities are measured by their difference between to ports of the elements and what quantity flow through a port of the element. For the electrical domain these are voltage and current respectively since a voltage is measured “across” an element, whereas a current flows through one.

In a generalized domain, one can define an effort, e , a generalized displacement, q , a flow, f , which is the time derivative of the displacement, and a generalized momentum, p , which is the time integral of the effort. Through a relation to this domain, one can define an effort and flow variable for each of the domains being analyzed. Choice of

conventions leads to a choice of which electrical element to use to represent an element in another domain assuming that the analysis is being performed in the electrical domain. In this thesis, the $e \rightarrow V$ (effort \rightarrow voltage) convention is used since voltage is naturally a relative variable. What follows in the rest of Section 2.5 is a description of the lumping conventions used in the various domains as they pertain to the analysis of the valve design.

2.5.2 The Fluidic Domain

The circuit analogy to variables in the fluidic domain is perhaps the most intuitive. In general, the pressure, P , is chosen to be the effort variable since it is defined in relative terms. Volume flow, Q , is used as the flow variable. For Poiseuille flow, an expression for pressure as a function of volume flow (Eq. 2.33) was derived in Section 2.1.1.2. To create a lumped parameter, one can define the pressure drop at a length L as:

$$\Delta P = \frac{12\mu L}{h^3 w} Q \quad (2.177)$$

By analogy to Ohm's law, one can define the fluidic resistance, R_{Pois} , as

$$R_{Pois} = \frac{12\mu L}{h^3 w} \quad (2.178)$$

An interesting thing to note about this expression is the strong dependence upon the height of the channel. It is important to remember that the height is the smallest dimension, and that the assumption that $w \gg h$ is made when assuming that the flow is one-dimensional. This expression, of course, is not exact, but provides important insight into how the various parameters scale. For non-rectangular geometry, the scaling essentially remains the same, although the prefactors are different. While it is not derived here, it is important to have an expression for the fluidic resistance when the channel

height and width are on the same scale. For this situation the fluidic resistance can be described as [79]

$$R_{w-h} = \frac{12\mu L}{wh^3} \left[1 - \frac{h}{w} \left(\frac{192}{\pi^5} \sum_{n=1,3,5}^{\infty} \frac{1}{n^5} \tanh\left(\frac{n\pi w}{2h}\right) \right) \right]^{-1} \quad (2.179)$$

2.5.3 The Thermal Domain

In the thermal domain the conventions of generalized displacement cannot be used. This is because the first law of thermodynamics suggests that the generalized displacement should be entropy; however, entropy is not a conserved quantity, and thus should not be used as the generalized displacement. Thus, for the thermal domain a separate convention is defined wherein heat energy, I_Q , is the flow variable and temperature, T , is the effort [75]. This makes sense since temperature is naturally a relative quantity like pressure and voltage.

Another useful characteristic of this convention is that a direct analogy can be applied between the thermal and electrical domains since the governing equations are exactly the same:

$$q'' = -\kappa \nabla T \Leftrightarrow J = -\sigma_e \nabla V \quad (2.180)$$

Thus, one can define a thermal resistance for conduction that is directly analogous to an electrical resistance:

$$R_T = \frac{1}{\kappa} \frac{L}{A} \quad (2.181)$$

where L is the length, and A is the cross-sectional across which heat is conducting. Also, by analogy to Eq. 2.149, one can define an equivalent thermal resistance for convection:

$$R_T = \frac{1}{hA} \quad (2.182)$$

Unfortunately, radiation is nonlinear with temperature. So, in order to define an equivalent resistance, one must linearize by deciding whether the two bodies are at vastly different temperatures or whether they are approximately equal. This manifests itself in terms of something of the form of

$$R_T = 4\sigma_{SB}F_{12}AT_2^3 \quad (2.183)$$

Additionally, one can define a means of thermal energy storage as a thermal capacitance:

$$C_T = c_p\rho\forall \quad (2.184)$$

where c_p is the specific heat, ρ is the mass density, and \forall is the volume. Because there is no kinetic energy in the thermal domain, there is no equivalent inductor.

Using these elements, one can now define equivalent circuits to model the response of the system. The model that is lumped in the following analysis is based upon the third technique described in Section 2.3.3 and depicted schematically in Fig. 2.15(c). Radiation is neglected in this model since there is no second body of interest. Fig. 2.17 shows the equivalent circuit for this model. Again, the coil is assumed to be at a constant temperature since its thermal conductivity is much higher than that of the substrate or the surrounding air. Thus, the heat transfer modes are conduction through the wafer and convection through the air. These are represented as the thermal resistances R_{wafer} and R_{air} respectively. Additionally, a thermal capacitance, C_{wafer} , is defined for the wafer. Convection occurs from both the top and bottom of the wafer.

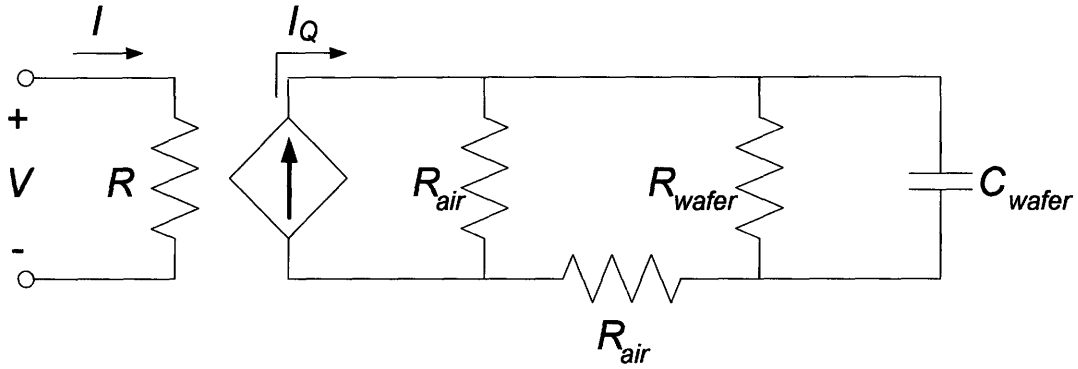


Fig. 2.17 – Circuit representation of lumped element model of the thermal domain. Power dissipation manifests itself in the Joule heating of the magnetic coil.

One can define an equivalent impedance for this circuit:

$$Z_{eq} = R_{air} \parallel \left(R_{wafer} \parallel \frac{1}{C_{wafer}s} + R_{air} \right) \quad (2.185)$$

$$Z_{eq} = \frac{R_{air} \left(R_{air} + \frac{R_{wafer}}{R_{wafer} C_{wafer} s + 1} \right)}{\left(2R_{air} + \frac{R_{wafer}}{R_{wafer} C_{wafer} s + 1} \right)} \quad (2.186)$$

Recognizing that the heat current is the power dissipation, the following transfer function can be described for the system:

$$H(s) = \frac{\Delta T}{I^2(s)R} = \frac{R_{air} \left(R_{air} + \frac{R_{wafer}}{R_{wafer} C_{wafer} s + 1} \right)}{\left(2R_{air} + \frac{R_{wafer}}{R_{wafer} C_{wafer} s + 1} \right)} \quad (2.187)$$

Using this transfer function, the system can be analyzed under a variety of operating conditions and frequencies. This analysis is performed when selecting the appropriate magnetic coil parameters in Section 4.3.2

2.5.4 Viscoelasticity as a Lumped Element System

Section 2.1.2 describes the mechanical behavior of the polymer gel as a homogeneous isotropic linear elastic solid. While this description is convenient for modeling purposes due to its simplicity, it fails to predict the transient behavior under various loads. A viscoelastic model is often applied to gels in order to predict the creep behavior due to a step input of stress or stress relaxation behavior resulting from a step input of strain. These models are constructed upon mechanical lumped element models consisting of springs and dashpots. The most widely accepted of these models is the Kelvin model (3-element model), which combines both the Voigt model for predicting creep and the Maxwell model for predicting stress relaxation [80-82]. It is shown in Figure 2.18.

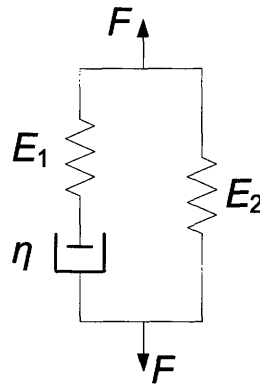


Fig. 2.18 – Lumped element model for viscoelastic solids.

The governing equation for this system is

$$F + \frac{\eta}{E_2} \frac{dF}{dt} = E_1 x + \eta \left(1 + \frac{E_1}{E_2} \right) \frac{dx}{dt} \quad (2.188)$$

Using this model, one can predict the transient response of the gel to various types of loading. Unfortunately, the effective moduli and damping coefficients were not measured, so integration of this viscoelastic representation of the gel is not utilized in the final design of the valves.

2.5.5 Coupling

One of the greatest benefits of using equivalent circuits with lumped element modeling is the ability to relate multiple domains. This was actually already done in Section 2.5.3 where the electrical and thermal domains were related by the electrical resistor and the dependent current source in the electrical and thermal circuits respectively. In that case the power was equated in both the circuits. This was somewhat of a special situation due to the fact that in the thermal domain the product of the across and through variables is not power as it is in the other domains. In the case of energy conserving transducers, one can relate the two circuits using a transformer or a gyrator. It is useful to think of these multidomain systems as transducers since stimuli in one domain gives rise to responses in another. Thus, one could think of the proposed valve as an electro-magneto-themo-chemo-mechanical transducer (Fig. 2.19). While all of the elements of this system are not modeled using a lumping approach in this thesis, suffice it to say that such a feat could be performed. In this case, such an approach was deemed unnecessary; however, parts of the lumped element approach were used in the design of the device for certain domains. Because the various domains are so highly coupled in this system (Fig. 2.19), the lumped approach can be unreasonable for modeling the entire system. In order to get a true description of the interactions finite element methods should be employed.

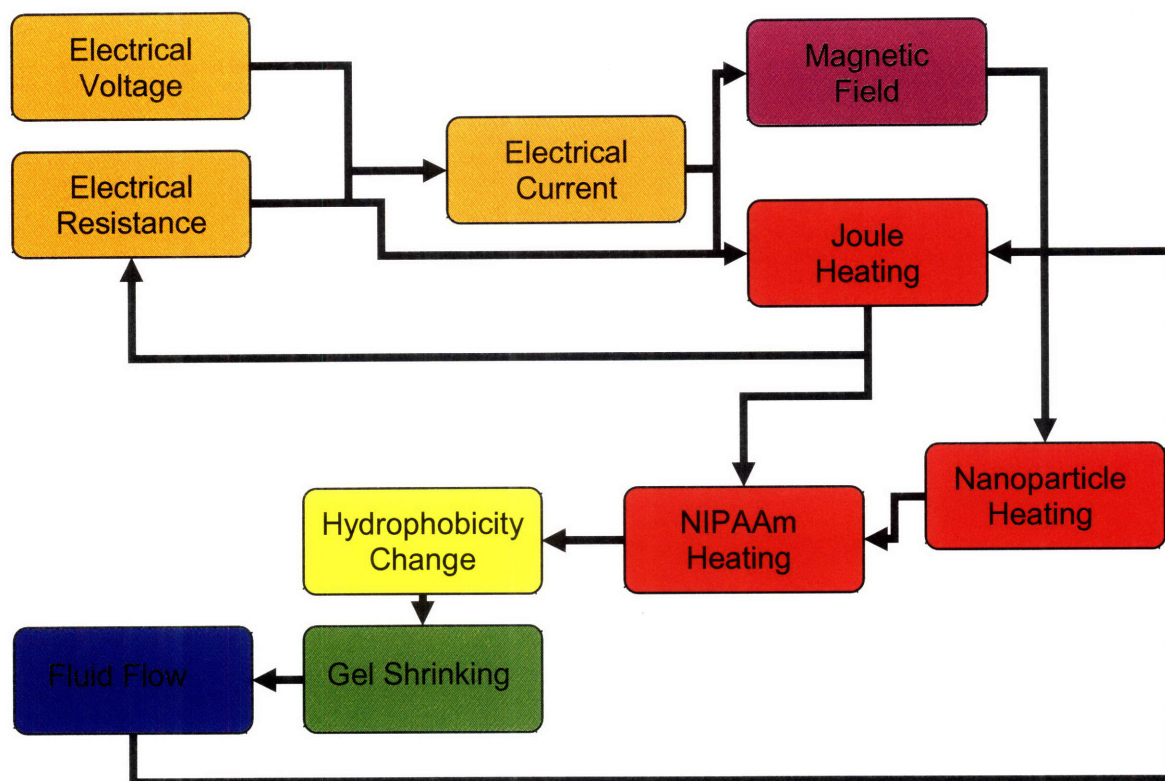


Fig. 2.19 – Relationships between the various domains of the overall system: orange = electrical; magenta = magnetic; red = thermal; yellow = chemical; green = mechanical; blue = fluidic.

2.6 Oxygen Inhibition

Free radical polymerization stimulated by UV irradiation is an important concept in this thesis. The device design and fabrication described in Chapters 3-5 require polymerization of the poly(NIPAAm) hydrogels by exposure to UV light much like conventional photolithography. This is performed by including photoinitiators in the prepolymer solution. The details of this process will be discussed in more detail in the aforementioned chapters. One important concern, however, is the presence of oxygen molecules and their role in the inhibition of the polymerization. After formation, the free radicals prefer to react with the oxygen. Thus, when oxygen concentrations are high, polymerization of the monomers does not take place since the rate constant of oxidation (5×10^8 L/mol-sec) is much higher than polymerization (10^3 L/mol-sec)[83]. The polymerization to oxidation competition is depicted schematically in Fig. 2.20.

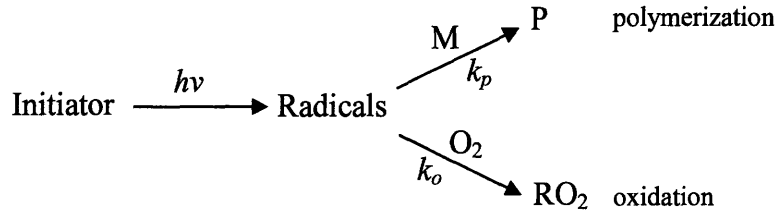


Fig. 2.20 – Balance of reaction rates. Schematic based off of [83]. k_p is the reaction rate associated with polymerization and k_o is the oxidation reaction rate.

The situation of interest is polymerization within a channel where there is a known constant concentration of oxygen at the channel wall. It is desirable to know what distance within the solution that the oxygen penetrates. The presence of this oxygen near the wall will prevent polymerization within this region [84-86]. Fick’s second law of diffusion is used to model the mass transport:

$$\frac{\partial C_{O_2}}{\partial t} = D\nabla^2 C_{O_2} + R \quad (2.189)$$

where C_{O_2} is the concentration of O_2 , D is the coefficient of diffusion of O_2 in the solution, and R is the generation term, which in this case refers to the reactions.

Assuming first-order irreversible reaction kinetics, one can write R as

$$R = -kC_{O_2} \quad (2.190)$$

One can also assume steady state and model the transport in one dimension. This results in the following expression:

$$D \frac{\partial^2 C_{O_2}}{\partial x^2} = kC_{O_2} \quad (2.191)$$

This is a second order, linear, homogeneous ordinary differential equation with a known solution of the form

$$C_{O_2} = A_1 e^{-\lambda x} + A_2 e^{\lambda x} \quad (2.192)$$

Here, $\lambda = \sqrt{k/D}$, and A_1 and A_2 are found from the boundary conditions. The first boundary condition is obvious: a known constant concentration at the wall. The second boundary condition comes from examination of the Damköhler number. The Damköhler number, Da , is a comparison between the reaction rate to the diffusion rate and is defined as [87]:

$$Da \equiv \frac{k_n C_0^{n-1} L}{D} \quad (2.193)$$

where n is the order of the reaction, C_0 is a known concentration, and L is a characteristic length. In situations where $Da \gg 1$, the reaction dominates the diffusion. Previously reported values for Da are 100-1000 for similar situations [84]. Because the reaction occurs much more quickly than the diffusion, it is fair to say that the oxygen concentration far away from the wall is zero. Thus, the two boundary conditions are:

$$C_{O_2}(x=0) = C_{wall} \quad (2.194)$$

$$C_{O_2}(x \rightarrow \infty) = 0 \quad (2.195)$$

Substituting these boundary conditions into Eq. 2.192, results in the following values for the constants:

$$A_1 = C_{wall} \quad (2.196)$$

$$A_2 = 0 \quad (2.197)$$

Thus, the concentration distribution as a function of position is:

$$C_{O_2} = C_{wall} e^{-x\sqrt{\frac{k}{D}}} \quad (2.198)$$

From this equation, one can determine a characteristic length through which the oxygen molecules penetrate:

$$L_p \sim \sqrt{\frac{D}{k}} \quad (2.199)$$

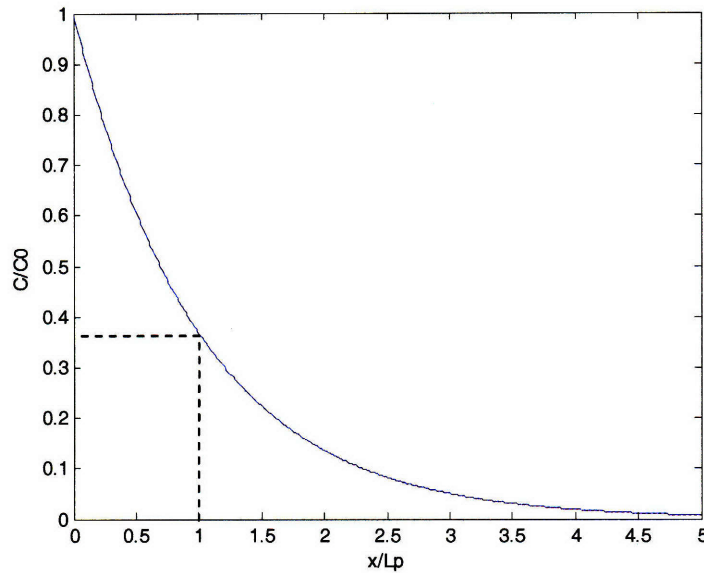


Fig. 2.21 – Oxygen concentration as a function of distance from the wall.

The reaction rate, k , was already established to be 10^3 L/mol-sec; however, the diffusivity still needs to be determined. The most common method for the determination of the diffusion coefficient is the use of the Stokes-Einstein equation [88]:

$$D = \frac{RT}{N_A} \frac{1}{6\pi\mu r} = \frac{k_B T}{6\pi\mu r} \quad (2.200)$$

where k_B is the Boltzmann Constant (1.38×10^{-23} J/K), T is the absolute temperature, μ is the fluid viscosity, and r is the particle radius. Of course, this equation presumes that the

particle of interest, in this case an O₂ molecule, is spherical. Various formulations of this equation have been presented with modifications to more precisely match empirical data [89]. Using the Wilke-Chang model, the diffusion coefficient can be estimated as $6 \times 10^{-10} \text{ m}^2/\text{s}$. Thus, the oxygen inhibition layer should be on the order of ones to tens of microns.

3. Systems Approach to the Design of the Device

3.1 Principles of Axiomatic Design

In order to design the microfluidic valve, the design method known as Axiomatic Design was employed. This design methodology was invented by Professor Nam Suh. It is an extremely useful technique for designing all types of systems and is particularly helpful for determining instances and causes of inhibitory coupling within a design.

Axiomatic design is based upon two fundamental axioms [90]:

- *Independence Axiom*: A complete set of independent functional requirements (FRs) can and must be maintained
- *Information Axiom*: The best design is the one that minimizes the information content

Here, he defines functional requirements to be the aspects of the design that must be satisfied. The functional requirements should encompass the complete set of requirements of the design. Additionally, they must be completely independent from one another.

Because it is possible to satisfy a set of functional requirements with multiple sets of design parameters (DPs), the best design is the one that has the lowest information content. Information content is a measure of the probability of success of a design parameter satisfying its corresponding functional requirement. The information content for a particular FR is defined as:

$$I = -\log_2 P \quad (3.1)$$

where I is the information content and P is the probability of success. The information content of a design is useful in determining how robust a particular design is. It is also closely related to the complexity of the design.

One of the major challenges of any type of design is determining the parameters to use in order to satisfy the needs of the design. Axiomatic design proposes the use of a single design parameter for each functional requirement. Ideally, the designer will be able to tune the design parameters as to only impact the functional requirements she intends to. If a design has fewer DPs than FRs, the design is coupled because one or more DPs affects more than one FR. If the design has more DPs than FRs, the design is redundant because multiple DPs affect the same FR.

A useful technique in axiomatic design is the use of matrix notation:

$$\{FR\} = [A]\{DP\} \quad (3.2)$$

where $\{FR\}$ and $\{DP\}$ are column vectors and $[A]$ is the system matrix. For a system with three FRs and three DPs Eq. 3.2 is equivalent to:

$$\begin{Bmatrix} FR_1 \\ FR_2 \\ FR_3 \end{Bmatrix} = \begin{bmatrix} A_{11} & A_{12} & A_{13} \\ A_{21} & A_{22} & A_{23} \\ A_{31} & A_{32} & A_{33} \end{bmatrix} \begin{Bmatrix} DP_1 \\ DP_2 \\ DP_3 \end{Bmatrix} \quad (3.3)$$

Examination of the system matrix is particularly useful for determining the coupling of a design. Systems with diagonal system matrices (Eq. 3.4) represent an uncoupled system since each design parameter affects only one functional requirement.

$$\begin{Bmatrix} FR_1 \\ FR_2 \\ FR_3 \end{Bmatrix} = \begin{bmatrix} X & 0 & 0 \\ 0 & X & 0 \\ 0 & 0 & X \end{bmatrix} \begin{Bmatrix} DP_1 \\ DP_2 \\ DP_3 \end{Bmatrix} \quad (3.4)$$

Systems with triangular matrices (Eq. 3.5) represent decoupled systems. Decoupled systems are ones in which one or more design parameters affect more than one functional requirement, but can be resolved by adjusting the parameters in a particular order. That is

to say one should adjust the parameters that affect multiple FRs first and adjust the ones that affect only one last.

$$\begin{Bmatrix} FR_1 \\ FR_2 \\ FR_3 \end{Bmatrix} = \begin{bmatrix} X & 0 & 0 \\ X & X & 0 \\ X & X & X \end{bmatrix} \begin{Bmatrix} DP_1 \\ DP_2 \\ DP_3 \end{Bmatrix} \quad (3.5)$$

Often it is necessary to rearrange the order of the FRs and DPs in order to determine whether a design is decoupled or coupled. There are many advantages to using the principles of Axiomatic Design to develop a design. This thesis will not delve into the various corollaries and theorems presented by Professor Suh as it is not the intent of this thesis. Nonetheless, a description of how the axiomatic framework was applied to generate a design for a poly(NIPAAm)-based microfluidic valve will be heavily discussed throughout the remainder of this chapter.

3.2 Top Level Functional Requirements

When defining the functional requirements of a design it is important to consider the wishes of the consumer/end-user. The design of the microfluidic valve had three top-level functional requirements:

- FR_1 – Valve must shrink to allow flow
- FR_2 – Valves must have the ability to be individually actuated at time of user's choice
- FR_3 – Valves should be able to be scaled up for large scale integration

Obviously, there is a wide range of design parameters that could be used to satisfy these functional requirements. Because the focus of this research was the implementation of poly(NIPAAm), the first design parameter (DP_1) was to use the heating and resultant shrinking of poly(NIPAAm) gels to open valves.

In order to activate individual valves at specific times, the design parameter of addressable electronically controlled heating was DP_2 . That is to say that the valves will

be actuated using some electronic signal. The detailed method of doing this will be determined in the lower-level FRs and DPs.

The third design parameter (DP_3) was to use photolithography to pattern all of the valves on a single substrate at once. This way many devices could be made across a wafer and have all their valves fabricated with a single step.

The system matrix for this design is shown in Equation 3.6:

$$\begin{Bmatrix} FR_1 \\ FR_2 \\ FR_3 \end{Bmatrix} = \begin{bmatrix} X & 0 & 0 \\ X & X & 0 \\ 0 & 0 & X \end{bmatrix} \begin{Bmatrix} DP_1 \\ DP_2 \\ DP_3 \end{Bmatrix} \quad (3.6)$$

One can see that the design is decoupled. The only design parameter that affects more than one FR is DP_1 . This is because the use of poly(NIPAAm) places specific requirements on the feasibility of using electronically controlled heating.

3.3 Original Design

The original design of the valve was simple in that it could easily be fabricated in most basic microfluidic channels. The design was to create posts in the centers of PDMS channels where the valve would be. A poly(NIPAAm) prepolymer solution would then be drawn into the channels. Photolithography would be used to polymerize the prepolymer solution at the locations of the valves. This would result in plugs of NIPAAm that would close the channel and be held in place by the posts. The channel would then be heated causing the plugs to shrink and allowing for the unpolymerized solution to be washed out.

The process of polymerizing the valves is shown in Figure 3.1. Fig. 3.1(a) shows the device prior to polymerization of the valve. It consists of a PDMS channel bonded to a glass substrate. NIPAAm prepolymer solution containing photoinitiators is flowed into

the channel (Fig. 3.1(b)) Subsequently, the valve is polymerized using photolithography with a mask aligner to create the solid poly(NIPAAm) plug around the post (Fig. 3.1(c)). Finally, the prepolymer is flushed out using water and other solvents.

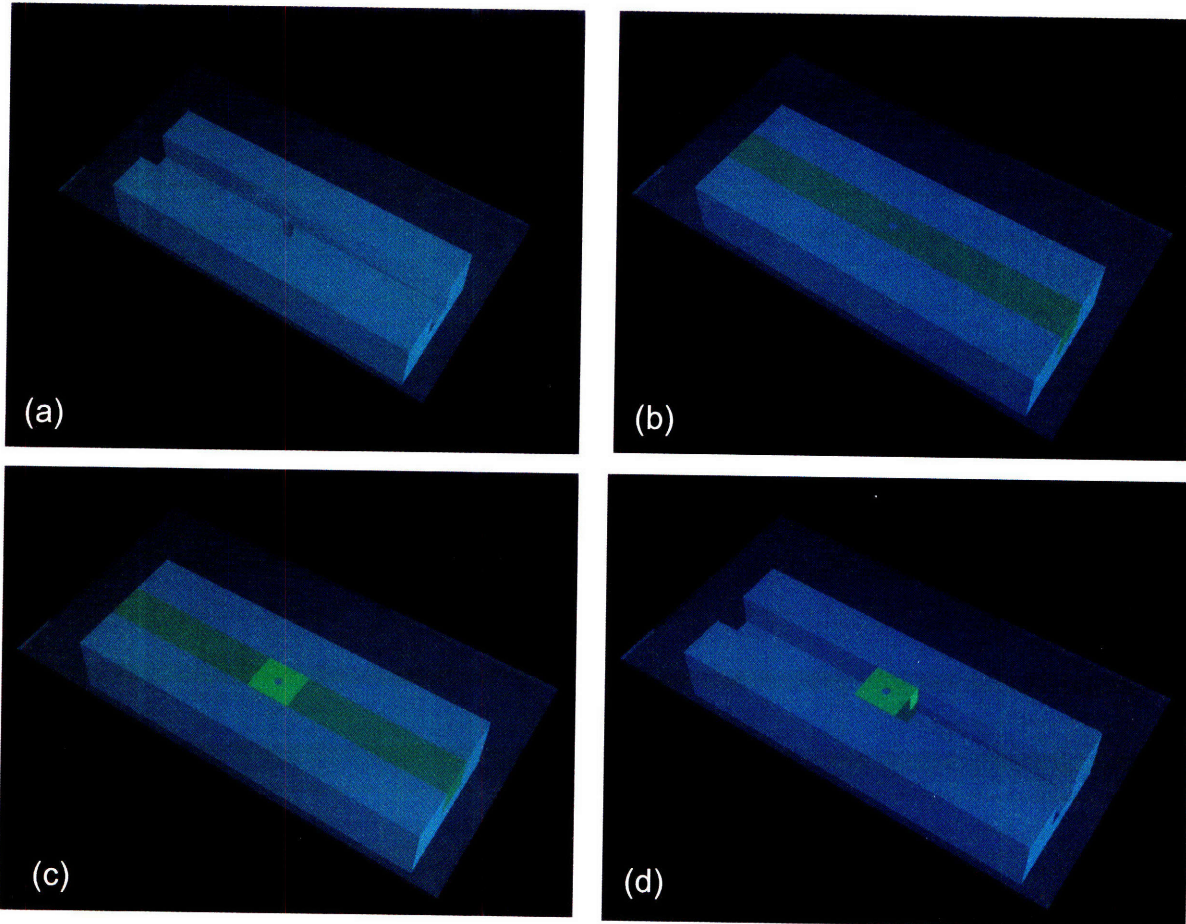


Fig. 3.1 – Stages of fabrication of original design: (a) create PDMS channel with glass top; (b) fill channel with prepolymer solution; (c) photopolymerize plug around post; (d) wash out prepolymer solution

This design originally seemed to satisfy all three of the functional requirements. It utilized the heating of poly(NIPAAm) to actuate the valves. It used photopolymerization to pattern the valves all at once. Finally, a heating element could be patterned onto the glass substrate to allow addressable electronic control of each individual valve.

Unfortunately, however, the fabricated valves did not behave as originally intended. The specific details of this fabrication process are discussed in more depth in Section 5.1. Figure 3.2 shows a typical valve fabricated by this process prior to and after the application of heat. From Fig. 3.2(a), it is clear that FR_1 cannot be satisfied. This is

because the poly(NIPAAm) does not entirely block the flow when in its swollen state. As was discussed in Section 2.6, oxygen inhibition prevents polymerization up to the edges of the channel [84]. Confirmation of this result is discussed further in Section 6.1. Overall, it was clear that this simple design would not be effective. Additionally, it was evident that increased levels of design decomposition within the Axiomatic Design framework were necessary.

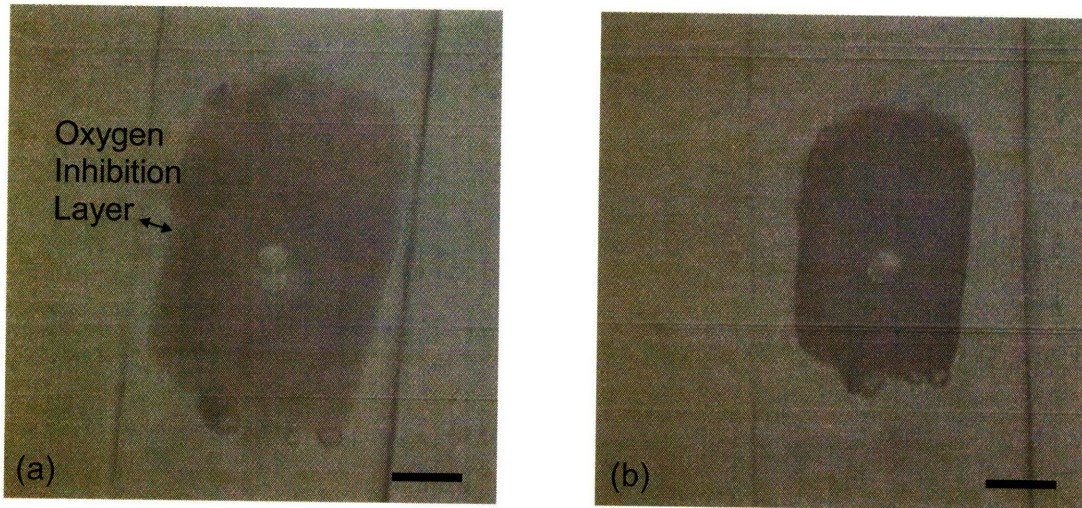


Fig. 3.2 – poly(NIPAAm) valves created by photopatterning in PDMS channels: (a) Prior to heating; (b) After heating. Oxygen inhibition prevents polymerization near the channel edges that scales with the characteristic diffusion length of the oxygen molecules. Polymerization was carried out as a 10sec continuous exposure on a Karl Suss MJB3 mask aligner. Scale bar is 50 μm .

3.4 Further Decomposition and Intermediate Designs

Due to the clear shortcomings in the original design, the functional requirements and design parameters were reconsidered and further decomposed. Decomposition in axiomatic design refers to defining lower level FRs for the DPs already specified.

3.4.1 Redefining DP_3

Prior to further decomposition, DP_3 was changed as to prevent issues with photopolymerization and improve results. Instead of using photolithography to pattern valves, the valves should be arrayed on a separate substrate to allow for scalability. This

allows for not only rapid fabrication of the valves, but also the ability to use a variety of channel designs with one valve substrate. Using a template, chip designers could design a variety of patterns by assuring that they cross certain locations on the template substrate wherever they want a valve. This greatly increases the scalability as valve substrates could be mass produced for use many different types of microfluidic devices.

3.4.2 Second Level of Decomposition

In order to improve the valve design, it was essential to decompose FR_1 further. DP_1 was defined as using the heating and shrinking of poly(NIPAAm) to open valves. This was decomposed into four new FRs:

- $FR_{1,1}$ – Valve must fully block the entire area of the channel
- $FR_{1,2}$ – Minimize the pressure drop across the open channel
- $FR_{1,3}$ – Minimize the time to open the valve
- $FR_{1,4}$ – Minimize the change in temperature of the working fluid

The first FR was chosen in order to avoid the problem with the original valve design. $FR_{1,2}$ was chosen because it is ideal in some situations to require as small of a pressure source as possible. Additionally, large pressure drops can add up quickly if a device is complex and contains a lot of valves. The choice of $FR_{1,3}$ is somewhat dependent on the application in that some applications (e.g. *in vivo* drug delivery) do not require extremely fast response time for the valves. Nonetheless, there are many devices where timing benefits are the main benefit of the device (e.g. on-chip polymerase chain reaction) and should not be limited by the valves. Finally, $FR_{1,4}$ was chosen because there are many chips where heat transfer can play a large part in the functionality of the device (e.g. PCR, cell culture, biomolecule folding). If the heat used to actuate the valve results in changes in temperature of the working fluid, this could significantly detract from the variety of applications with which these valves could be used. Temperature dependence is extremely important at the microscale, and can be seen in molecular mechanics models such as the wormlike chain model where the persistence length scales as $(k_B T)^{-1}$ or in statistical mechanics models such as the canonical ensemble where the probability of any state and the overall partition function both scale as $\exp(1/k_B T)$ [91-93].

To address these FRs, the following DPs were chosen:

- $DP_{1.1}$ – Utilize designs that do not require NIPAAm to span the entire width of the channel
- $DP_{1.2}$ – Increase the height around the valve
- $DP_{1.3}$ – Maximize the swelling ratio of the hydrogel
- $DP_{1.4}$ – Decrease the size of the valve
- $DP_{1.5}$ – Use magnetic nanoparticles to generate heat from inside the gel

Thus, the second order system matrix is as follows:

$$[A]_2 = \begin{bmatrix} X & 0 & 0 & 0 & 0 \\ 0 & X & X & X & 0 \\ 0 & X & 0 & X & 0 \\ 0 & 0 & 0 & X & X \end{bmatrix} \quad (3.7)$$

Immediately, it is evident from inspection that the design is redundant because the matrix is not square. This is due to the fact that $DP_{1.2}$ and $DP_{1.3}$ are both addressing $FR_{1.2}$. From Section 2.1.1, it is known that the pressure drop for Poiseuille flow scales as h^{-3} where h is the height of the channel. Thus, the pressure drop can be minimized by maximizing the shortest dimension through which the flow travels when passing through the open valve. This is done by ensuring that the gel shrinks as much as possible ($DP_{1.3}$), and by maximizing the height of the open valve ($DP_{1.2}$).

While the redundancy of this design may seem like a problem, the solution is simple. Rather than allowing $DP_{1.3}$ to vary it should be made a constant. This constant is the maximum swelling ratio achievable that does not result in an unacceptable hydraulic permeability (since hydraulic permeability and swelling ratio both increase with decreased cross-linking ratio – Sections 2.1.4 and 2.1.5). This makes intuitive sense since there is no reason why one would wish to reduce the swelling ratio to anything less than the maximum allowed. Thus, the system matrix reduces to the following form:

$$[A]_2 = \begin{bmatrix} X & 0 & 0 & 0 \\ 0 & X & X & 0 \\ 0 & X & X & 0 \\ 0 & 0 & X & X \end{bmatrix} \quad (3.8)$$

The system matrix is no longer redundant; however, it is still coupled since the matrix is not triangular. This is because $DP_{1,2}$ and $DP_{1,3}$ (previously $DP_{1,4}$) both affect $FR_{1,2}$ and $FR_{1,3}$. The problem lies in the fact that the smaller size of the gel is required to reduce the time to open the valve. This is because the swelling kinetics are governed by diffusion of the water molecules, and thus the characteristic time constant scales as $\tau \sim L^2/D$ (Section 2.4). Alternatively, as previously mentioned, the pressure drop scales with h^{-3} . To address this problem, one can alter $DP_{1,3}$. By changing it such that the height can remain constant but that multiple gels are used, the in-plane diffusion length is decreased while the height is maintained. In short, $DP_{1,3}$ can be restated as “use multiple gels.”

The system matrix now reduces to the following form:

$$[A]_2 = \begin{bmatrix} X & 0 & 0 & 0 \\ 0 & X & 0 & 0 \\ 0 & X & X & 0 \\ 0 & 0 & X & X \end{bmatrix} \quad (3.9)$$

As one can see, the matrix is now triangular, and thus the design is decoupled. This system matrix now informs the designer of the proper order in which to tune the design parameters to reach the desired functional requirements.

3.4.3 Third Level of Decomposition

In order to realize a fully developed design, the DPs were decomposed further. Thus the following FRs were derived from the second level DPs:

- $FR_{1,1,1}$ – Valve must entirely block without spanning the width of the channel

- $FR_{1.5.1}$ – The magnetic field strength should be approximately 2.5 kA/m [64]
- $FR_{1.5.2}$ – The current density should not exceed the maximum current density of the film of approximately 10^5 A/mm²
- $FR_{1.5.3}$ – Joule heating in coil should not exceed the melting temperature of the film, which for gold is 1064.2°C
- $FR_{1.5.4}$ – wt% of nanoparticles should not affect swelling ratio or the ability to polymerize the gel

The use of magnetic nanoparticles requires an oscillating magnetic field to generate heat within the gels. In order to do this in a reasonable amount of time, it has been shown that magnetic field strengths of approximately 2.5 kA/m are required [64]. Furthermore, when passing current through films it is essential that the current neither exceeds the maximum current density of the film nor results in so much Joule heating that the film melts. Finally, it is important to ensure that the nanoparticles are not in such a high concentration as to limit the ability of the gel to swell or to be patterned by means of photolithography.

The design parameters chosen to address these functional requirements are as follows:

- $DP_{1.1.1}$ – Hydrogel blocks should cover holes instead of channel area
- $DP_{1.5.1}$ – Use a planar MEMS magnetic coil with sufficient current
- $DP_{1.5.2}$ – Maximize the cross-sectional area of the magnetic coil
- $DP_{1.5.3}$ – Use a low enough current that that the resistive heating does not exceed the maximum allowed
- $DP_{1.5.4}$ – Minimize wt% of nanoparticles that will generate sufficient heat

The resulting system matrix for the chosen DPs and FRs is shown below:

$$[A]_3 = \begin{bmatrix} X & 0 & 0 & 0 & 0 \\ 0 & X & 0 & X & 0 \\ 0 & X & X & X & 0 \\ 0 & X & X & X & 0 \\ 0 & 0 & 0 & 0 & X \end{bmatrix} \quad (3.10)$$

Clearly, this matrix highly coupled. Subsequent design and optimization of this matrix is discussed in the following sections.

3.4.4 Intermediate Valve Designs and Reformulation of $DP_{1,1}$

While the third level system matrix is highly coupled, the valve portion is completely uncoupled from the magnetic coil. This allows for the design of valve structures without being concerned about the coupling regarding the magnetic coil. The key to these designs was that the poly(NIPAAm) gels would cover holes in the channel rather than spanning the entire width of the channels. The general principle behind this is shown in Figure 3.3.

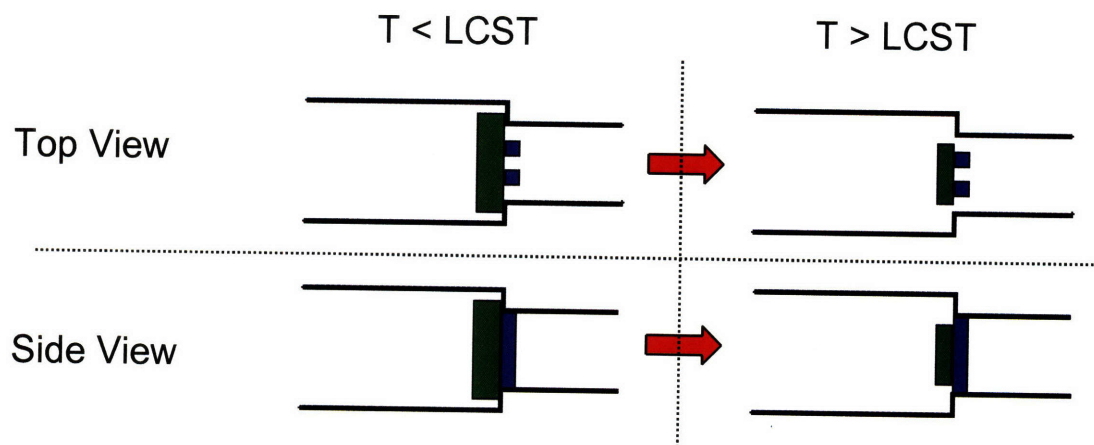


Fig. 3.3 – Schematic of valve principle. Contractions in channel widths and heights allow for the gels to completely cover the channel without requiring polymerization to the walls. Green represent the poly(NIPAAm) and blue represents posts within the channel. The posts are necessary for preventing the shrunken poly(NIPAAm) blocks from moving downstream.

A variety of different valve designs were created based upon this principle. Figure 3.4 shows two sample designs.

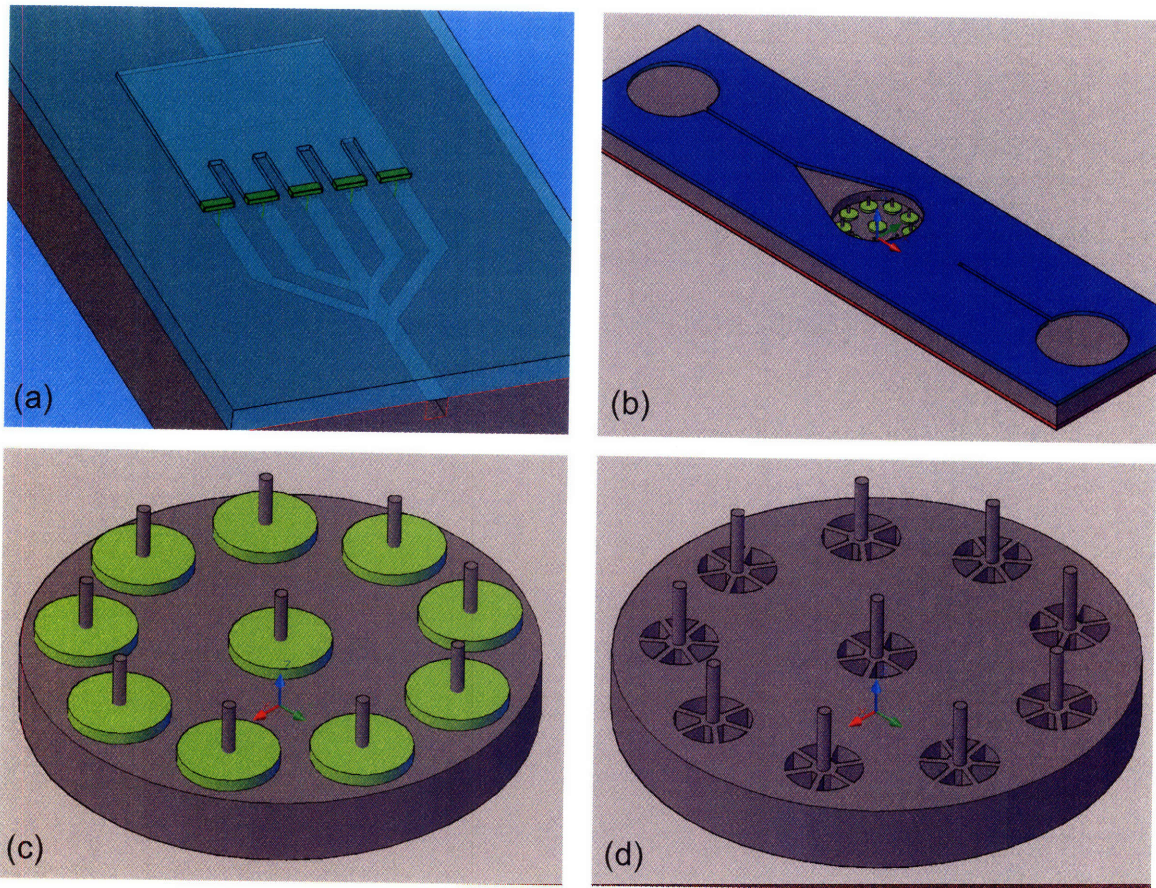


Fig. 3.4 – Various valve design that satisfy $DP_{1.1.1}$: (a) poly(NIPAAm) blocks (green) block channels with smaller widths and heights than the channel sections containing the gels; (b), (c), (d) poly(NIPAAm) disks cover vertical holes. Posts are used to hold the disks in place and in-plane crossing features prevent the shrunken gels from passing through. Flow through these valves is vertical.

While these designs all met the design parameters specified from the axiomatic approach, it was clear that the second axiom was not being well adhered to. The second axiom states that the best design is the one with the minimum information content, where the information content is related to the probability of success of a given design. Because the complexity of all of these designs is high, the information content is also high. The main problem arises in the fabrication of these devices. Most of them require significant amounts of micromachining and precise control of the polymerization of the NIPAAm. With additional masks and processing steps the probability of success decreases. Additionally, the valves would be so much more difficult to fabricate than convention valves made with soft lithography that their benefits may be outweighed by the complexity.

To address this issue, it was apparent that one could alter $DP_{1.1}$. While the DP stated that the hydrogel could not span the width of the channel and fully block it, that statement is not entirely true. The source of the lack of polymerization at the edges was the presence of molecular oxygen that had permeated through the PDMS. It is, however, possible to use other substrates than PDMS and avoid this problem entirely. For example, glass is not as permeable to oxygen as PDMS and thus could be used as a channel or valve substrate with which NIPAAm could be polymerized to the edges. Therefore, $DP_{1.1}$ was changed to “Use a glass or silicon substrate.”

3.4.5 Decoupling the Magnetic Field FRs and DPs

Equation 3.10 shows that the third level system matrix is highly coupled. This is mainly due to the fact that two of the DPs are directly contradictory. $DP_{1.5.1}$ states that the current should be maximized in order to generate enough field strength from a planar MEMS magnetic coil, whereas $DP_{1.5.3}$ states the current should be minimized as to ensure that the Joule heating of the coil is minimized.

It is also important to note that while $DP_{1.5.2}$ and $DP_{1.5.3}$ both affect $FR_{1.5.2}$, they do so in a complementary way. Maximizing the cross-sectional area and decreasing the current both act to decrease the current density. It can be seen that the current density requirement is acting not as a FR, but rather as a constraint. Thus, one should set the current density limit of approximately 10^5 A/mm² as a constraint. The associated design parameter of maximum cross-sectional area should be held as a constant. There is no reason not to maximize this value, so it should be chosen to be the maximum thickness that can be achieved with the micromachining processes. While one could use electroplating to deposit the coil, this is undesirable as the solution chemistry is difficult to perfect, and the resultant profile is a rough and non-uniform. Thus, the complexity is increased using electroplating and evaporation or sputtering should be used instead. These processes tend to have a maximum thickness of approximately one to two microns depending on deposition materials and conditions.

In order to reduce the coupling, one should reexamine the equation for the magnetic field strength (Eq. 2.138) derived in Section 2.2.2:

$$H = I \left\{ \frac{N}{R} \left[\ln(N) + 0.5 \ln \left(\left(\frac{R}{Nd} \right)^2 \right) + \ln \left(1 + \sqrt{1 + \left(\frac{d}{R} \right)^2} \right) \right] - \frac{N}{R \sqrt{1 + \left(\frac{d}{R} \right)^2}} \right\} \quad (3.11)$$

From inspection of this equation, it is clear that the magnetic field strength can be altered by other mechanisms than the current as well. By altering either the number of turns, N , or the radius of the magnetic coil, R , one can change the magnetic field without altering the current. Unfortunately, these terms do not affect the field linearly and thus make tuning it much more difficult, which in turn increases the information content.

As was discussed in Section 2.2.2, the coil parameters were set such that the width of the coil in plane would be equivalent to the in-plane spacing between adjacent rings. From this, one can state the cross sectional area in terms of the other parameters as:

$$\alpha = hw_c = h \frac{R}{2N} \quad (3.12)$$

Here, h is the out-of-plane thickness of the coil. Since the cross sectional area should remain maximized at a constant value, one can alter the field strength, H , by increasing R and N simultaneously such that their ratio remains constant. Figure 3.5 shows the dependence of H on increasing values of N when R/N is maintained constant.

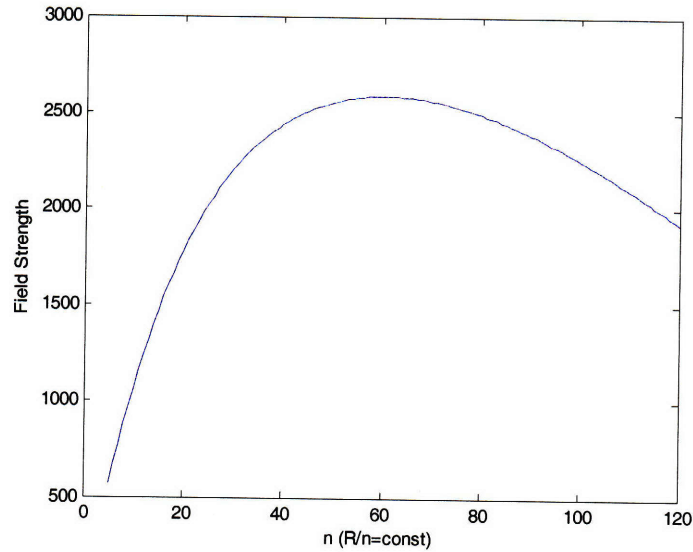


Fig. 3.5 – Dependence of magnetic field strength on increasing N and R for a constant value of $R/N = 10\mu\text{m}/\text{turn}$. Location of the peak is dependent upon d (distance from gel to coil).

Thus, $DP_{1.5.1}$ can be altered to say “maximize coil radius and number of coils while maintaining their quotient to be constant.” This maximizing obviously has limits that are derived both from fabrication limitations and practical limitations such as the fact that very large diameter coils cannot be useful on microscale chips. Additionally, the relationship expressed in Eq. 3.11 and displayed in Fig. 3.5 suggests that there is a point at which the field strength will begin decrease. This point (provided that it is not outside of the range of fabrication compatibilities) should be chosen.

Ultimately, the design is decoupled. The constraint regarding the current density sets the out-of plane thickness (due to fabrication limitations) and the minimum width below which the current exceeds the constraint. The Joule heating FR is controlled next by altering the current such that it is below the heating limitations. Finally, the magnetic field strength is achieved by increasing the radius and number of coils.

The resulting system matrix for this level is:

$$[A]_B = \begin{bmatrix} X & 0 & 0 & 0 \\ 0 & X & X & 0 \\ 0 & 0 & X & 0 \\ 0 & 0 & 0 & X \end{bmatrix} \quad (3.13)$$

Of course, this is only decoupled to first order since the Joule heating not only increases with decreased cross-sectional area, but also with increased length. The length of the coil is obviously increasing as the coil radius increases. However, if it is necessary to include this factor, an iterative process can be used where the new length value derived from increasing the coil radius is inserted back into the resistive heating equation to determine a new, lower, current value. This in turn yields a higher radius, and this process can be repeated until a solution is converged upon.

If in-plane size is a limiting factor and coil radius cannot be increased, one can approach the decoupling in a different way. Rather than using a single planar magnetic coil, one could “stack” planar coils on top of each other. This would also more closely represent what is done at the macro-scale where solenoids and inductors are inherently out-of-plane structures. This stacking would take the place of $DP_{1.5.1}$ again in that instead of increasing current or radius and number of turns, one could stack multiple planar coils. This would allow for low currents to still be used to generate the necessary field strength.

Unfortunately, such structures are much more difficult to realize using microfabrication. Insulator layers with connecting electrodes must be patterned and would greatly increase the information content of the device.

3.4.6 Manufacturing FRs and DPs

It is important to consider the possible functional requirements of the fabrication processes themselves before completely settling upon a design. In true Axiomatic Design, this would take the form of mapping to the physical domain and would utilize process variables (PVs). For the purpose of this design, such a level of analysis was not necessary and thus these parameters are represented as FRs and DPs.

The first thing to consider is whether or not it is useful to have a transparent substrate. Many microfluidic devices utilize transparent substrates in order to see the samples using conventional fluorescence microscopes, laser excitation, and other biological imaging tools that rely upon sample transparency. Because of this demand, it is useful to specify the design parameter of using a clear substrate.

Secondly, it is important to minimize the complexity of channel fabrication. To do this, one should use conventional fabrication techniques in microfluidics such as soft lithography. This process uses PDMS to make the channels, and is available to virtually any lab working in the field. Thus, the channels should be a separate substrate from the valves. This also aids in assembly since the components of the valves are physically uncoupled. Additionally, it assists in meeting the constraint of large scale integration.

3.5 Complexity and Predictable Shrinking

After following the previously discussed process of decomposition, the design has been successfully decoupled. There is, however, a large degree of imaginary complexity due to the uncertainty regarding the position of the shrunken gel. From the decomposition, it was determined the valve should be made out of poly(NIPAAm) on a separate substrate from the channels (Fig. 3.6(a)), and that the shrinking of the hydrogel would allow flow through the valve. The problem arises in that the shrinking occurs in an unpredictable manner (Fig. 3.6(b) and (c)).

The complexity derived from this design is known as “Imaginary Complexity” in Axiomatic Design because the position of the shrunken gel cannot be known. This uncertainty leads to problems in that the flow profile and fluidic resistance will change depending on the position. In order to address this concern, one should add the FR that “the shrinking must be predictable.” The associated DP is that “the gel should be confined upon its bottom surface using anchor structures.” These anchor structures are

essential for the consistent functionality of these valves. Thus the final FRs and DPs are chosen to decouple the design and minimize the information content and complexity.

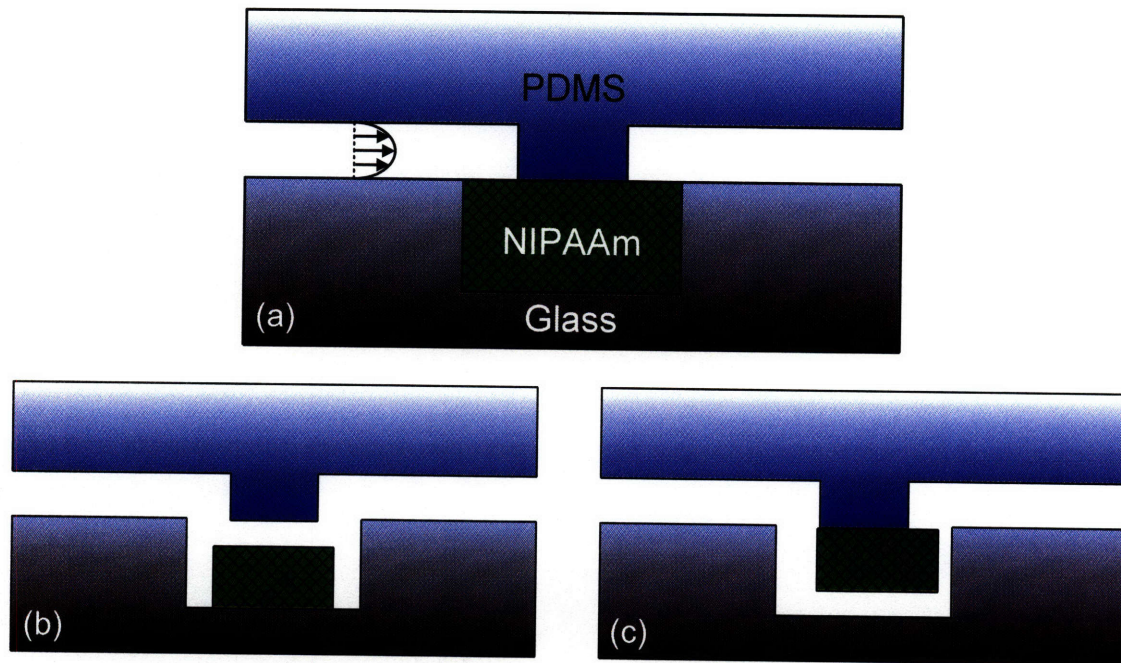


Fig. 3.6 – Unpredictability of position of shrunken gel (a) Valve structure prior to shrinking. The direction of flow is shown as the Poiseuille flow profile; (b) and (c) heating and resulting shrinking of the gel could result in various locations of the gel.

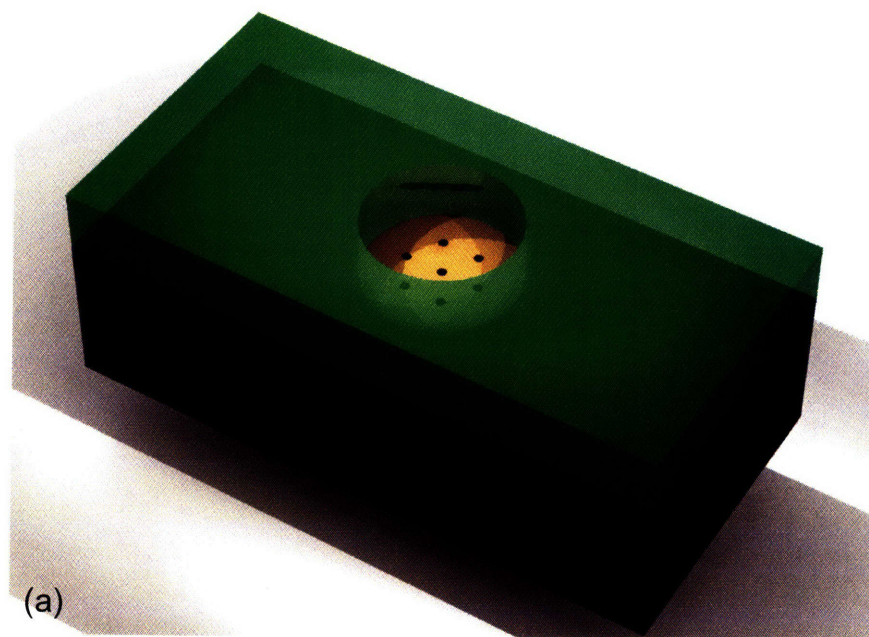
3.6 Final Design

A design for the valve that is composed of all of the DPs was created (Fig. 3.7 and 3.8). It consists of microwells fabricated in a non-PDMS substrate (in accordance with $DP_{1.1}$). Glass was chosen as the substrate due to its optical transparency (as was discussed in Section 3.4.6). At the bottom of the wells, anchor structures were designed to ensure predictable shrinking. The anchors are created by isotropic etching of the glass beneath a metal hard mask. The overhanging metal that results from the undercut of the etch acts to keep the poly(NIPAAm) plug attached to the bottom of the well. Full details and results of the fabrication process are discussed in Chapter 5.

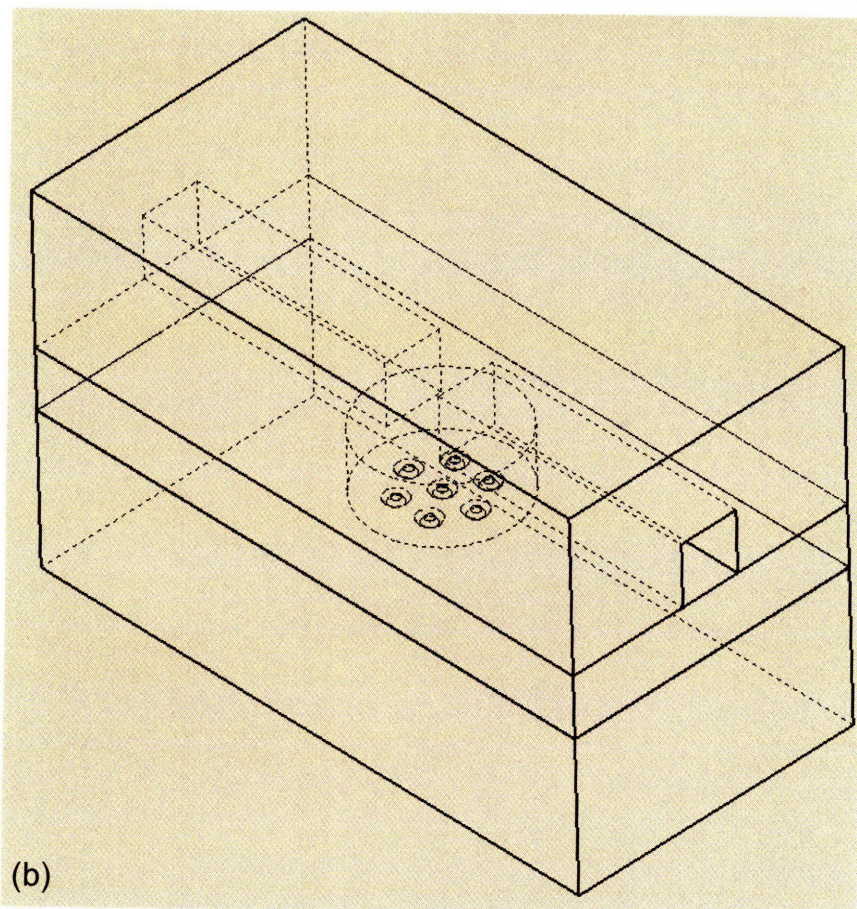
The principle of operation is that when the poly(NIPAAm) is in its swollen state, fluid cannot flow. This is due to a discontinuity in the PDMS channel at the location of the

valve. When the poly(NIPAAm) is heated by application of an oscillating magnetic field, it shrinks downward and allows fluid to flow below the discontinuity (Fig. 3.8(b)). The magnetic field is generated by sending current through the magnetic coil, which is patterned on the back side of the glass substrate.

The pressure drop across the valve is minimized by maximizing the height of the open channel ($DP_{1,2}$). This is done by increasing the depth of the microwell. Since poly(NIPAAm) shrinks isotropically, increasing the depth of the well increases the gap between the PDMS and the hydrogel surface. Additionally, the well can be made with a diameter that is larger than the channel width to further decrease the fluidic resistance of the valve. The resistance as a function of the in-plane dimension scales only as linear dependence rather than a third power one as it does with the height.



(a)



(b)

Fig. 3.7 – 3D views of valve design: (a) Prior to filling well with poly(NIPAAm) and bonding the PDMS channel; (b) Beneath the metal hard mask are the anchor holes. Discontinuities in the channels allow the valve to be closed when swollen.

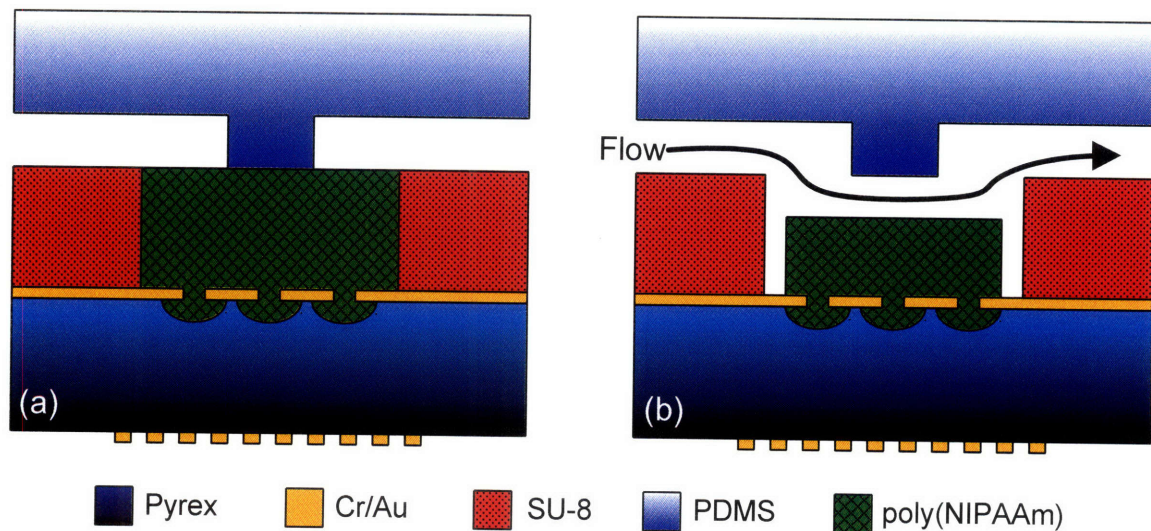


Fig. 3.8 – Cross-sectional view of valve operation: (a) Swollen poly(NIPAAm) prevents fluid flow; (b) Heating via the magnetic coil results in poly(NIPAAm) shrinking and subsequent fluid flow.

Time response of the valve can be decreased by using multiple valves in parallel as was described in $DP_{1.3}$. This can be achieved by splitting the channel upstream so that flow is directed across multiple smaller valves at once thus maintaining the pressure drop, but reducing the response time.

4. Device Modeling

4.1 Oxygen Inhibition

A great deal has been discussed in the previous chapters regarding the effects of oxygen inhibiting the free radical polymerization of the NIPAAm prepolymer. Section 2.6 described the distance away from the channel walls to which the oxygen prevented the polymerization as the oxygen penetration length, L_p . This length scales in accordance to the diffusivity and first-order reaction rate constant as:

$$L_p \sim \sqrt{\frac{D}{k}} \quad (4.1)$$

where D is the diffusion coefficient of molecular oxygen in the prepolymer solution, and k is the first-order reaction rate constant. To approximate this length one can use the value for D of oxygen in water, which is $2.10 \times 10^{-5} \text{ cm}^2/\text{s}$ [27]. An approximate value for k can be found in the literature to be 10^3 s^{-1} [84]. Thus, the penetration length should be on the order of microns.

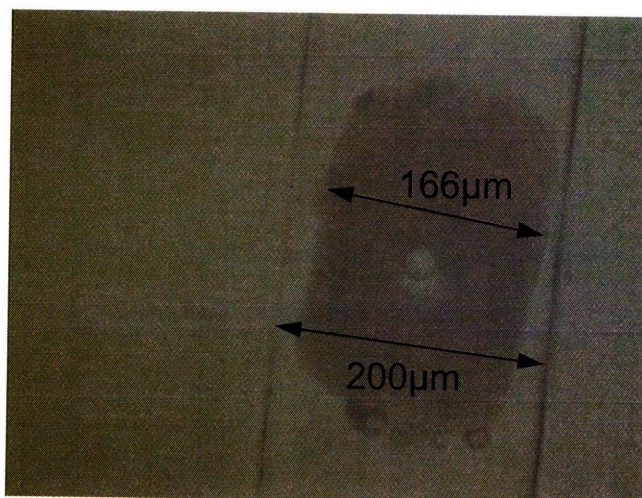


Fig. 4.1 – Measurement of the oxygen inhibition layer suggests a penetration length of approximately $17 \mu\text{m}$.

Fig. 4.1 shows a typical valve after polymerization. Optical measurements suggest that the distance between the channel walls and the gel is $\sim 15\mu\text{m}$. This is on the same order as the calculated penetration length suggesting that oxygen inhibition is the primary reason for the lack of polymerization near the sidewalls.

4.2 Fluid Flow

4.2.1 Analytical Solutions

In Section 3.4.2, $FR_{1,2}$ stated that one should minimize the pressure drop across the open valve. Ideally, this pressure drop would be no greater than the pressure drop across an the same length of open channel. In channels whose width and height are on the same order the pressure drop, ΔP , can be approximated as [79]:

$$\Delta P = Q \frac{12\mu L}{wh^3} \left[1 - \frac{h}{w} \left(\frac{192}{\pi^5} \sum_{n=1,3,5}^{\infty} \frac{1}{n^5} \tanh\left(\frac{n\pi w}{2h}\right) \right) \right]^{-1} \quad (4.2)$$

Plugging in the following design parameters:

$$Q = 10^{-11} \text{ m}^3/\text{s} \text{ (volume flow rate)}$$

$$\mu = 8.9 \times 10^{-4} \text{ Pa}\cdot\text{s} \text{ (dynamic viscosity of water)}$$

$$L = 200\mu\text{m} \text{ (length)}$$

$$w = 100\mu\text{m} \text{ (width of channel)}$$

$$h = 100\mu\text{m} \text{ (height of channel)}$$

The volume flow rate was decided based upon a common microfluidic velocity of 1mm/s. Thus, $\Delta P = 0.507 \text{ Pa}$.

Fabrication limitations limit the depth of the well; however, it is still useful to have an estimate for the pressure drop across the open valve. Because the shrunken gel will leave a gap that is wider than it is tall, the pressure drop expression derived for one-dimensional flow may be applicable. In reality, the flow is three-dimensional and analytical expression for the pressure drop cannot be obtained. Nonetheless, the one-dimensional expression gives an approximation that is useful for determining the height of the well. Setting the pressure drop equal to 0.507 Pa results in

$$\Delta P = Q \frac{12\mu L}{wh^3} \Rightarrow 0.507 = (10^{-11}) \frac{12(8.9 \times 10^{-4})(250 \times 10^{-6})}{(100 \times 10^{-6})h^3} \Rightarrow h = 81 \mu\text{m} \quad (4.3)$$

If thirty percent shrinkage is presumed, this height requires a well that is on the order of 242 μm deep. Of course the flow is not one-dimensional, and the actual pressure drop will be higher. Since the wells are made out of SU-8 (this is discussed in much more detail in the following chapters), a maximum height of 100 μm is used. Substituting 33 μm (30% of 100 μm) into Eq. 4.2 yields a pressure drop of 7.4 Pa, which is not as good as if there were no valve there at all, but still very acceptable.

4.2.2 CFD Solutions

The modeling presented in the previous section is useful for making design decisions. Unfortunately, since they are based upon many simplifications, they do not give exact solutions to the pressures and forces created by the fluid flow. To determine more accurate depictions of the fluid flow, computation fluid dynamics (CFD) simulations were used. These simulations were performed using COSMOS FlowWorks. An inlet velocity of 1mm/s was used and atmospheric pressure was applied as an outlet condition. The geometry used was that of a 100 μm \times 100 μm channel with a 200 μm diameter well. Shrinkage of thirty percent was again assumed. Since the anchor structures hold the gel at the bottom of the well, the gel is placed at the bottom for the CFD. Results of the analysis are shown in Figs. 4.2 and 4.3.

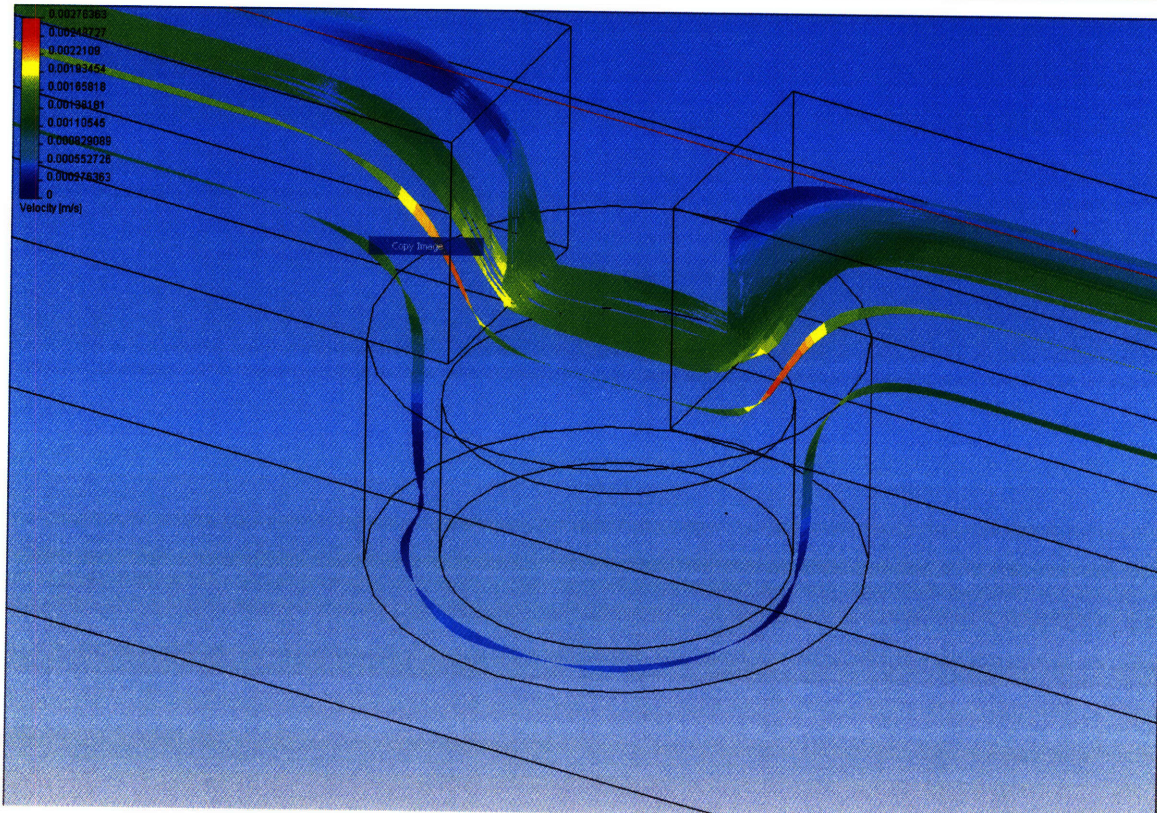
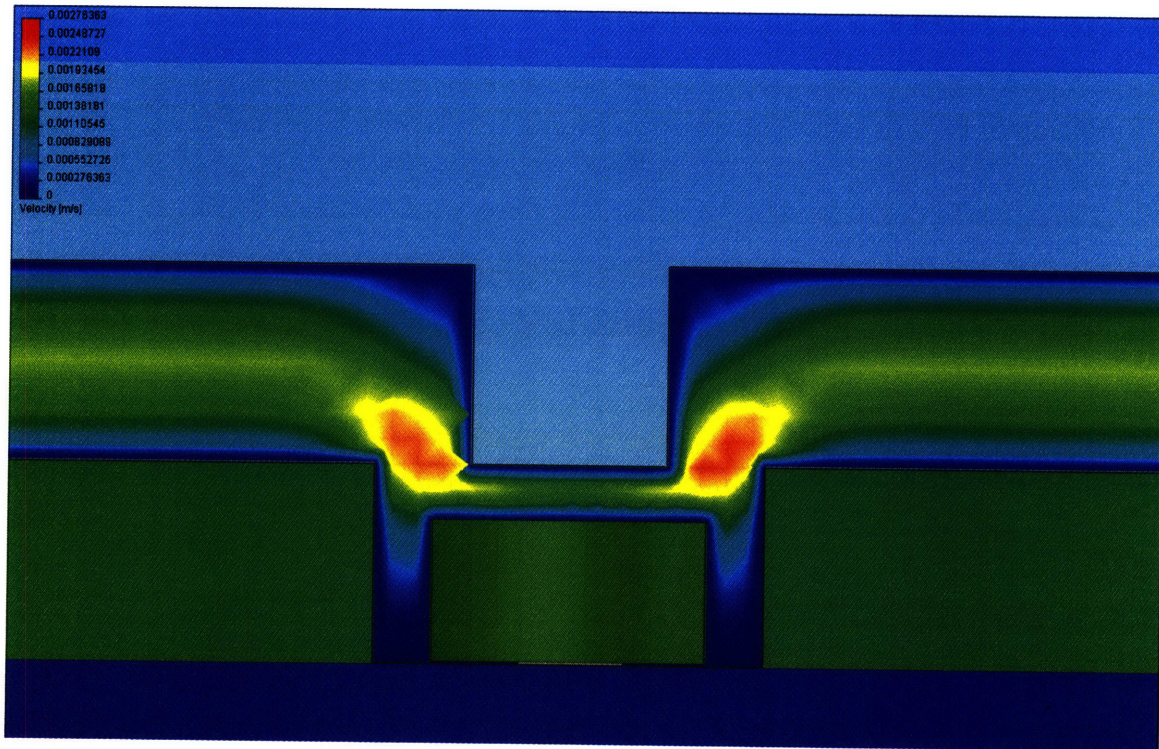


Fig. 4.2 – Velocity distributions around the open valve: (a) profile along central plane of channel; (b) 3D streamlines

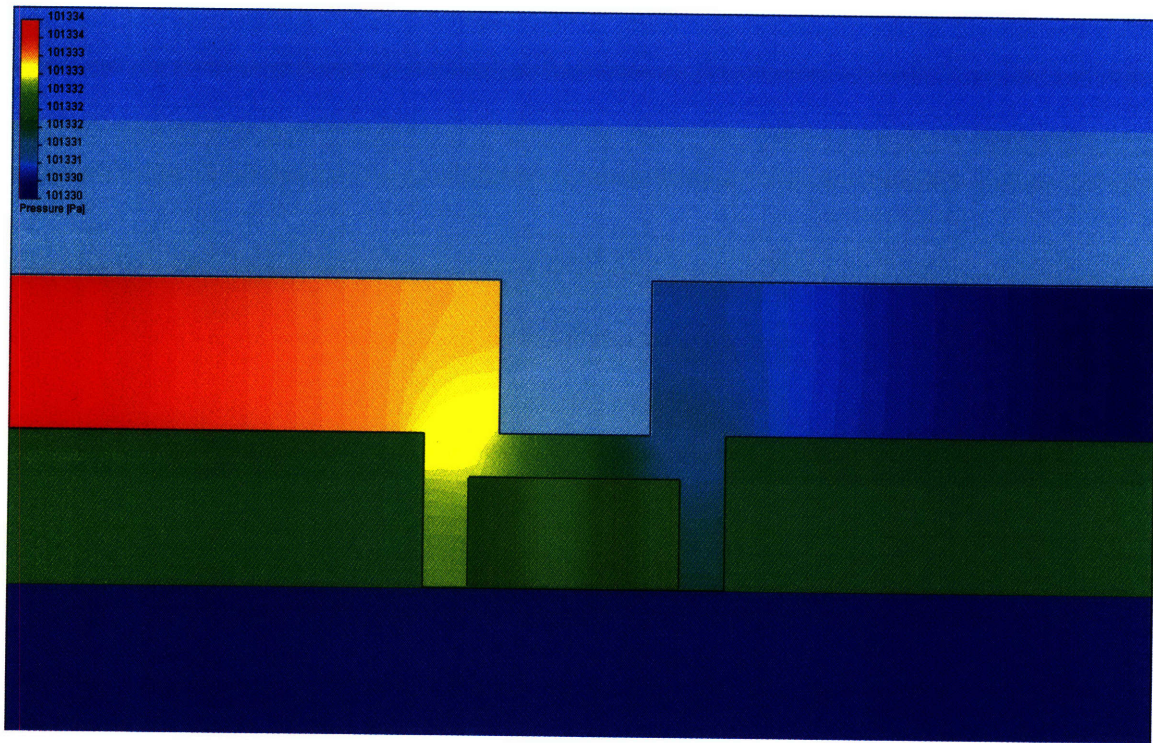


Fig. 4.3 – Total stagnation pressure across the valve displayed with plane along center of channel.

From Fig. 4.3, one can see that the pressure drop across the valve is on the order of 2-4 Pa. This is actually *less* than the pressure drop predicted from the one-dimensional equation. The reason for this is that, due to the isotropic shrinking of the gel, fluid can also flow around the sides of the poly(NIPAAm) plug and thus the flow area is higher. Evidence that this flow occurs can be seen in Fig. 4.2 where the flow clearly has vertical components.

4.2.3 Stresses on the Gel and Anchors

It was also important to determine the stresses imposed on the gel by the fluid flow. Again, CFD modeling with the aforementioned conditions was applied. The results of this simulation are shown in Fig. 4.4. Integrating the pressure distribution and shear forces around the gel results in a negligible upward force of about 90pN and a forward force of about 23.2nN.

These stresses are important to determine if either the gel or the anchor metal could suffer any damage due to the imposed fluid stresses. To investigate the latter concern, one should determine the adhesion strength of the metal to the substrate. Benjamin and Weaver characterized the adhesion strengths of a variety of evaporated metal films on glass substrates [94]. From these findings, it appears that Iron, Chromium, Titanium, and some other less common metals have the best adhesion. For this reason and its ability to be easily wet etched, chromium is chosen as an adhesion layer between the wafer and the gold. The adhesion strength of chromium is greater than 500g (in their own units) which corresponds to a shear stress of $300 \times 10^8 \text{ dyn/cm}^2$ ($30 \times 10^8 \text{ Pa}$). This was the maximum range of their testing setup, and thus the adhesion strength may be much higher than that.

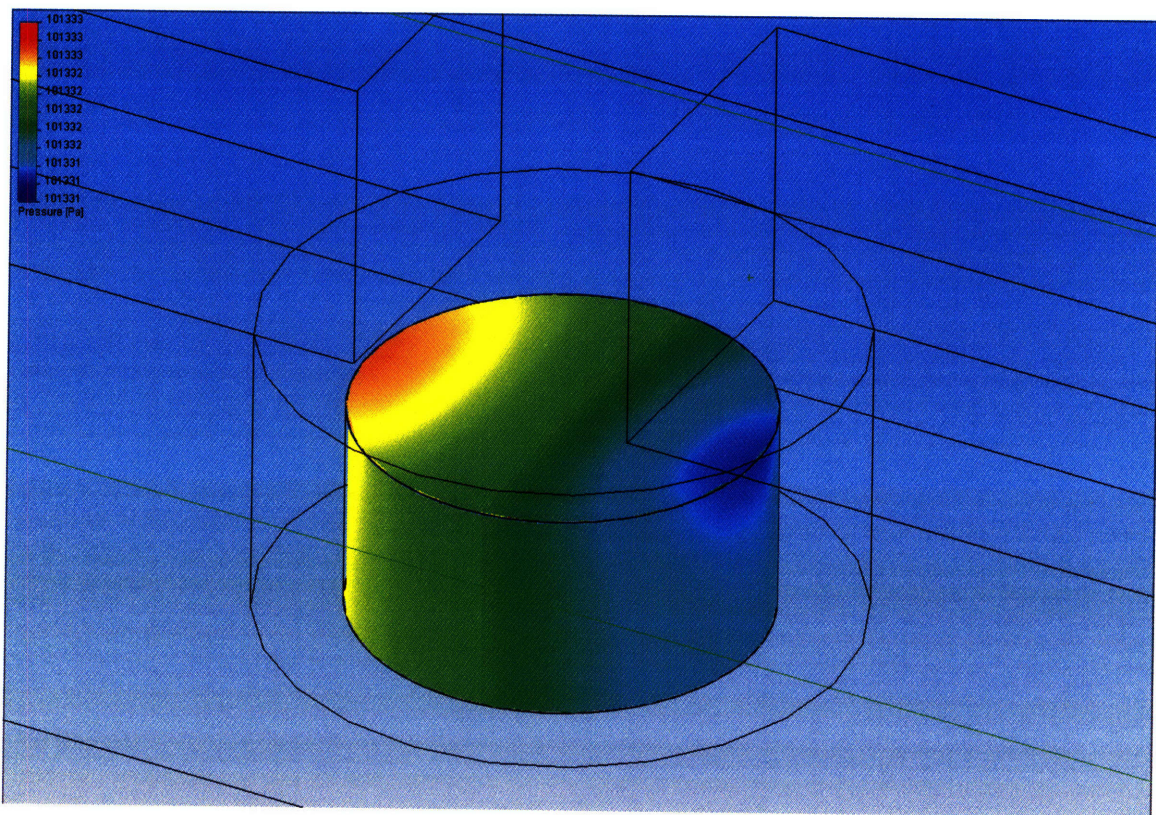


Fig. 4.4 – Pressure distribution across the poly(NIPAAm) plug.

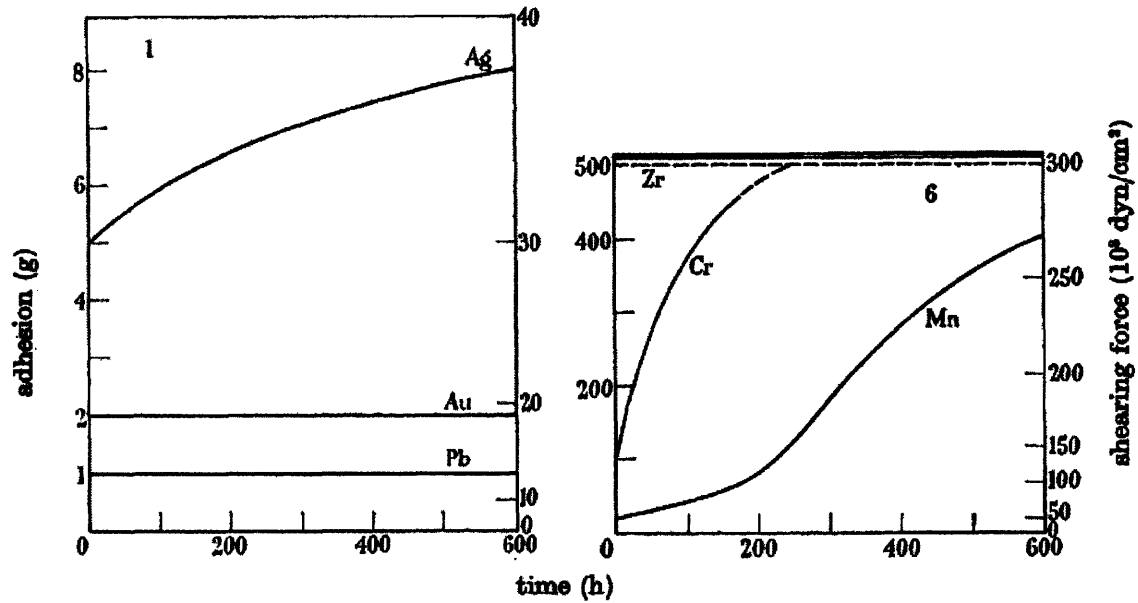


Fig. 4.5 – Adhesion forces of various evaporated metals on glass characterized by Benjamin and Weaver [94].

The fabrication of the anchors is discussed in the next chapter. Depending on the amount of lateral etching the amount of overhang of the metal over the hole varies. To determine if the adhesion strength of the metal and the force applied to it from the gel are on the same order, one can estimate a difference in diameters of the metal hole to the underlying glass hemisphere to be on the order of ten microns. Thus, even if the entirety of the force applied to the gel were transmitted to only one anchor, the adhesion strength would still be about six to seven orders of magnitude stronger than necessary. Additionally, the yield strength of most hydrogels is on the order of kilopascals [63, 95], thus the gel is still two to three orders of magnitude stronger than the stresses applied by the fluid.

It is also important to determine if the stresses applied to the anchors result in any significant deformation of the gold film. This analysis was performed using FEA (COSMOSWorks) and the results are shown in Fig. 4.6. The maximum stresses found in any of the anchor structures is approximately 9kPa, and the maximum displacement of the film 45pm. Thus, the deformation of the films is essentially negligible. Of course, real devices are often less structurally sound than the modeled ones due to defects and residual stresses. While these are not predicted by the model, they were not seen to present any problems in the fabricated devices. If such issues became significant, one could switch the metal layer from Cr-Au to polysilicon. Polysilicon has a higher modulus

of elasticity (hundreds of GPa). Additionally, polysilicon has even better adhesion to glass since it forms covalent bonds between the silicon and oxygen atoms.

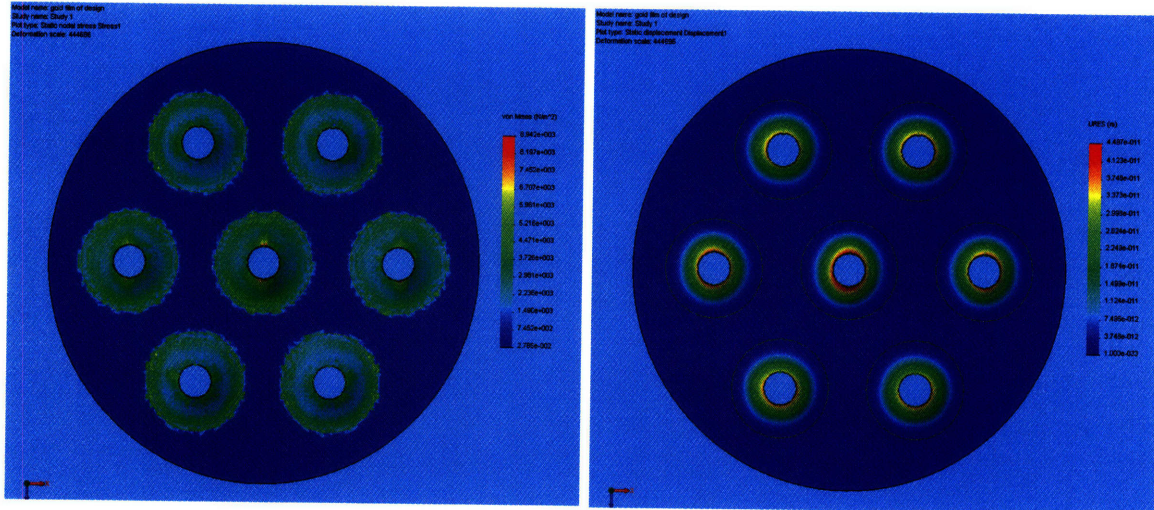


Fig. 4.6 – FEA analysis of the stresses on the gold film: (a) stress; (b) displacement.

4.3 Magnetic Heating

4.3.1 Magnetic Nanoparticles

In order to determine the amount of heating that can be provided using magnetic nanoparticles, one should apply the modeling presented in Section 2.2.1. The power dissipation can be approximated by Eq. 2.117:

$$P = \mu_0 \pi H_0^2 f \chi_0 \frac{2\pi f \tau}{1 + (2\pi f \tau)^2} \quad (4.4)$$

Magnetic heating was demonstrated in hydrogels by Lao *et al.*[64]. They showed that at magnetic field strengths of approximately 2.5 kA/m and frequencies of 375 kHz heating of the hydrogel could be performed rapidly. $\mu_0 = 4\pi \times 10^{-7} \text{ N/A}^2$ and $\chi_0 = 0.56$ (from EMG 705 data sheet – see Appendix 2). The time constant τ was approximated from

Rosensweig *et al.* [70] to be 2×10^{-5} sec. Thus the power dissipation is 3.5×10^{11} W/m³. The hydrogel in the valves has a volume of approximately 5×10^{-12} m³ of which approximately 3% is filled with nanoparticles. This means that the nanoparticle heating generates about 50mW. Using the thermal conductivities and specific heats of water to model the gel, one can show (though it is not done here) that while it takes seconds to reach the equilibrium temperature, the LCST can be reached in milliseconds or less.

4.3.2 MEMS Magnetic Coil

As was described in Section 3.4.5, the design of the magnetic coil is difficult due to the coupling of the various parameters in the design. While the equation to generate the necessary field can be solved using a variety of different parameters, the limitations regarding fabrication, current density, and Joule heating restrict the choices of these parameters. The ultimate goal of the design was to produce a magnetic field strength greater than 2.5kA/m since value this has been shown to produce rapid heating in hydrogels [64].

Following the approach specified in Section 3.4.5, the thickness of the coil is set to its maximum based on fabrication limitations. Since the metal will be deposited by electron beam evaporation, a reasonable maximum that will still avoid unpredictability is about 750nm. The maximum current density of gold is on the order of 10^5 A/mm²; however, in order to ensure some factor of safety, the maximum allowed in this design is 10^4 A/mm². This establishes a relationship between the coil width and current that can be used given the thickness of 750nm. Fabrication limitations also exist for the minimum allowable width due to the resolution of the lithography tools available. This is set to 5 μ m although smaller features are likely achievable.

The current selected is chosen based upon the Joule heating that results. The melting temperature of gold is about 1340K. Again, to ensure a factor of safety, the maximum temperature allowed in the coil was set to 1000K. To model the heat transfer, the lumped element model described in Section 2.5.3 was utilized. All of the available parameters

were put into a MATLAB® (MathWorks) program that determined the field strength and temperature increase. While ideal operating frequencies can be derived from the nanoparticle power dissipation models, it is desirable for the user to be able to adjust the frequencies of the field when tuning the device. The extreme case is that of a step input where the coil is constantly subjected to a maximum current. While this does nothing in the way of heating up the nanoparticles, it is the case of maximum heating of the coil. Using the transfer function specified in Eq. 2.187, the system response was determined for the chosen values. After following through the steps described in Section 3.4.5, the following values were chosen for the magnetic coil:

$t = 750\text{nm} \rightarrow$ thickness of coil

$R = 600\mu\text{m} \rightarrow$ radius of coil

$N = 60 \rightarrow$ number of turns

$d = 150\mu\text{m} \rightarrow$ distance from coil to gel

$I = 23\text{mA} \rightarrow$ current through coil

Due to the defined geometrical relationships of the coil and effects of heating on resistance, the following values result from these choices:

$L_c = 113.1\text{mm} \rightarrow$ length of coil “wire”

$w_c = 5\mu\text{m} \rightarrow$ width of coil “wire”

$R_e = 1351\Omega \rightarrow$ electrical resistance at final temperature (determined using TCR)

$R_{wafer} = 6.35\text{K/W} \rightarrow$ thermal resistance of wafer

$R_{air} = 888.89\text{K/W} \rightarrow$ thermal resistance of air

$C_{wafer} = 5.43\text{J/K} \rightarrow$ thermal capacitance of wafer

In modeling the convective resistance, a value had to be chosen for h . Because this value is not known, it was selected to be $15\text{W/m}^2\text{-K}$, which is in the range for common free convection values. The step response of the system is shown in Fig. 4.7. The maximum temperature change reached is approximately 318K suggesting that the final temperature is approximately $615\text{-}620\text{K}$. This is well below the maximum prescribed.

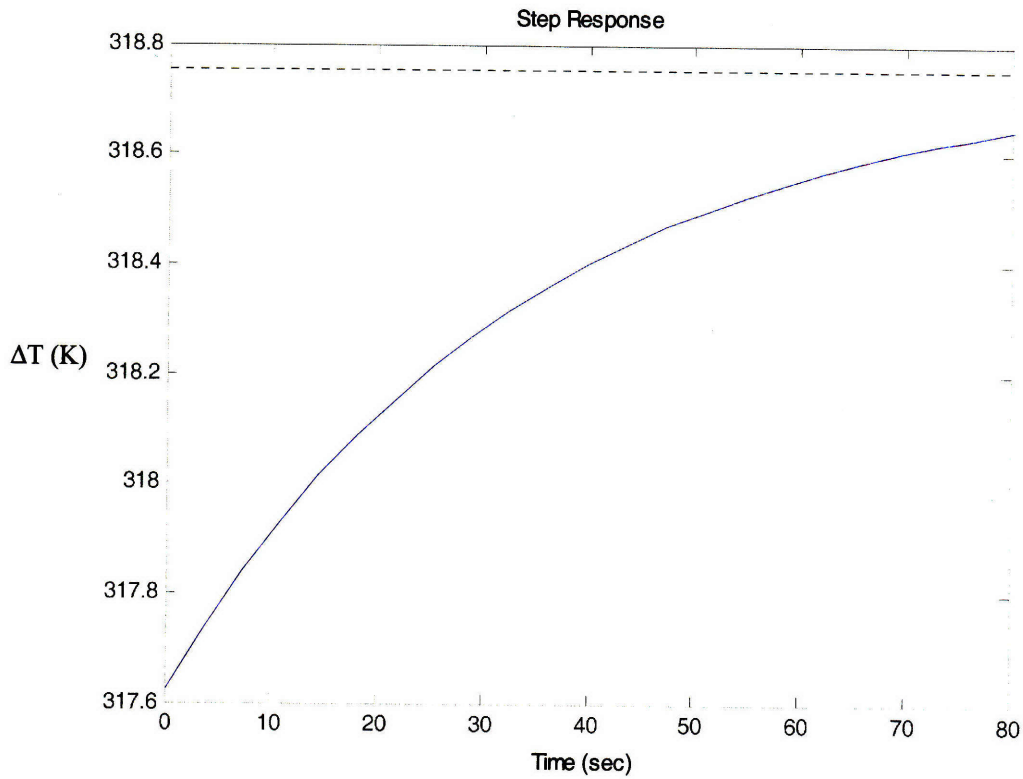
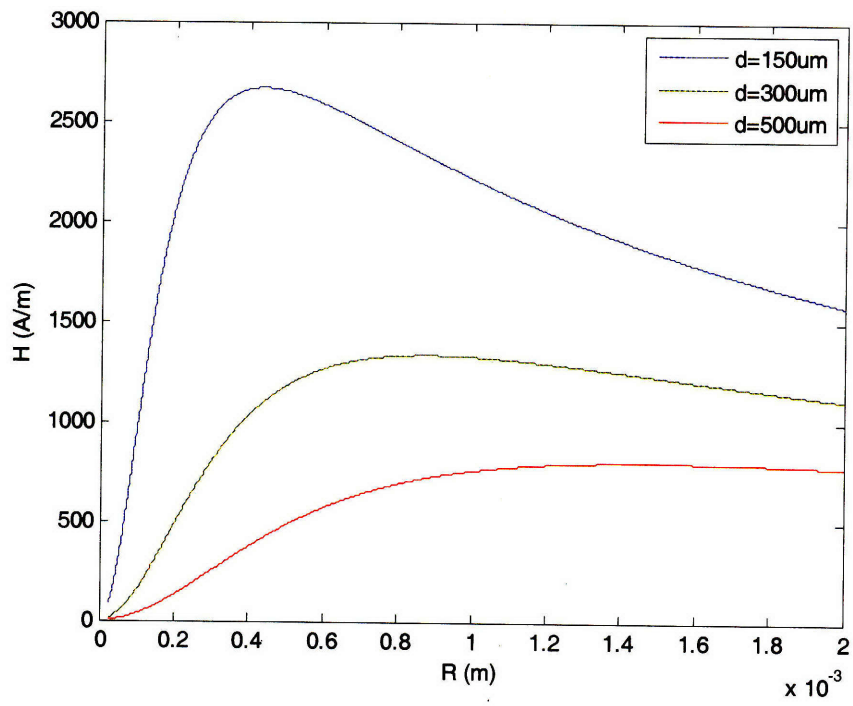
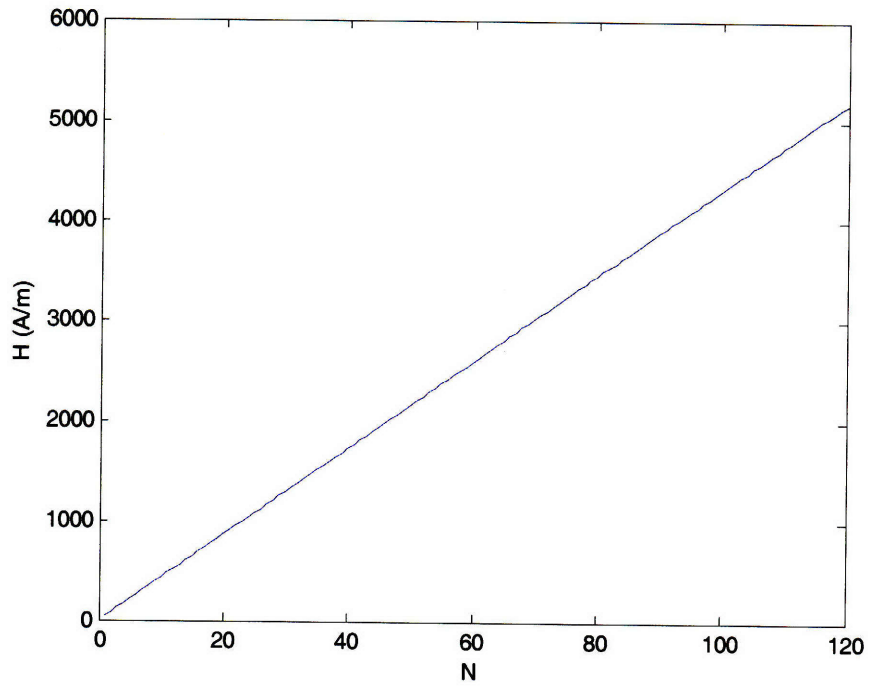


Fig. 4.7 – Step response of thermal circuit. Temperature increase is nearly instantaneous varying by only little more than 1°C after $t=0^+$.

The magnetic field strength established by these parameters is 2.59kA/m. The dependence of field strength based on the various parameters is shown in Fig. 4.8. One should note that these dependencies shift based upon changes in the other parameters. The plots shown are based upon the values specified above. Fig. 4.8(b) includes multiple plots for the varying values of d .



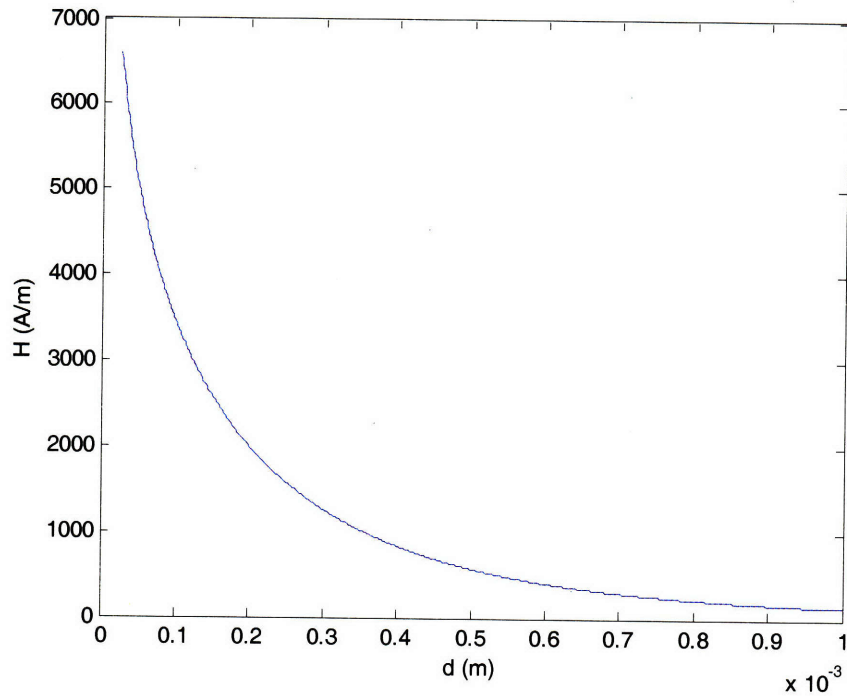


Fig. 4.8 – Dependencies of magnetic field strength on the various parameters: (a) number of coils, N ; (b) outer radius of coil, R , for various values of d ; (c) distance from the gel to the coil, d .

Also of interest to the designer is the distance in the plane of the gel that the magnetic field drops off, a . This is of importance in determining how closely the valves can be placed next to each other without causing any unwanted interference or heating from an adjacent coil. Additionally, one may be interested in how much of the field is in the center of the gel in comparison to the outside. Eq. 2.147 defines this behavior and is solved numerically using MATLAB® (MathWorks). The results are shown in Fig. 4.9.

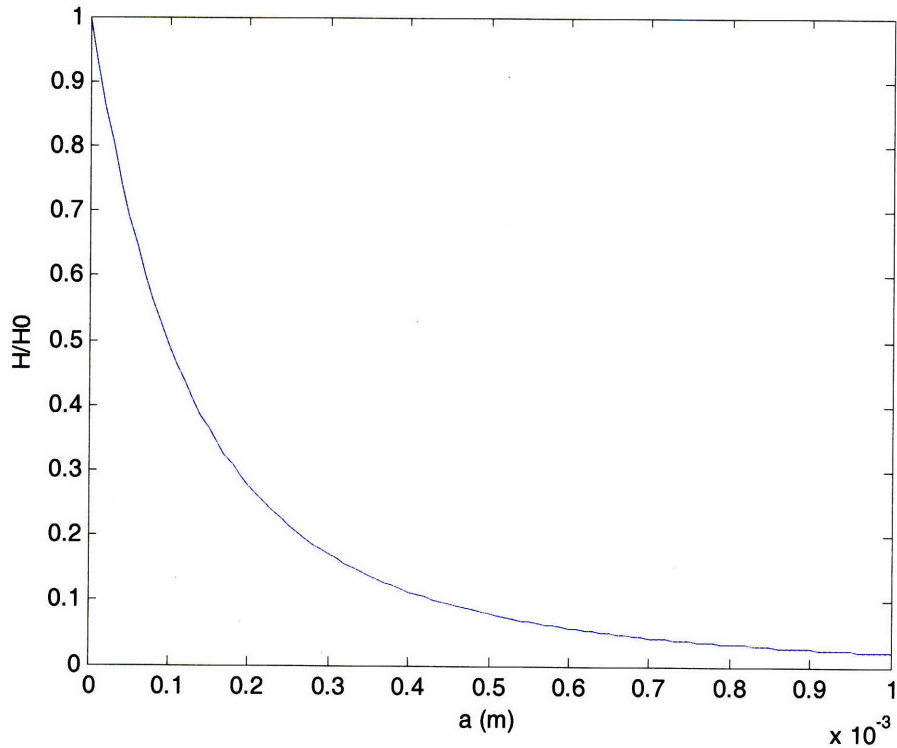


Fig. 4.9 – Relative magnetic field strength as a function of distance away from the center of the gel. The rapid drop off suggests that the valves can be placed close to each other.

From this figure, one can see that the field strength drops off very rapidly off axis. At about $450\mu\text{m}$, the field strength is only about ten percent of what it is on-axis. This is useful because it allows the designer to place multiple valves very close to each other without worrying about accidentally opening unintended valves. It does, however, pose concerns regarding the heating throughout the gel. If only the center is heated up at the assumed rate the gel may not shrink as quickly. As it turns out, this is not much of a concern since the characteristic timescale of heat conduction through the gel is much faster than the shrinking time constant. This was described already in Section 2.4. Thus, under the assumption that the models presented in Chapter 2 are correct, the chosen design parameters for the coil should satisfy the prescribed functional requirements of the valve.

5. Fabrication

5.1 Original Design Fabrication

The original design that was fabricated was discussed in Section 3.3. This design consisted of a channel made out of PDMS and bonded to a glass substrate. The channel had a post in its center around which a poly(NIPAAm) plug was patterned by means of photolithography. The intention was that, when the plug was in its swollen state, it would span the width of the channel and block fluid flow. When heated by the magnetic nanoparticles, the hydrogel would shrink to allow flow through the channel. Similar designs to this one can be found in the literature [4, 6, 7] where substrates other than PDMS were used.

The fabrication process for this design is based upon the simple techniques of soft lithography (Fig. 5.1). First, SU-8 is spun onto a silicon wafer to a thickness of approximately 100 μ m and patterned using photolithography with an interval expose on a conventional mask aligner (Electronic Visions Model EV620). After baking and developing the SU-8 master, PDMS is poured onto it and cured at approximately 80°C for one to two hours. The PDMS is mixed in a 10:1 weight ratio of base to curing agent and is degassed for approximately thirty minutes in a benchtop desiccator. The PDMS used for these experiments was Sylgard 184 by Dow Corning. After curing, the PDMS was peeled off of the master. Because the thickness of the PDMS was so large, no surface treatment of the SU-8 master was necessary; however, for smaller thicknesses, one can silanize the wafer using a product such as Trichloro(1H,1H,2H,2H-Perfluorooctyl)-Silane. The PDMS was then bonded to a glass slide using air plasma. This is done by subjecting the PDMS and glass to 1000Watts of RF plasma in an asher for seventeen seconds and then contacting them together. The plasma oxidation acts to replace some of the methyl groups on the PDMS surface with hydroxide groups. These hydroxide groups then form covalent bonds with the silicon and oxygen atoms on the surface of the glass.

Because the bonds are covalent, the bond between the PDMS and glass is permanent. Blunt hypodermic needles (21 gauge) are used to produce inlet and outlet holes in the PDMS.

After the chip has been assembled, a NIPAAm prepolymer solution that contains a photoinitiator is flowed into the channel. The solution is composed of 2.18:0.124:3.0:1.0:0.154 *N*-isopropylacrylamide (NIPAAm) : *N,N'*-methylenebisacrylamide (NMBA) : Dimethyl Sulfoxide (DMSO): deionized water: 2,2-Dimethoxy-2-phenylacetophenone (DMPA) by weight. The NMBA is the cross-linking agent, the DMPA (Aldrich 196118) is the photoinitiator (data sheet available in Appendix 3), and the DMSO and water are solvents. This solution is based upon previously reported results [96]. Polymerization of the NIPAAm is carried out using a standard mask aligner (Karl-Suss MJB3) with a chuck that has been fabricated for this purpose (Appendix 4). Exposure times can vary for anywhere from five seconds to one minute depending on the degree of cross-linking desired. After polymerization, the device is heated, and the unpolymerized solution is washed out of the channels with water.

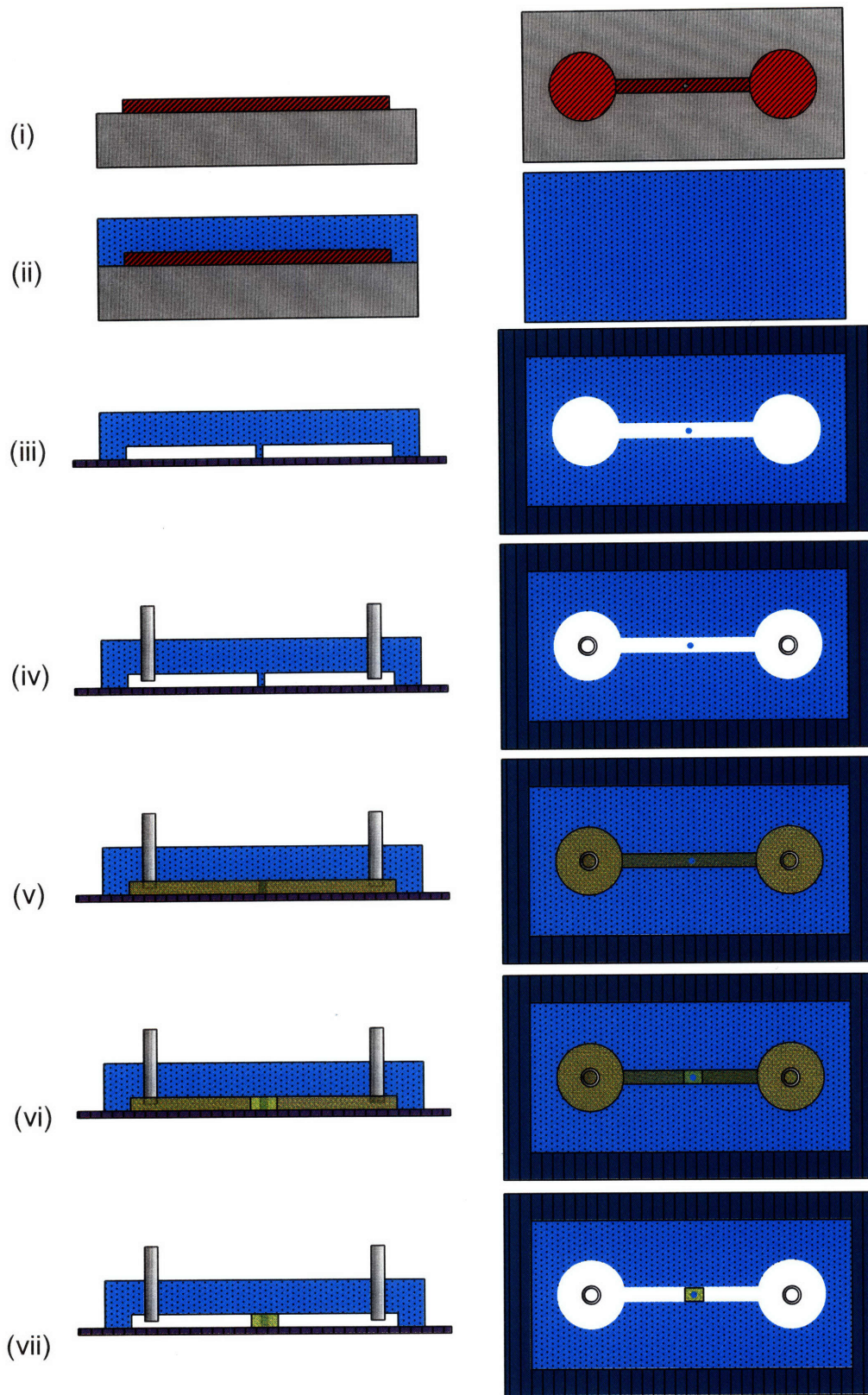


Fig. 5.1 – Fabrication process for the original design: (i) spin and pattern SU-8; (ii) mold PDMS off of wafer; (iii) peel of PDMS and bond to glass slide; (iv) insert hypodermic tubing; (v) flow NIPAAm prepolymer into channel; (vi) pattern poly(NIPAAm) around post; (vii) wash away remaining prepolymer solution

Fig. 5.2 shows the results of this method for two different exposure times. A more comprehensive chart of polymerizations in these channels can be found in Appendix 1. It is interesting to note that, for the interval exposure method, there is some fuzziness due to molecular diffusion. When an interval expose is used, the polymerized molecules around the edge have time to diffuse during the interval between exposures causing a gradient in crosslinking at the edges.

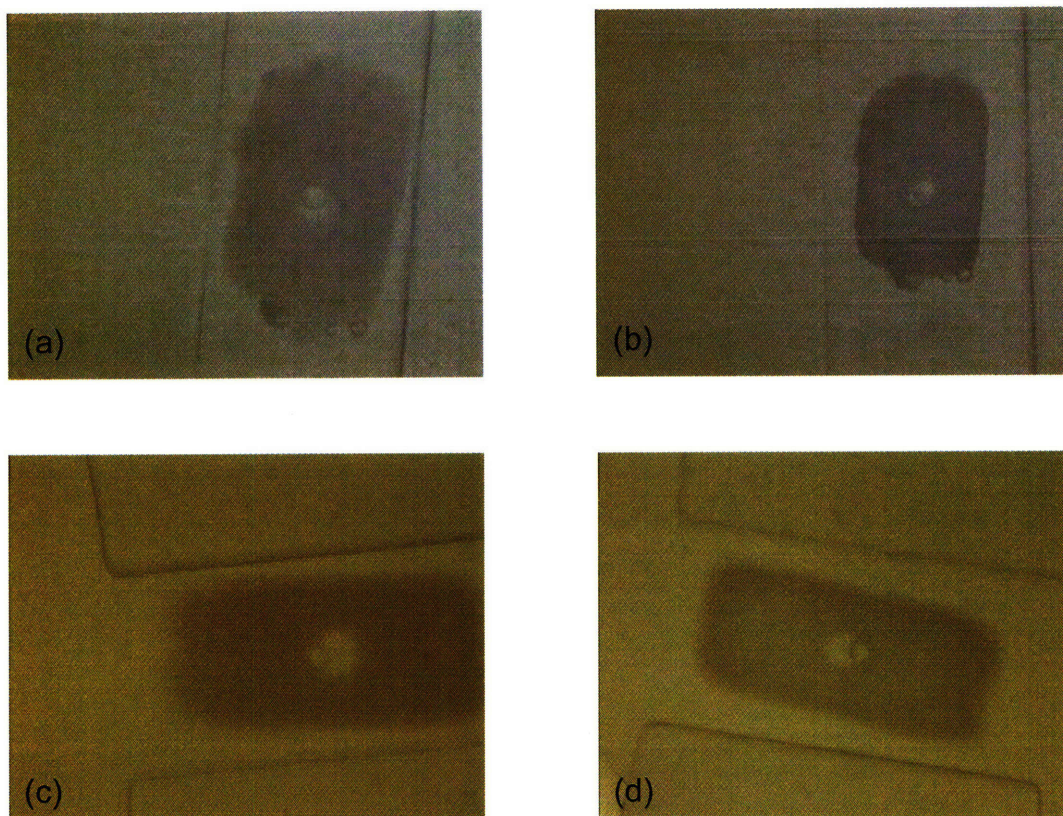


Fig. 5.2 – Valves fabricated using the original valve design: (a) continuous 10sec exposure; (b) after heating valve (a); (c) 15 sec interval expose (5 x 3sec); (d) after heating valve (c). Presence of an oxygen inhibition layer is visible in (a) and (c).

More important than the fuzziness, however, is the presence of oxygen inhibition. As was discussed in Sections 2.6 and 4.1, the presence of molecular oxygen can inhibit free radical polymerization. The oxygen reaches the channel since PDMS is permeable to it. This effect scales as

$$L \sim \sqrt{\frac{D}{k}} \quad (5.1)$$

where D is the coefficient of diffusion of O_2 in the NIPAAm prepolymer and k is the pseudo first order rate constant [84]. As mentioned in Section 4.1, one would expect this length to be on the order of tens of microns. The lengths in Fig 5.2(a) and (c) are on this order, thus confirming the suspicions that oxygen inhibition is the reason for this lack of polymerization at the edges. To further validate this assumption, the same experiment was carried out in a commercially available rectangular glass capillary. Results from this test show that the poly(NIPAAm) polymerized to the edge of the channel (Fig. 5.3). This is due to the fact that glass is impermeable to the molecular oxygen, and thus there is no inhibition.

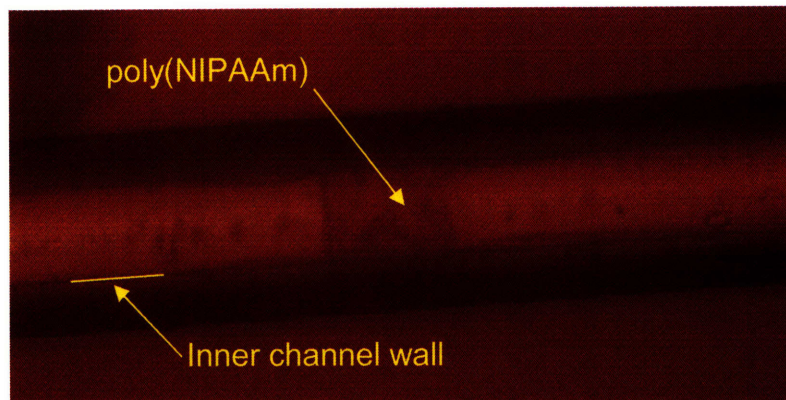


Fig. 5.3 – Polymerization of poly(NIPAAm) in a rectangular glass capillary. Since there is not oxygen present, polymerization can occur up to the edges of the channel.

Additional problems with this design became apparent after fabrication. The first was that after polymerizing the NIPAAm, it did not shrink when heated above its LCST (Fig. 5.4(b)). While the exact reasons for this are unknown, it is likely due to the use of DMSO as one of the solvents in the prepolymer solution. DMSO is a polar aprotic solvent that can dissolve polar and nonpolar solutes. Because of this, the changes in hydrophobicity with temperature of the poly(NIPAAm) likely have no effect on the expulsion of DMSO. Therefore, because the solvent is not forced out of the interstitial spaces in the hydrogel network, no shrinking is observed. Because of this lack of shrinking, the oxygen inhibition actually helps this device in that the prepolymer can still be flushed out. Since

there are gaps between the wall and the hydrogel on both sides, water can be pushed through the channel in order to wash out the prepolymer. The poly(NIPAAm) can then undergo shrinking since it is filled with only water rather than the DMSO-Water hybrid solvent.

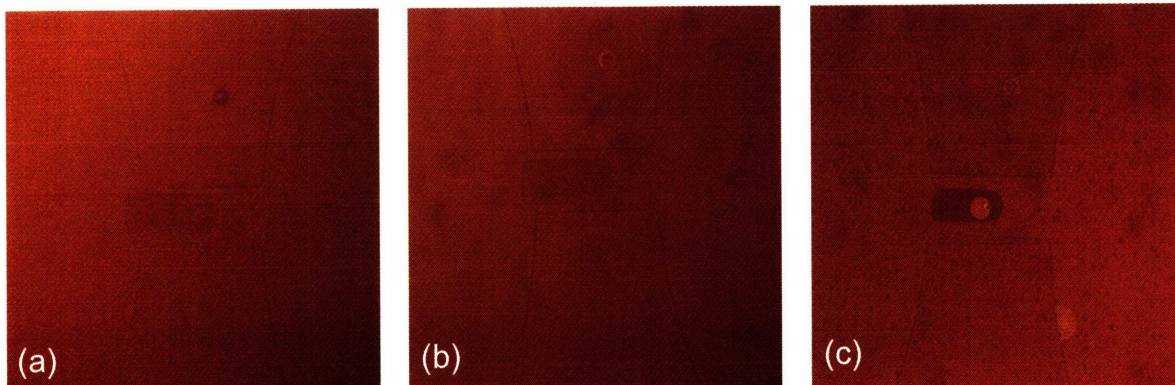


Fig. 5.4 – Heating poly(NIPAAm) before washing: (a) immediately after polymerization; (b) after applying heat but prior to washing with water; (c) after washing with water and applying heat

One other problem that resulted from this fabrication was that the post often did not bond to the glass. This was likely due to the high aspect ratio of the post. Since PDMS has such a low modulus of elasticity, the post may not have had a high enough stiffness to ensure that it would always stay vertical during the bonding process. Fig. 5.5 shows the results of a valve fabricated in a device where the post was not bonded to the glass. Flow caused the poly(NIPAAm) plug to be pushed out of the channel since there was no post to hold it in place.

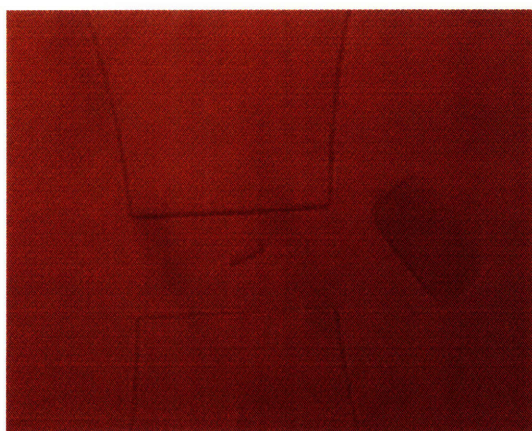


Fig. 5.5 – Lack of bonding between the PDMS post and glass allows poly(NIPAAm) plug to be pushed off of it in the presence of flow. This problem is due to the high aspect ratio of the channel height compared to its diameter.

5.2 Final Device Fabrication

Due to the issues discussed in the previous section, a new design was constructed using the Axiomatic Design framework (Chapter 3). This section discussed the fabrication techniques utilized in the fabrication of this design.

5.2.1 Process Flow

The first iteration of this design was intended to be a prototype used to demonstrate the principle of operation and its feasibility. The materials and fabrication methods used are not recommended for use in high volume manufacturing of this design, but were used to quickly demonstrate the intended purpose. Additionally, no MEMS magnetic coil was fabricated in this design in order to simplify the fabrication.

A full process flow is shown in Fig. 5.6 for the portion of the device fabricated in the cleanroom. First, the glass wafer is cleaned using a piranha bath (1:3 H_2O_2 : H_2SO_4) for ten minutes. Immediately afterwards, it is rinsed in a spin rinse drier, and put directly into an electron-beam evaporation machine. 200Å of chromium are evaporated to serve as an adhesion layer, and 2000Å of gold are evaporated to serve as the hard mask and anchor top. These metals are deposited on both sides of the wafer. Photolithography is performed next using one micron of OCG 825 resist. It is spun onto the wafer (~3000rpm), baked at 95°C for fifteen minutes, spun onto the other side, baked at 95°C for thirty minutes, exposed for 1.7 seconds on an Electronic Visions Model EV620 aligner, developed in OCG 934 1:1 developer until the features clear (about one minute), and postbaked at 120°C for thirty minutes.

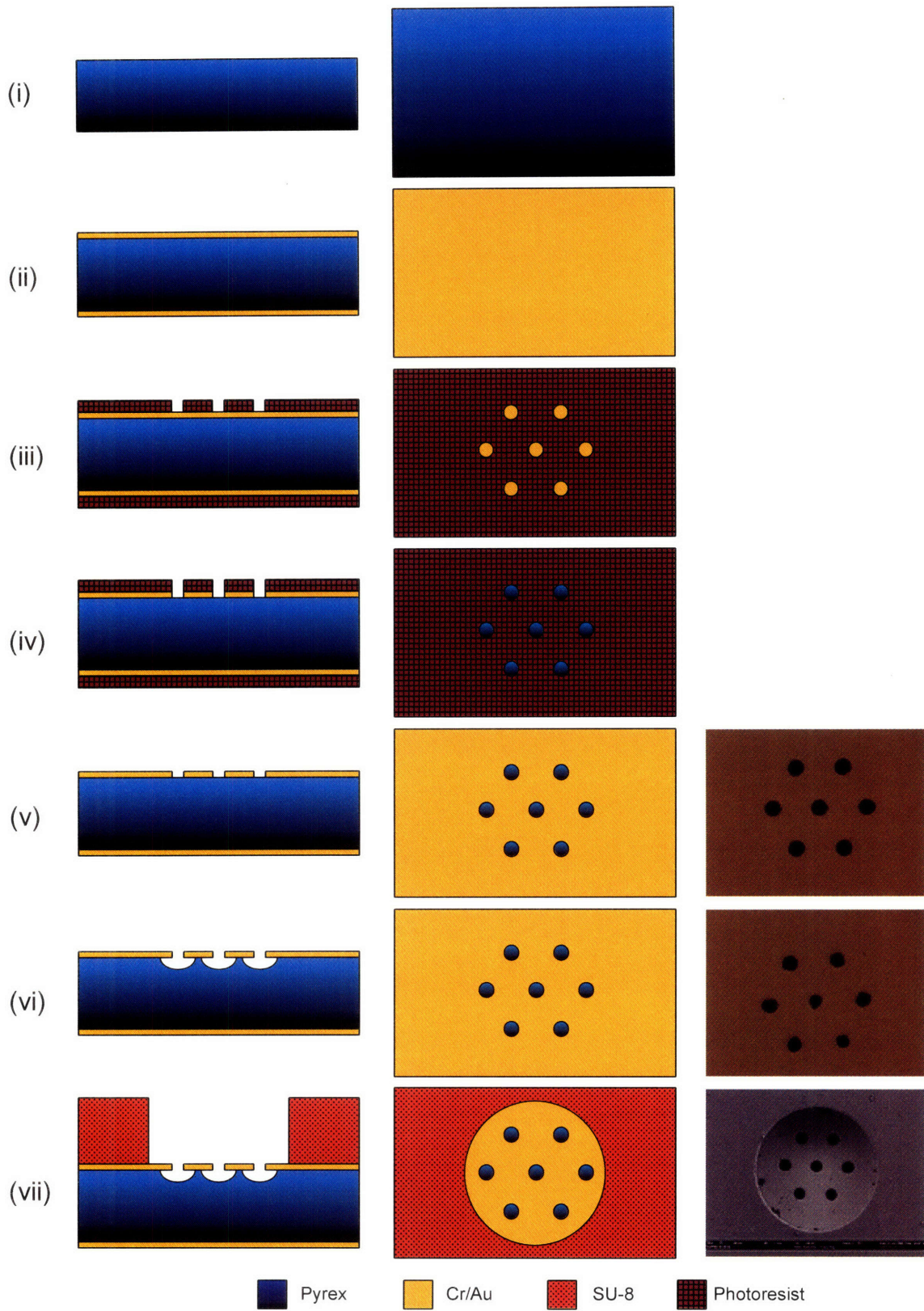


Fig. 5.6 – Process flow for cleanroom-based portion of fabrication: (i) piranha clean; (ii) evaporation of Cr (200Å) and Au (2000Å); (iii) spin, expose, and develop 1µm OCG resist (both sides); (iv) wet etch Cr and Au; (v) wet etch glass; (vi) spin, expose, and develop SU-8. Images in third column are from actual device fabrication.

After the photolithography, the hard mask is wet etched using a potassium-iodine based gold etchant and CR-7 to pattern the gold and chrome layers respectively. A 1:1 deionized water : hydrofluoric acid solution is then used to isotropically etch the glass wafer. Finally, SU-8 2050 (Microchem) is spun to a thickness of approximately 100 μ m, prebaked at 65°C and 95°C on hotplates, exposed for approximately 25-30 seconds (5 second intervals with 15 second waits), postbaked at 65°C and 95°C, developed with propylene glycol monomethyl ether acetate (PM Acetate), and rinsed with isopropanol and water.

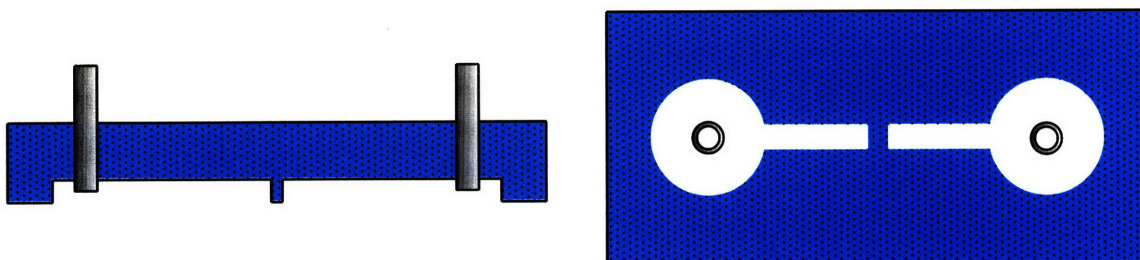


Fig. 5.7 – PDMS channel design fabricated using standard soft lithography cast off of an SU-8 master. A discontinuity at the middle of the channel prevents flow until the valve is opened.

PDMS channels are fabricated using the same technique as described in Section 5.1 with the exception that the channel design varies slightly to contain a discontinuity (Fig. 5.7). After the microwells are fabricated according to the previously described micromachining process, they are filled with the NIPAAm prepolymer solution. This is done using a thermal inkjet printing tool developed by Hewlett Packard. This process will be described in more detail in Section 5.2.2.2. The solution is then polymerized using a handheld UV lamp (Spectroline Model EA-160) for thirty seconds. Finally, the channel is fixed on top of the substrate by hand.

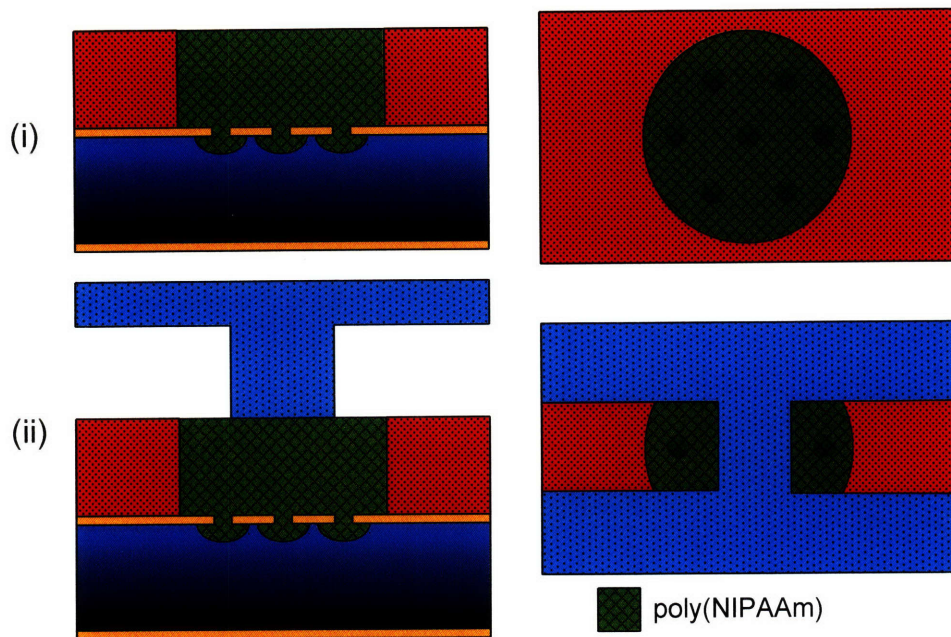


Fig. 5.8 – Final process steps: (i) print prepolymer into well and polymerize; (ii) attach PDMS channel

5.2.2 Fabrication Details and Results

5.2.2.1 Wet Etching of Glass

In order to fabricate the anchors for the poly(NIPAAm) plug, isotropic wet etching of the glass substrate was performed. Isotropic wet etches to controlled depths are difficult to achieve in the absence of an etch stop. They should be carefully timed and characterized in order to achieve repeatable results. The design of the valves was robust enough that an exact depth was not necessary. Nonetheless, the design and subsequent masks were prepared under the assumption that the lateral and vertical etch rates are the same for isotropic etchants. This has been the general understanding in the literature [75]. That is to say that the distance undercut would be the same as the depth of the etch (Fig. 5.9(a)).

Unfortunately, experimental results showed that the lateral etch rate is in fact much greater than the vertical one for the prepared solution. In order to isotropically etch glass, hydrofluoric acid (HF) was used with the aforementioned chrome-gold hard mask. In

order to reduce the speed at which the glass was etched, the acid was diluted with deionized water in the ratio 1:1 HF:H₂O.

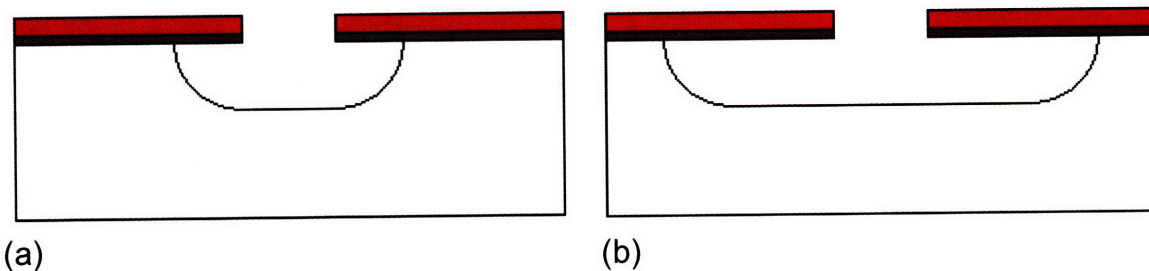


Fig. 5.9 – Isotropic wet etching of glass: a) Expected profile (1:1 Lateral:Vertical Etch Rates) b) Actual profile (lateral rate \gg vertical rate)

The first devices were fabricated using a ten minute etch. The results of this etch can be seen in Figure 5.10 and Figure 5.11. In those figures, the devices have been cross-sectioned using a diesaw and imaged with a SEM. The force from the water jets on the diesaw caused the metal hard mask to be removed above the area etched out by the HF solution. This allows for a clear depiction of the extent to which the glass was etched laterally. The anchors were etched so significantly that they became overlapped and resulted in a single large trench. From Figure 5.10, it can be easily seen that the amount of lateral etching far exceeds that of the vertical etching. Figure 5.11 depicts the original size and location of the holes in the hard mask (blue) and the extent to which the mask was underetched (yellow). From this image, it can be determined that the final diameter of the holes is approximately 135 μ m. This suggests that in ten minutes, the solution etched a radial distance of approximately seventy microns. Because the design called for a radial distance of around fifteen microns, it was necessary to characterize the etch rate of the 1:1 HF:DI solution.

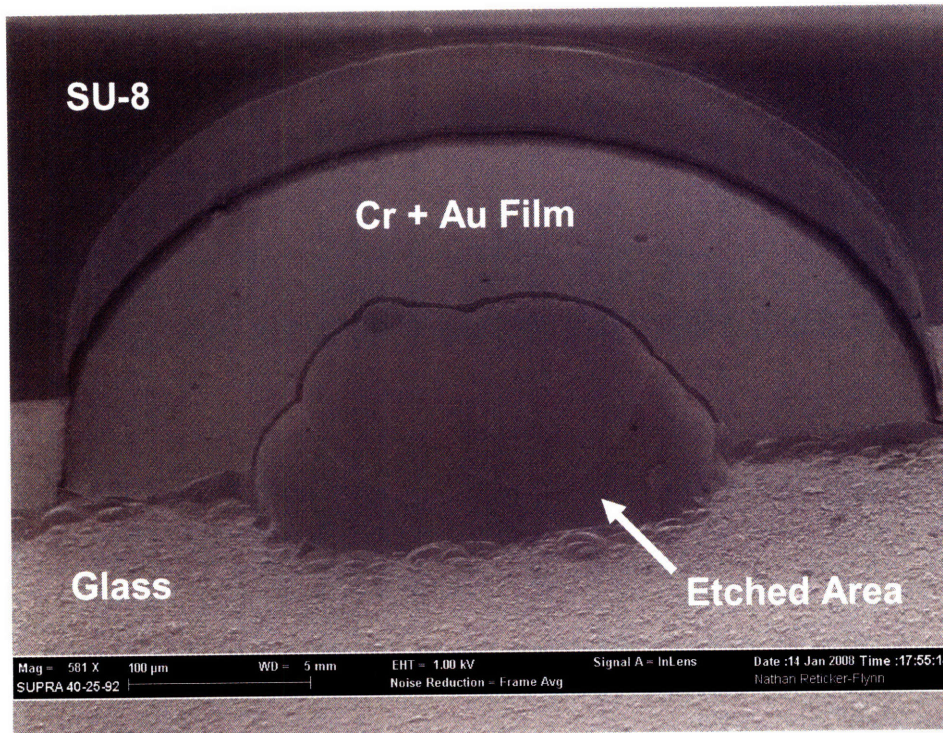


Fig. 5.10 – SEM image of first device. SU8 well is 500 μ m. Wafer has been cut in the diesaw. Gold film has been removed over the etched area. Individual anchors holes have been overetched resulting in diameters of approximately 135 μ m. It is clear that lateral etch rates far exceed vertical etch rates.

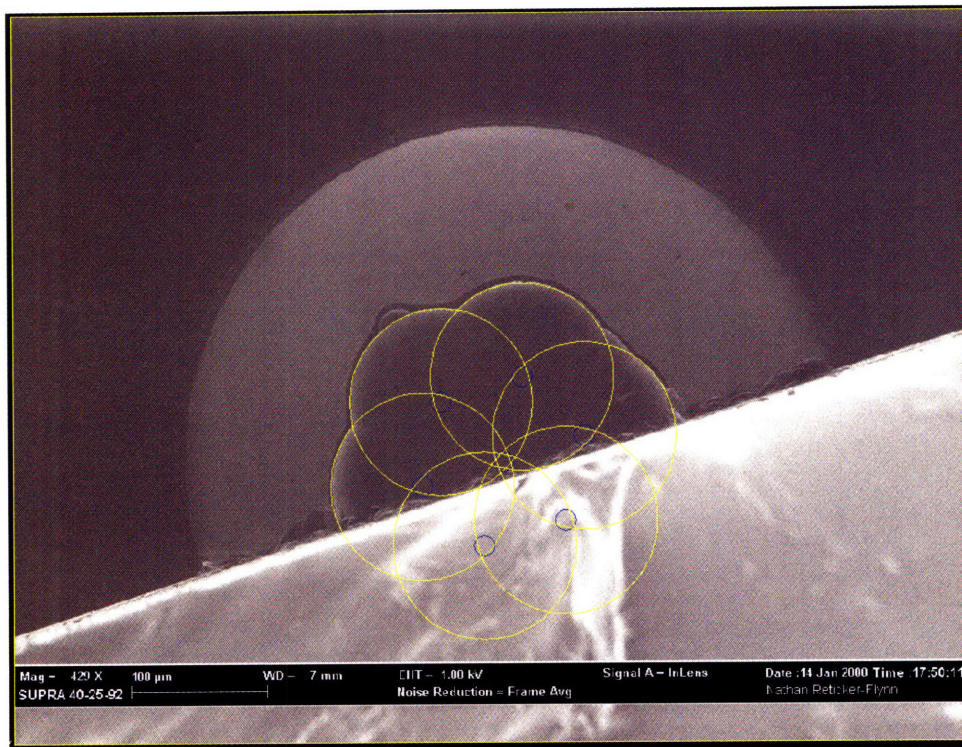
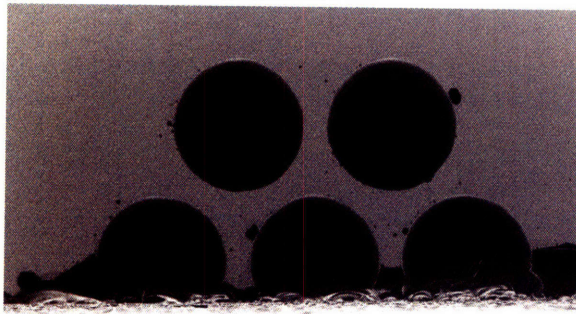


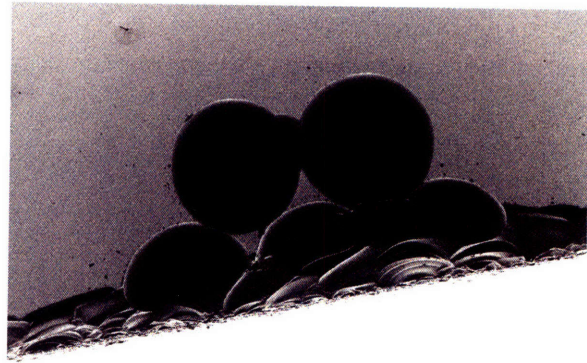
Fig. 5.11 – SEM image of first device. Blue circles represent the location and size (15 μ m diameter) of the holes in the metal hard mask. Yellow circles represent the final geometry of the etched anchors (~135 μ m diameter).

Etch rates were characterized by exposing samples to various etch times. One wafer was prepared with the hard mask and cut into dies containing two sets of anchors using the diesaw. The samples were then placed into the HF solution for times ranging from one to eight minutes. No agitation was used during the etching as sufficient amounts of etchant were reaching the surface and agitation often promotes higher lateral etch rates [97]. The samples were immediately rinsed with water and dried with nitrogen after the etching was complete.

To determine the degree of lateral etching, the samples were again cut using the diesaw. As previously mentioned, the force from the water used during the cutting removed the metal hardmask above where the glass was etched, but not in the surrounding area. This allowed for easy visualization of the extent of the etching. Figure 5.12 shows the various amounts of etching for the different etch times. Figure 5.13 shows the dependence of lateral etching on time. From this graph, one can use the linear fit to determine the etch rate (approximately $5.1 \mu\text{m}/\text{min}$). Additionally, the zero-minute etch distance can be extrapolated. The fact that it is not zero ($20.6 \mu\text{m}$) suggests that the etching may have begun at a further radial distance than the hardmask.

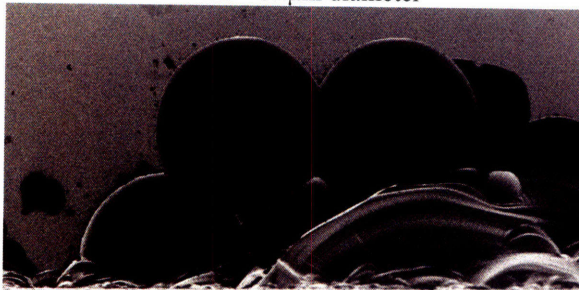


Mag = 1.27 K X 20 µm WD = 6 mm EHT = 1.00 kV Signal A = Int.ens Date: 10 Jan 2003 Time: 8:29:46
SUPRA 40-25-92 Noise Reduction = Frame Avg



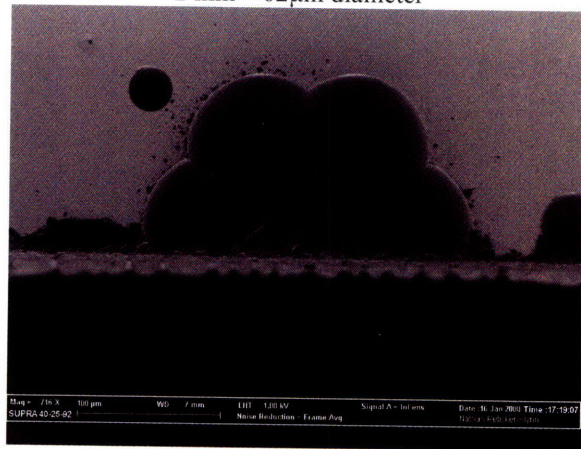
Mag = 1.07 K X 20 µm WD = 6 mm EHT = 1.00 kV Signal A = Int.ens Date: 10 Jan 2003 Time: 8:37:45
SUPRA 40-25-92 Noise Reduction = Frame Avg

1 min – 52µm diameter



Mag = 1.14 K X 20 µm WD = 6 mm EHT = 1.00 kV Signal A = Int.ens Date: 10 Jan 2003 Time: 8:45:13
SUPRA 40-25-92 Noise Reduction = Frame Avg

2 min – 62µm diameter



Mag = 7.06 X 100 µm WD = 7 mm EHT = 1.00 kV Signal A = Int.ens Date: 10 Jan 2003 Time: 17:19:07
SUPRA 40-25-92 Noise Reduction = Frame Avg

3 min – 70µm diameter

6 min – 103µm diameter

Fig. 5.12 – Characterization of lateral etch rates of 1:1 HF:DI Water on glass. Hard mask had an original diameter of 15µm.

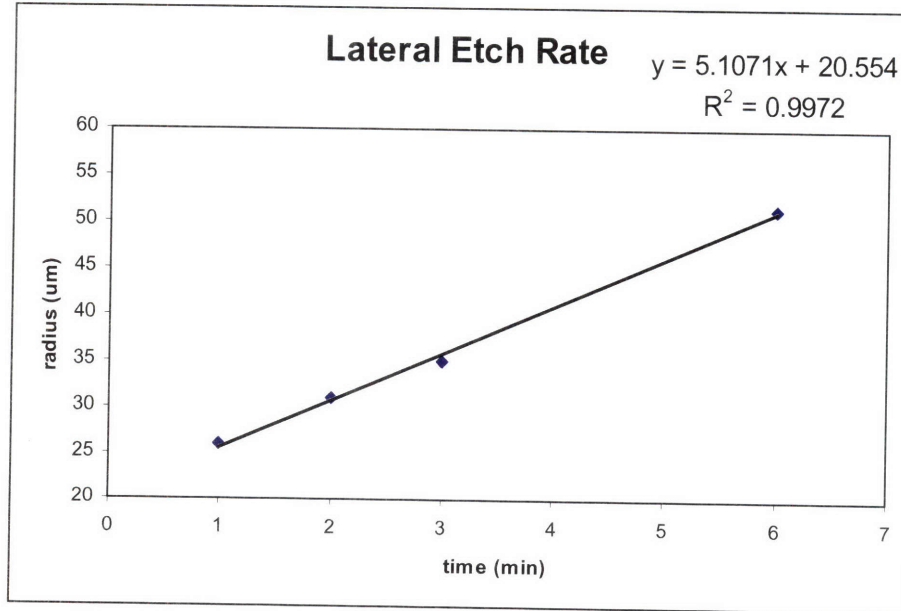


Fig. 5.13 – Radius of anchor as a function of etch time. Linear fit suggests a lateral etch rate of 5.1µm/min. Starting radius of 20.6µm is much larger than the 7.5µm supposedly defined by the mask.

It was suggested that the 200Å chrome adhesion layer of the hard mask may have been overetched beneath the 2000Å gold layer. Since the starting distance of the etching appeared to be much further than the edge of the hard mask but the hole in the gold film appeared to be the correct size, it is likely that the discrepancy came from the chrome. Furthermore, careful examination of optical images prior to etching the glass shows a faint ring outside of the hole that may be evidence of a larger diameter hole in the chrome layer (Figs. 5.14 and 5.15). When preparing a second set of devices the chrome layer was etched for a shorter time (approximately 25sec) in CR-7 rather than the previous two minutes. The results of the decreased chrome etch time show that the initial diameter of the etching area was indeed much smaller. For the same etch times, the final diameters of the anchors were about twenty microns smaller (Fig. 5.16).

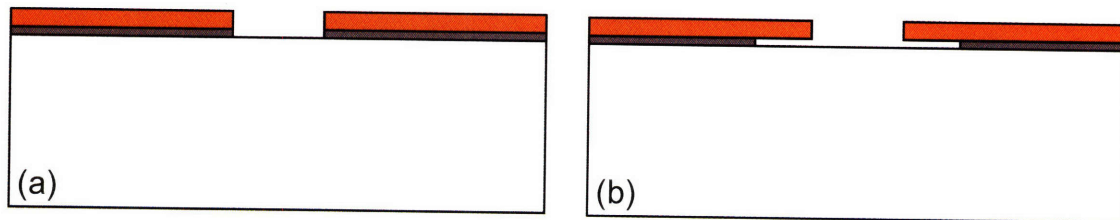


Fig. 5.14 – Etching of hard mask: (a) intended profile, (b) overetching of chrome layer allows more of substrate surface to contact HF solution

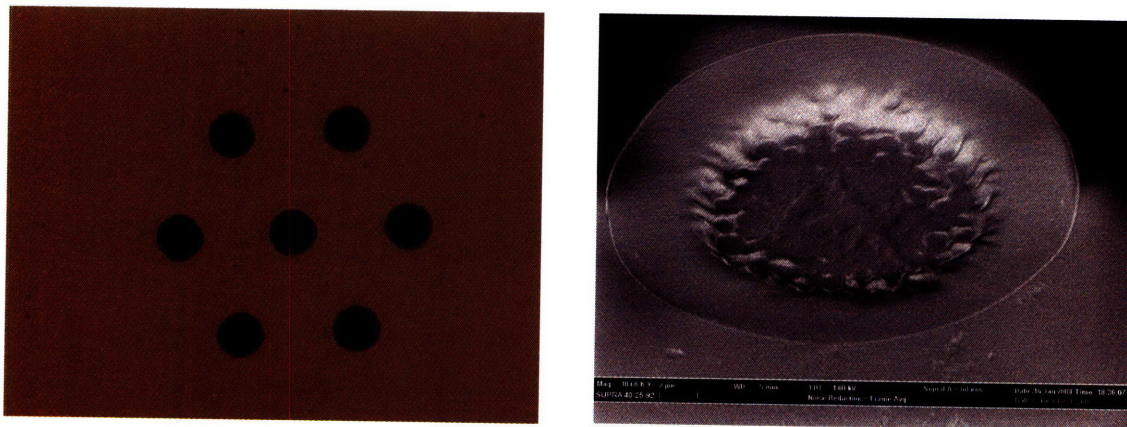
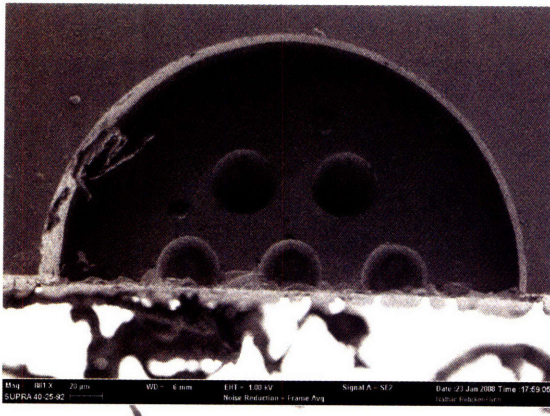


Fig. 5.15 – Overetching of chrome beneath the gold results in increased diameters and lateral etching of the anchor holes.



39µm diameter



36µm diameter

Fig. 5.16 – Reduced CR-7 etch times resulted in smaller diameter anchors after one minute HF etches.

To confirm the validity of the undercut, a focused ion beam (FIB) was used to remove a portion of the gold-chrome layer above one of the anchors (Fig. 5.17). Clear undercut can be seen that demonstrates the validity of the etching process and integrity of the metal layer.

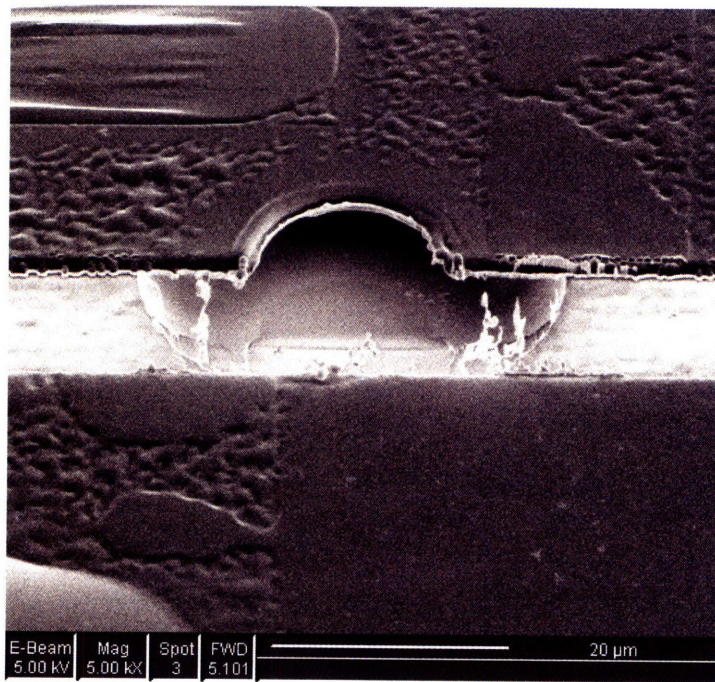


Fig. 5.17 – SEM of one anchor after removal of a rectangular portion of the chrome-gold layer. Undercut and vertical etching of the glass are visible.

5.2.2.2 Printing

After the microwells have been fabricated in a cleanroom, they are filled with the NIPAAm prepolymer. Due to their small diameters (200-500 μ m) and small volumes (3-20nL), they cannot be filled by hand or using conventional tools. Instead, a thermal ink-jet printing system developed by Hewlett Packard, known as the POEM system, was used. This system has the ability to print droplets with volumes on the order of a few picoliters with an accuracy of a few microns.

The system setup is shown in Fig. 5.18 and Fig. 5.19. The main component is the controller to which the printer tip is attached. This handheld device can be operated standalone or remotely via a USB port. It controls parameters such as the voltage supplied to the tip, the droplet jetting frequency, which nozzles are used (most tips have between 10-20 nozzles of varying sizes), along with other advanced parameters. Additionally, it monitors the current conditions such as back pressure and temperature. Careful control over all of these parameters is essential for successful printing of the “ink” being used.

A variety of different tips are available for the controller. These tips range in droplet volumes that they can produce. While it is often desirable to use smaller volume tips in order to have a fine resolution of the volumes being jetted, smaller nozzles can become clogged more easily depending on the solute sizes and jetting parameters. Because the volumes of the SU-8 wells were significantly larger than the droplet sizes on most all of the tips, it was fine to use the larger volume nozzles. The droplet sizes used in the fabrication of the valves ranged from 80-160pL. Droplet sizes are not exact, however, since the tips are calibrated to water. Thus, when the solvent is vaporized in the nozzle to create the expulsion of the droplet, different quantities than those specified by HP are jetted. Additionally, DMSO has a much higher boiling point (189°C) than water. Thus, the exact quantity expelled from the tip is unknown. This makes it difficult to predict the number of drops required to fill the well volume.

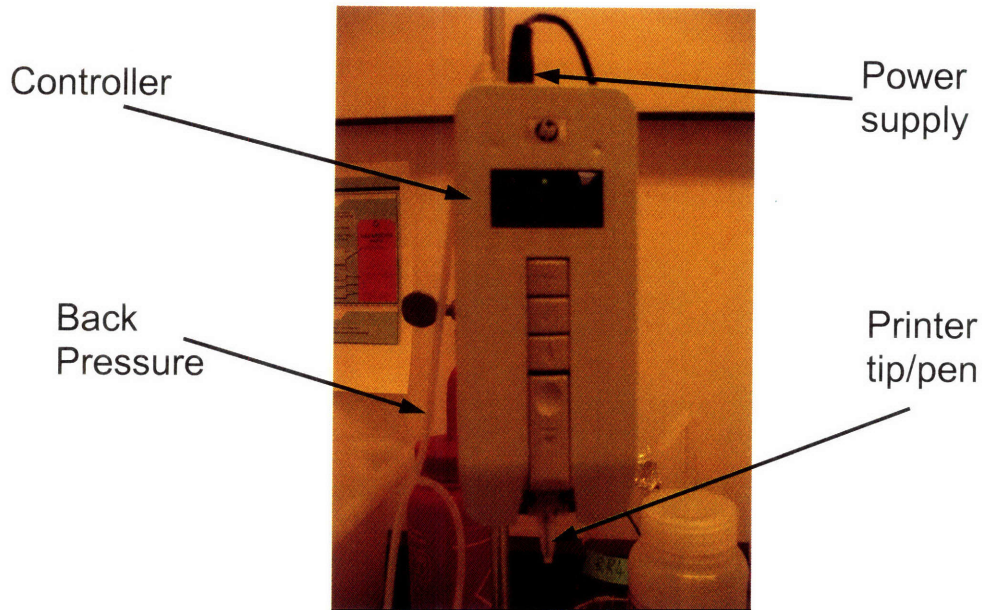


Fig. 5.18 – HP TIPS controller. This controller can be used on its own, or controlled remotely.

This issue is exasperated by the nonuniformity of the SU-8 layer. While the intended thickness was $100\mu\text{m}$, the actual thickness varied significantly across the wafer ($\pm 70\mu\text{m}$). This was a result of the nonuniformity of heating during the bake steps. The prebake and postbake steps were both performed on hotplates whose temperatures were set to be 65°C and 95°C (to allow for ramping of temperature). Due to the number of users in the facility, the hotplate surfaces had become warped preventing wafers from contacting their entire back surface to the hotplate. When using silicon as a substrate, this is not much of a problem since silicon is so thermally conductive that the heat distribution is essentially uniform. Glass, however, is not a good thermal conductor, and thus the temperature distribution, when contacting only a few points of the hotplate surface, is highly nonuniform. These changes in heating result in nonuniform thicknesses despite their uniformity immediately after spin coating. The effects can be seen in Fig. 5.20.

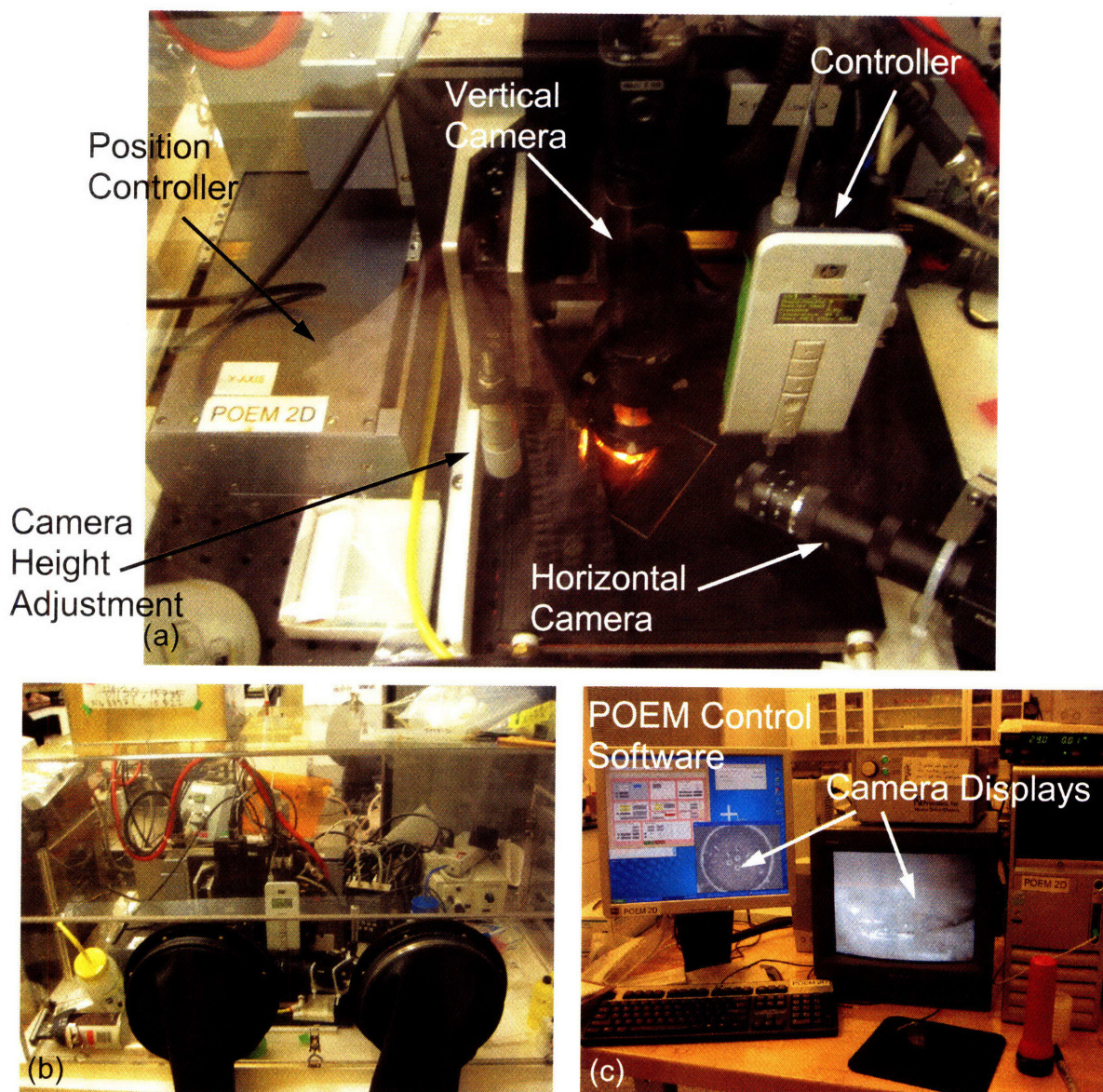


Fig. 5.19 – HP POEM thermal ink-jet printer setup: (a) two cameras assist in the alignment of the printer to the substrate; (b) entire system is operated from within a glovebox; (c) both the positioning and printing are controlled remotely.

Adding to the issues of varying well heights and droplet sizes, is the issues of evaporation and drying. When such small volumes of fluid are present they can quickly evaporate depending on the humidity of the surrounding air. Furthermore, there is the possibility of DMSO “freezing.” While it has a high boiling point (189°C), its melting point is just slightly below room temperature (18.45°C) [98]. If the solution is allowed to dry without first being polymerized, it can form strange crystalline-like structures that depend on the substrate (Fig. 5.21).

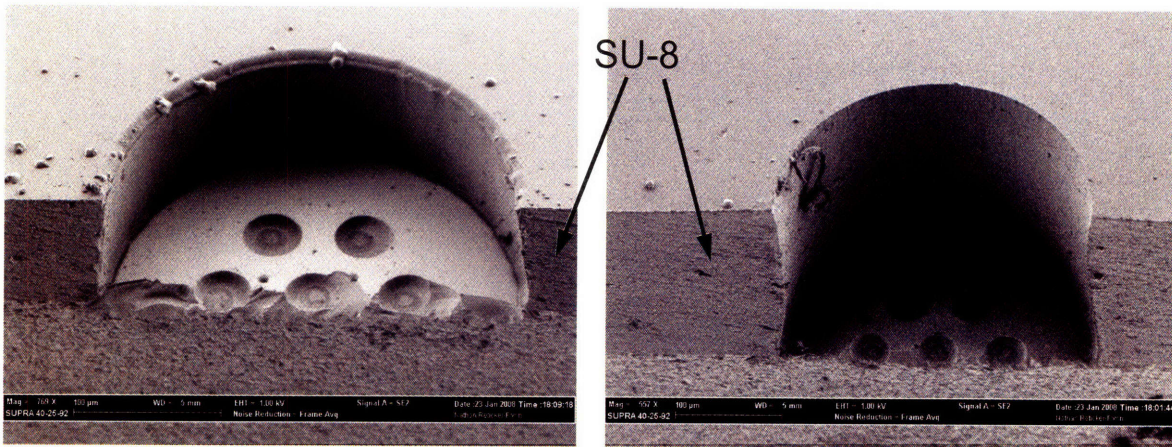


Fig. 5.20 – Nonuniformity of SU-8. Two wells on the same wafer were cut down the middle using a diesaw. SEMs of the wells show clear disparity in the thickness of the SU-8 layer.

All of these factors contribute to the fact that the number of droplets cannot be predicted prior to printing. This requires constant monitoring of the well during printing in order to ensure that the wells are not overfilled.

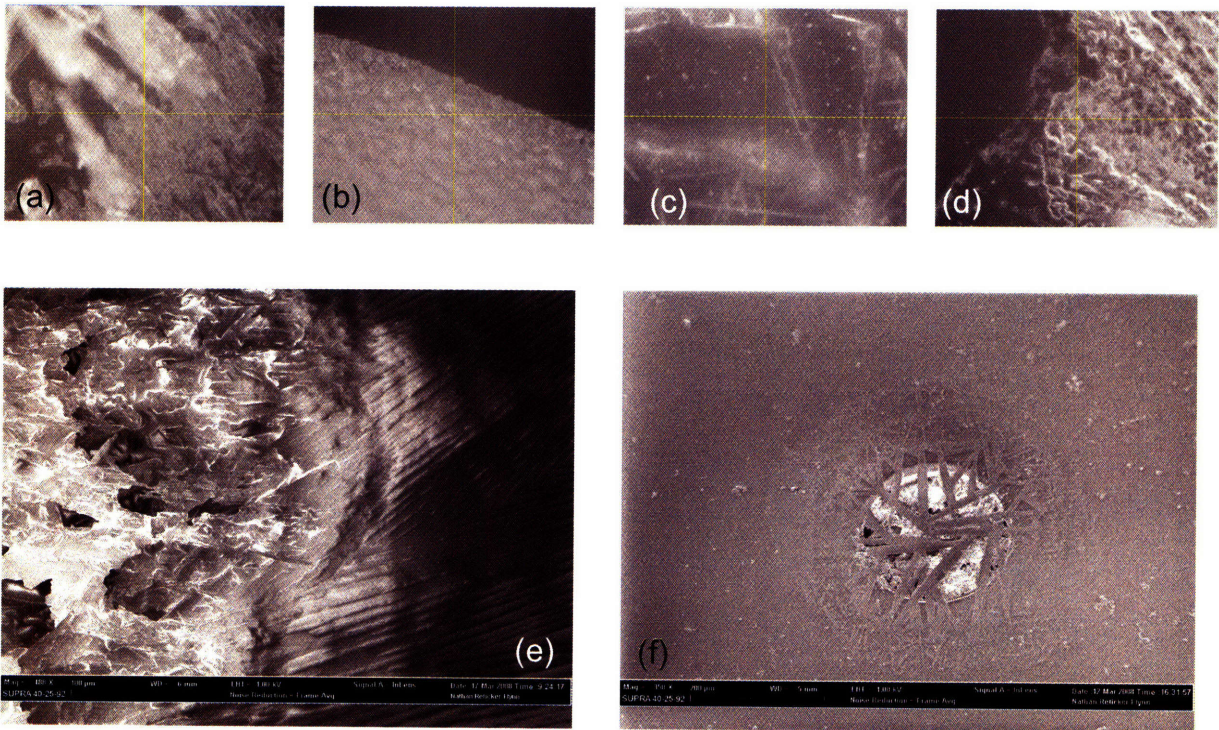


Fig. 5.21 – Effects of prepolymer drying. Optical images of unpolymerized dried prepolymer solution on (a) glass, (b) SU-8, (c) gold, and (d) silicon. (e) SEM of dried prepolymer on glass. (f) SEM of filled well that had unpolymerized solution dry on top. The crystalline-like structure creates a meshed pattern over the top of the well.

To monitor the filling of the wells, a vertical camera is used. This is the same camera that is used to align the wells to the printer. Unfortunately, this camera moves with the printer controller, and thus cannot be above the well during the printing. In order to monitor the filling of the well, one must print a few drops, move the camera over the well to inspect it, move the printer head back over the well, and repeat this process until the well is full. Because of the evaporation, drying, varying well depths, and varying droplet sizes, no two wells will be the same, and this process must be carried out for each well that is filled. The process can be difficult and problematic for a variety of reasons. Limited lighting is used since the ink is photosensitive. All lights are UV filtered with amber films, making imaging significantly more difficult. Additionally, a profile whereby the surface of the NIPAAm is above the surface of the well is desired in order to ensure a seal between the hydrogel and the PDMS channel. Because of this, one should fill the well such that the liquid at the center is higher than the surface of the SU-8, but still held into the well by surface tension (Fig. 5.22).

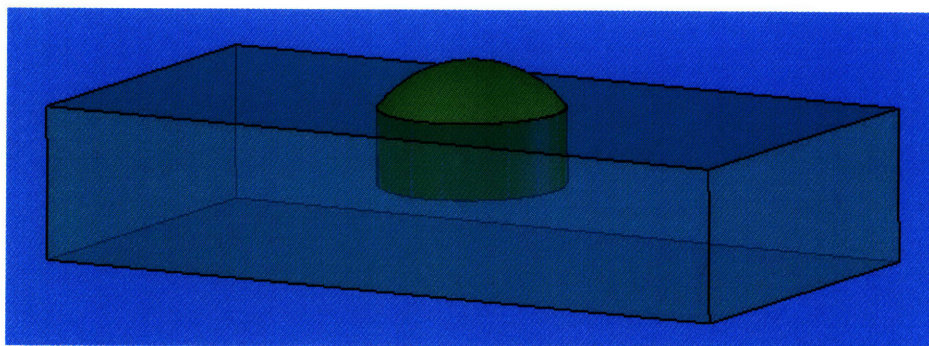


Fig. 5.22 – The NIPAAm prepolymer should be printed such that its profile is above the surface of the substrate, but does not spill out of the well. This is a careful balance between gravity and surface tension.

To increase the feasibility of this challenge, a horizontal camera was installed. While this camera greatly reduced the available stage area, its presence assisted in providing more insight into the degree to which the well was filled. Typical images acquired during the well filling are shown in Fig. 5.23. It is easy to see from these images how it can be difficult to determine if the well is completely filled.

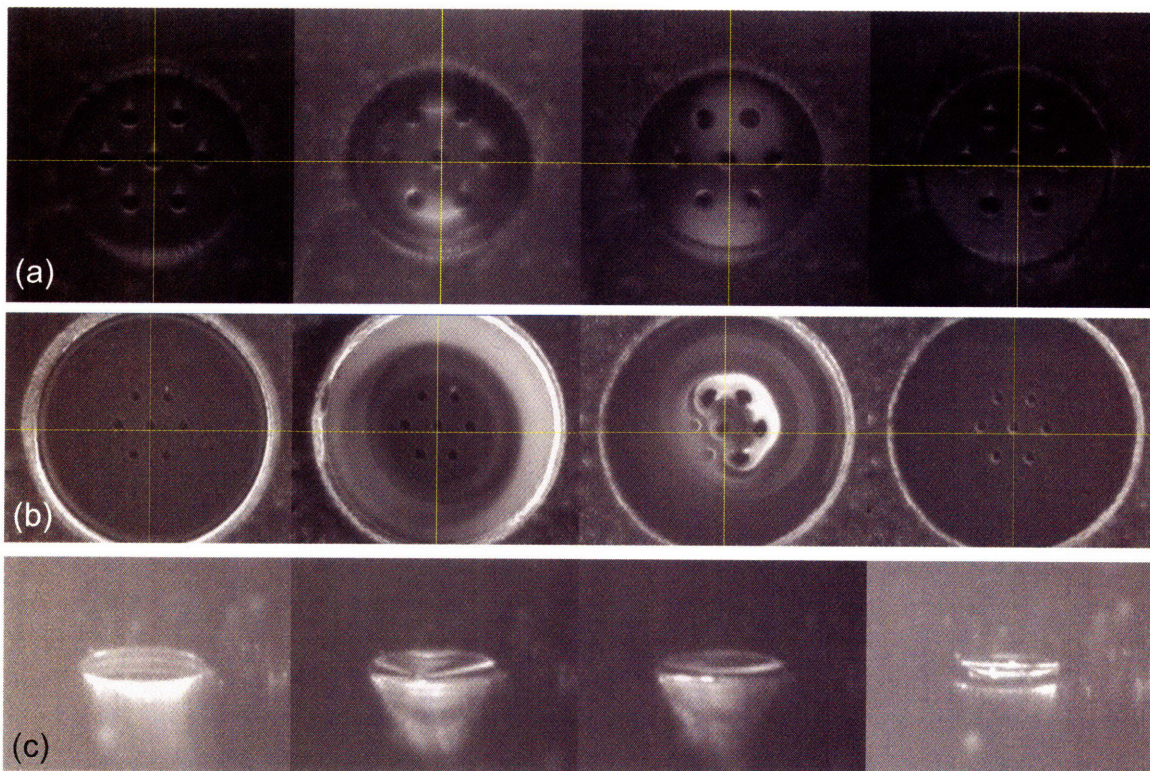


Fig. 5.23 – Images used to determine degree to which the wells are filled during printing. (a) and (b) are taken using the vertical camera when filling 250µm and 500µm wells respectively. Images in (c) are taken using the horizontal camera with a 500µm well.

5.2.2.3 Polymerization

After the prepolymer solution is printed into the wells it is polymerized by exposure to UV light. The exposure energy is the important parameter in that it determines the degree of crosslinking of the hydrogel. As was previously discussed, the amount of crosslinking affects the structural properties of the gel as well as the swelling ratio. From the mechanical perspective of the design, it is desirable to have a low hydraulic permeability and a high stiffness. These parameters usually require larger amounts of crosslinking. It is also desirable to maximize the swelling ratio; however, this requires smaller degrees of crosslinking.

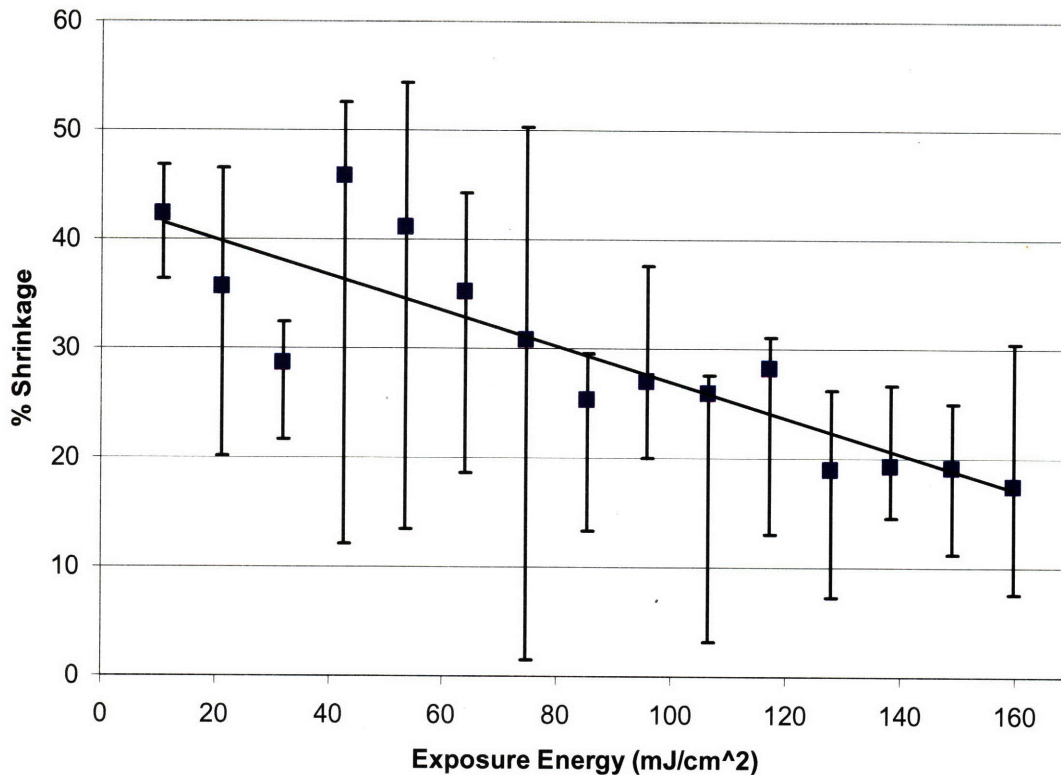


Fig. 5.24 – Effect of exposure energy on swelling ratio. Higher exposure energies result in smaller swelling ratios. Exposure energies based on exposure times and light power at 365nm.

In order to determine the amount of crosslinking that can be tolerated while still maintaining the swelling ratios required by the design parameters, it was necessary to characterize the amount of shrinking of the gel as a function of its exposure energy. This was determined by exposing 1 μ L droplets to UV light for varying amounts of time at five second intervals using a Spectroline Model EA-160 lamp. The results of these experiments are shown in Fig. 5.24. Exposure energies were determined from the product of the time and the light power. Power values were determined using a handheld light meter. The Spectroline lamp is intended to be a 365nm UV exposure lamp. Nonetheless, it produces significant amounts of power at other frequencies (Table 5.1). Exposure energies in Fig. 5.24 are based upon power readings at 365nm.

These experiments showed that exposure energies as high as 70-80mJ/cm² will result in shrinking of 30% or more. As was discussed in Section 4.2.2, the device was modeled based on the assumption of 30% shrinkage of the poly(NIPAAm) plug. Thus, all devices

were fabricated with exposure times consistent with an exposure energy of approximately 70mJ/cm².

Wavelength (nm)	Power (mW/cm ²)
405	1.738
365	2.13
320	0.783
220	4.57E-04

Table 5.1 – Light power emitted by the Spectroline Model EA-160 115V, 60Hz, 0.20A UV exposure system. Measurements taken with an optical powermeter at a distance of ~45mm

5.2.2.4 Channel Bonding

The channels are fabricated using Sylgard 184 PDMS molded off an SU-8 master. Typically, PDMS is bonded to glass by exposure to oxygen plasma using the methods discussed in Section 5.1. This process works because the hydroxide groups can react with the oxygen atoms on the surface of the glass (SiO₂). The process flow used for this device, however, requires bonding between SU-8 and PDMS. Because SU-8 does not contain the oxide groups found in glass, it cannot be covalently bonded to PDMS by exposure to oxygen plasma.

Temporary bonds are often formed between PDMS and glass simply by contacting the two together. The contact is generally energetically favorable, and the PDMS appears to “wet” the glass. This method was tried with the SU-8 devices. Unfortunately, the PDMS did not seal to the SU-8 surface due to the nonuniformity and roughness of the SU-8 surface.

PDMS has been widely used as a stamp for pattern transfer. Using this principle, adhesive was coated on a glass slide. The PDMS channels were then pressed onto the slide in order to cover their bottom surface with the adhesive. The channels were then aligned and pressed against the SU-8 devices, Unfortunately, this technique was unsuccessful primarily due to the presence of adhesive in the channel itself.

Finally, a mixture of PDMS was prepared with a ratio of ~20:1 base to curing agent. This resulted in a “tacky” PDMS mixture when cured. Its surface was somewhat sticky and allowed for attachment to the devices. While this bond is temporary, it will hold devices well enough for testing purposes.

Alignment of the channels to the devices can be difficult. While a variety of techniques were tried, the best method found was using a device like the one shown in Fig. 5.25. The device allows one to slide the PDMS channels in a vertical manner without distorting its shape. Furthermore, the inlet and outlet hypodermic tubes are fixed into the acrylic substrate allowing for easy attachment and detachment of tygon tubing without moving the PDMS channels or chip. After the channel is bonded, the device fabrication is complete and it is ready to be tested.

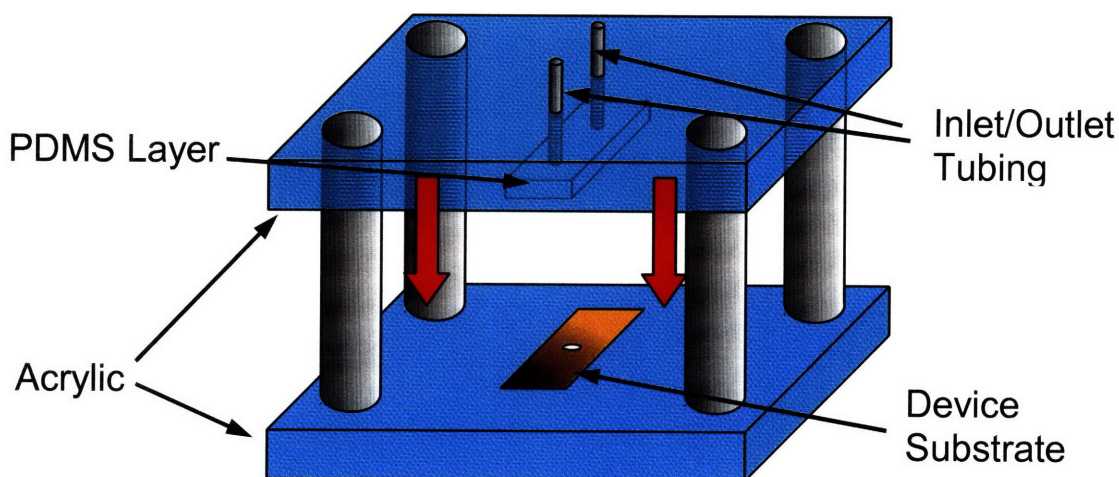


Fig. 5.25 – Alignment device. Top plate holds PDMS channels and allows for vertical movement.

5.2.3 Prepolymer Solutions

While the use of photopolymerizable NIPAAm solutions has been widely discussed throughout this chapter, it is not the only way to polymerize poly(NIPAAm) hydrogels. Polymerization of poly(NIPAAm) has been carried out using a variety of techniques. The other main technique makes use of a Reduction-Oxidation reaction. This technique

involves the use of an initiator and an accelerator along with the NIPAAm and crosslinking monomer (usually NMBA).

This technique was investigated for use with the current design. Multiple issues led to the quick realization that its use increased the complexity of the fabrication. The first issue was that, after polymerization, it appeared that there was remaining solution that did not polymerize. Since the design requires that the microwell is entirely full, this lack of polymerization was not acceptable. Furthermore, alignment was a significant issue. Every time a new tip is installed onto the printer, the camera and tip must be realigned to each other. This process is not simple and can take up to several hours to perform.

Nonetheless, this would be necessary since the process would require printing of one solution (likely a mixture of NIPAAm, NMBA, and TEMED, an accelerator) followed by a second (likely APS, the initiator). Overall precise control of solution chemistry added to these issues, and this technique was abandoned. While the photoinitiated solution has issues of its own (e.g. solvent drying, lack of lighting), its use seemed far less difficult than the RedOx method.

6. Experimental Results and Discussion

6.1 Original Design

Many of the results regarding the fabrication of the valves are discussed in the previous chapter. As was previously mentioned, the original design was abandoned due to the fact that, while it had low information content, it did not completely block the flow. This was due to the presence of oxygen near the channel walls that prevented polymerization.

A full table of devices sorted by their polymerization energies is shown in Appendix 1. A few general conclusions can be made from these experiments. The first is that, exposure energy affects the amount of shrinkage exhibited by the gel. This is also confirmed in the literature [48, 99, 100]. This is due to the fact that higher exposure energies result in higher crosslinking ratios and thus reduce the amount of shrinkage exhibited by the gel.

The second result worth noticing is the difference between the interval and continuous exposure methods. When using a continuous exposure, the gel is subjected to the UV light for the full duration without any stops. Under interval exposure, the full exposure time is broken up into intervals with waits of approximately fifteen seconds between each interval. This is commonly done in conventionally photolithography when patterning things such as thick resists or SU-8 where the exposure time is longer than conventional thin resists. The reason for doing this is to prevent the resist and wafer from heating up significantly when being polymerized. If this precaution is not performed, the resist can delaminate from the substrate due to stressed induced by a coefficient of thermal expansion mismatch.

Here, the interval exposure was employed again out of concerns regarding heating. The main concern was that if the polymerized portion was heated above the LCST that it may begin to shrink. Thus, when additional branches were polymerized around it, it would be

“stuck” in its shrunken form. Before the realization that oxygen inhibition was the limiting factor, it was believed that this was the reason why the hydrogel was not polymerized up to the edges of the channel. Obviously, this was not the case since the gap was as large if not larger in the interval exposure cases (Fig. 6.1). Furthermore, diffusion of the polymerized gel and solution during the interval waits resulted in less well defined edges to the gel. It turns out that the concern over shrinking during polymerization was unwarranted in the first place. As was discussed in Section 5.1, DMSO, the solvent in the prepolymer, is unlike water in that the swelling ratio seems to be far reduced. This is likely due to the lack of noncovalent interactions that are thought to be the cause of the volume phase transition in water.

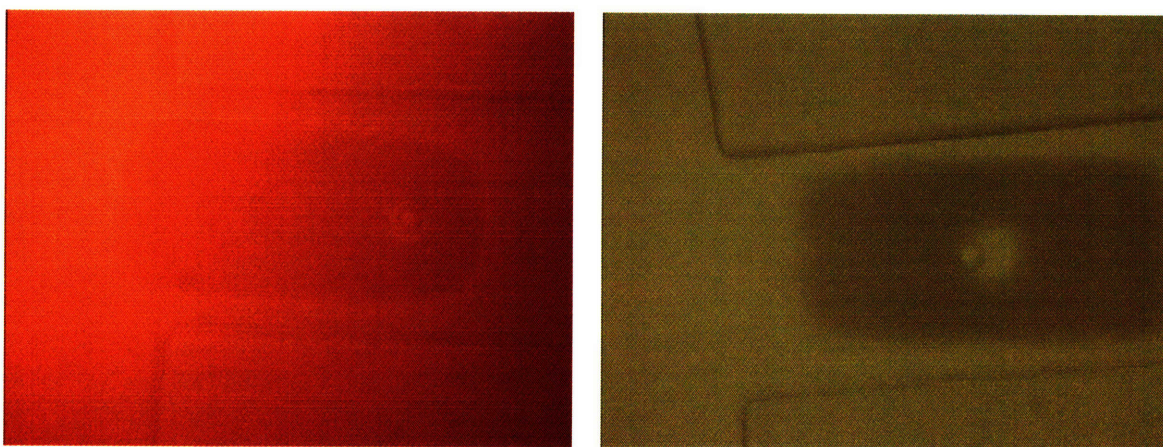


Fig. 6.1 – Continuous and interval exposures for 15sec: (a) continuous; (b) interval (5×3 sec). Lack of polymerization to the walls occurs in both cases. The edges of the gel in (b) are fuzzier due to diffusion during the waiting periods.

Ultimately, neither method resulted in an acceptable valve structure. While people have employed similar methods in the past, they have never done so in PDMS [5-7, 96, 101, 102]. While this design was the simplest, the ultimate inability to completely block flow deemed it unsuccessful.

6.2 Revised Design

Fabrication results of the final design were shown in the previous chapter along with results of the generalized polymerization tests. The issues of polymerization to the edges

have been eliminated in this design by filling wells that are not made of PDMS (Fig. 6.2). This ensures the absence of oxygen near the edges and fully polymerized gels.

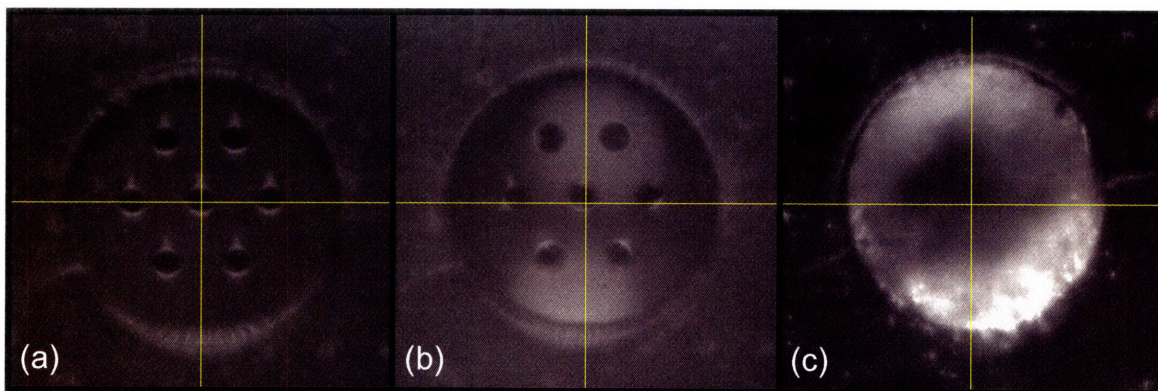


Fig. 6.2 – Polymerization of poly(NIPAAm) in microwell shows polymerization to the edges: (a) empty; (b) filled but unpolymerized; (c) after polymerization.

After the gels were polymerized, their phase transition response was measured using a variety of techniques. The first technique was to measure it optically using a horizontal camera. Results of this method are shown in Fig. 6.3. Unfortunately, it is difficult to discern the amount of shrinkage or surface profile even at a qualitative level from these images.

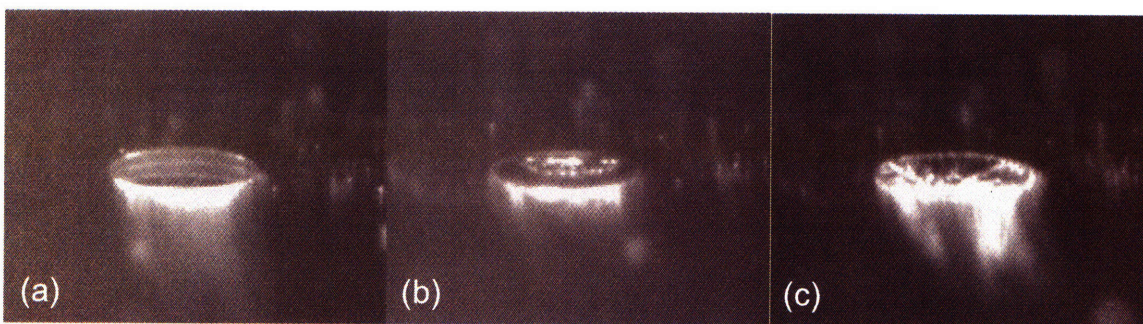
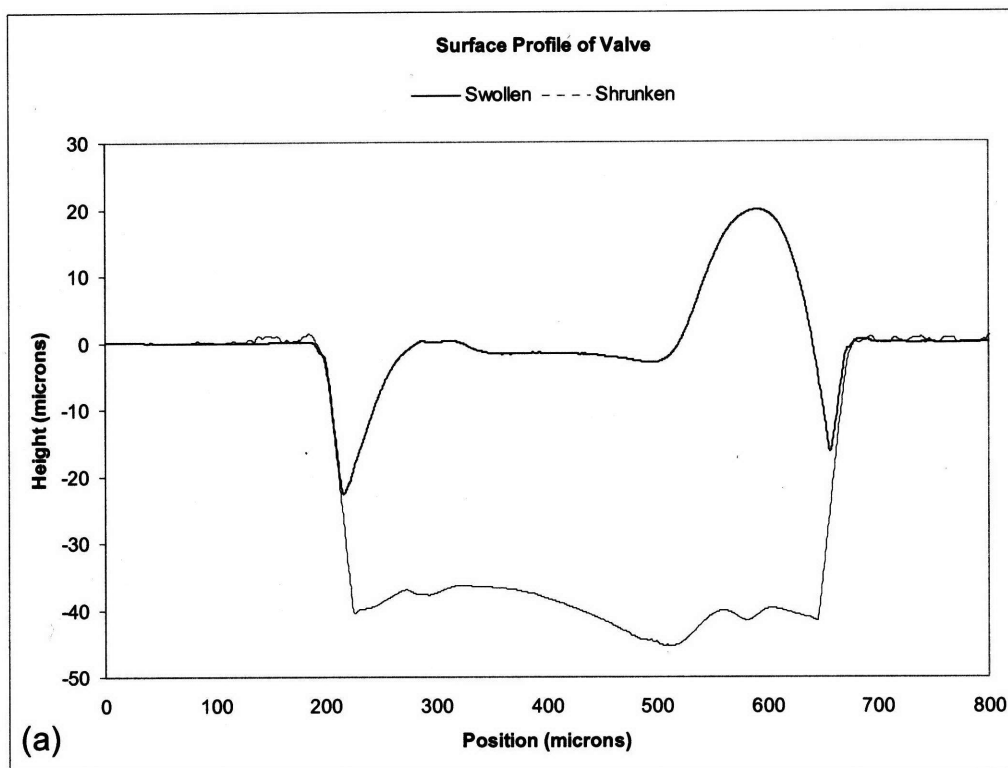


Fig. 6.3 – Optical imaging of shrinkage: (a) empty; (b) after polymerization and adding water; (c) after heating. Amount of shrinkage is difficult to discern from optical images.

Surface profilometry was used next to determine the profile of the gel prior to and after shrinking. First, a white-light interferometry 3D surface profiler (Zygo NewView) was used. While the profiler had no problems imaging empty wells, any areas containing poly(NIPAAm) could not be handled by the machine and no data was available for those

regions. This may have to do with the roughness of the surface and the resultant sporadic nature of the fringes during measurement.

Finally a contact profilometer (Tencor P-10) was used to determine the profile of the gel. The results of this profilometry are shown in Fig. 6.4 for three sample wells. The discrepancy in swollen heights is likely due to different amounts of filling and evaporation prior to polymerization. As was mentioned in Section 5.2.2.2, a lack of proper imaging combined with constant evaporation prevents one from knowing the exact profile of the prepolymer prior to polymerization.



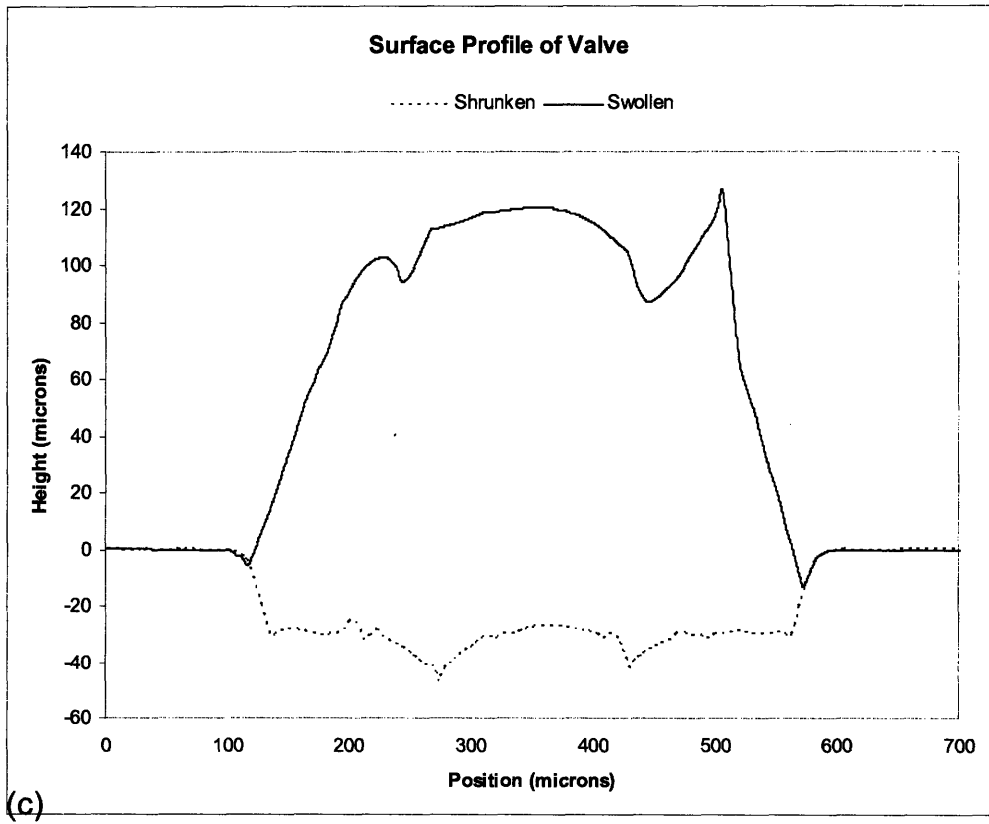
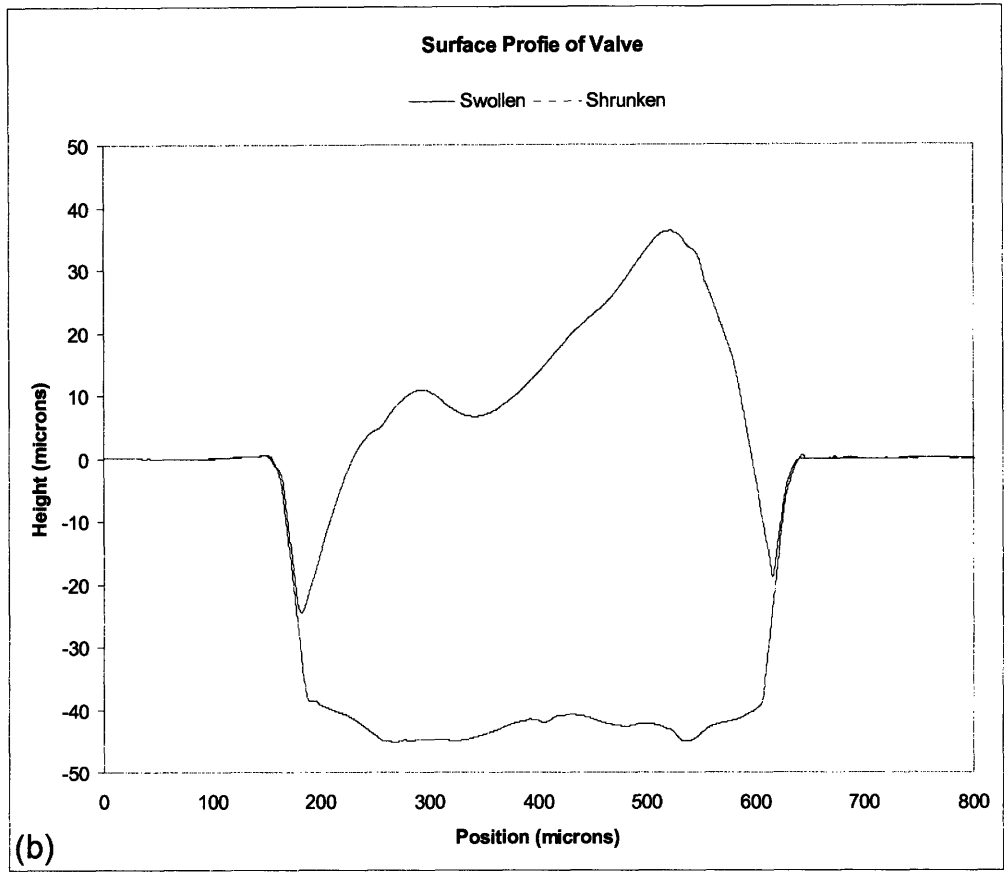


Fig. 6.4 – Surface profile for three sample wells before and after heating.

It is evident that the swollen hydrogel does not fill the well right at the top surface. The exact reason for this is not known, however, it should not be a concern. It is known that vertical compression of the gel results in radial expansion according to Poisson's ratio. This ensures that any small vacancies are filled when the PDMS channels are bonded on top of the device.

One possible cause for this separation at the top may be due to the interfacial energy between the prepolymer and SU-8. Fig. 6.5 shows the wetting of the prepolymer solution on SU-8, glass, and silicon. The contact angle between the SU-8 and prepolymer is much higher than the other two substrates. This hydrophobicity of the SU-8 may be the cause for the separation near the top surface of the wells and may also explain why it is possible to achieve gels whose upper surface is so far above the well despite its narrow diameter (Fig. 6.4(c)).

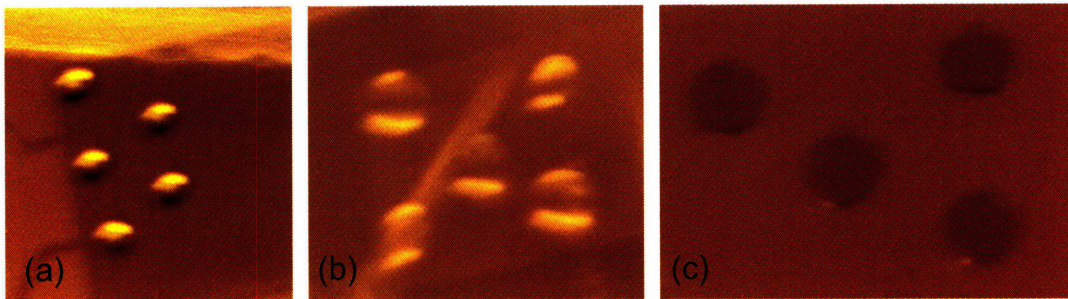


Fig. 6.5 – Surface wetting of NIPAAm prepolymer solution on (a) SU-8, (b) glass, and (c) silicon.

The final fabricated device is shown in Fig. 6.6. Channel alignment and bonding is one of the major challenges. Currently, this is performed by hand under a probe station. Depth of field issues along with poor positional control of the PDMS have resulted in difficulty in achieving this task with the accuracy prescribed by the design. Furthermore, because the PDMS mixture has such a small amount of curing agent, its stiffness appears to be significantly lower. Thus, after bonding the channel geometry can become warped from its original shape. The small amount of curing agent is necessary to make the PDMS “sticky” enough to bond to the SU-8 since covalent bonding is not an option between

these materials. Also, because this bond is not permanent, it is fairly weak and often lifts up when significant pressures are applied.

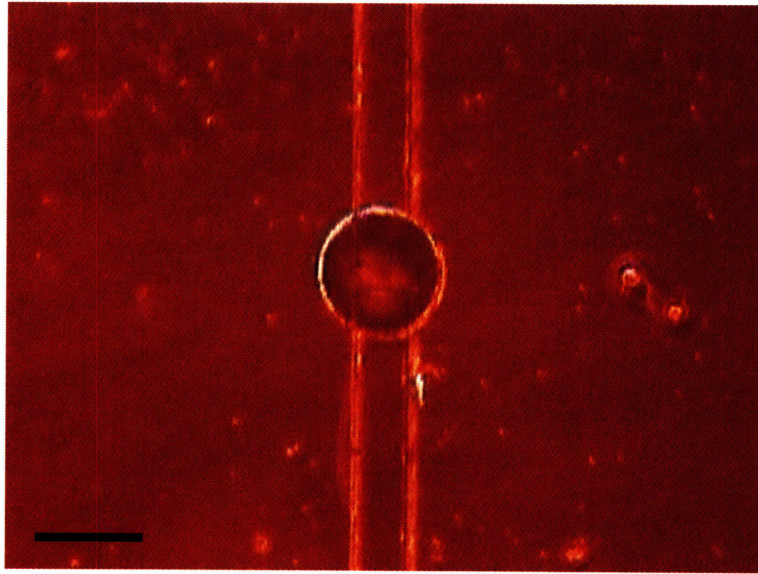


Fig. 6.6 – Final fabricated prototype. Scale bar is 200 μ m. This device has uncharacteristically good alignment of the channels to the well.

Another interesting point to note regarding the profilometry is that the majority of the shrinkage appears to occur in the vertical direction. No visible decreases in height near the edges of the well are visible in any of the surface scans (Fig. 6.4). One should note that the sloped sidewalls of the well are not actually sloped, but are an artifact of the scanning tip, which has a conical end. Confirmation of this lack of radial shrinkage can be acquired from optical images (Fig. 6.7). One possible cause of this is adhesion of the poly(NIPAAm) to either the SU-8 or gold surfaces. Thus, while the free surface can move up and down the sides cannot move due to the adhesion.

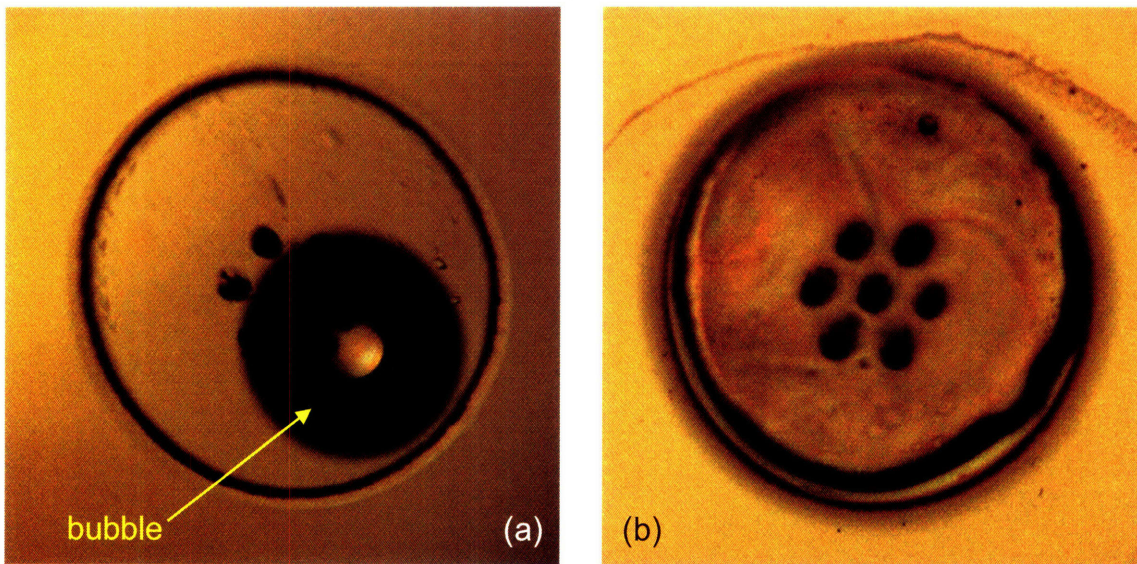


Fig. 6.7 – Despite vertical shrinkage demonstrated in the gels from profilometry, almost no radial shrinkage is visible: (a) swollen; (b) shrunken.

7. Future Work and Design Iterations

A variety of tasks still need to be performed to confirm the validity of this design and the models used to generate it. As for the current prototype, quantitative flowrate measurements must be made to confirm the CFD results. Additionally, measurements of pressure drops across the open valves and maximum allowable pressures for the closed valves need to be characterized.

7.1 Magnetic Nanoparticles

Some initial testing has been performed on the Fe_2O_3 nanoparticles (FerroTec EMG 705). The size of the nanoparticles was determined using Transmission Electron Microscopy (TEM) (Fig. 7.1). It was determined that diameters of the nanoparticles are on the order of approximately 15nm.

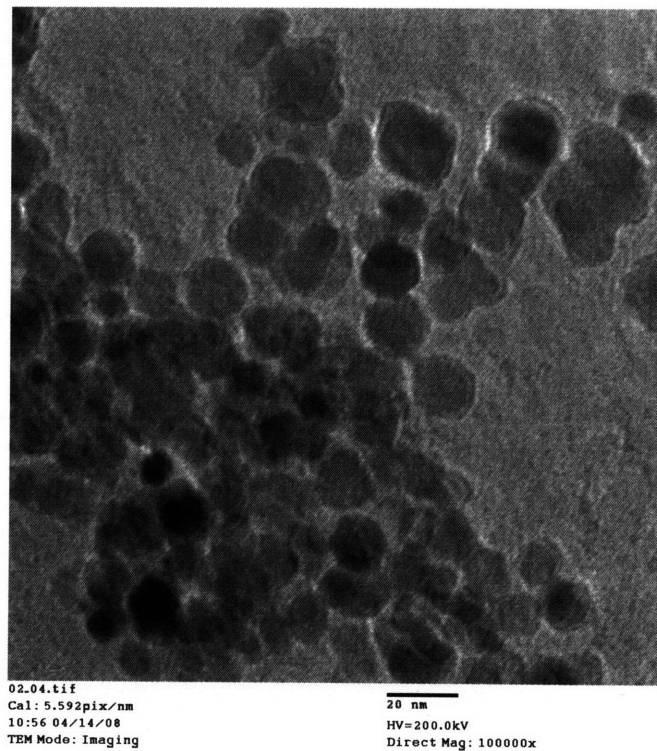


Fig. 7.1 – Iron-Oxide nanoparticles in NIPAAm prepolymer solution imaged using TEM.

Preliminary experiments regarding printing of the prepolymer solution have been performed. 2-3 vol% of nanoparticles was added to the previously-described prepolymer solution. While clogging of the tip and instabilities in printing occurred more readily than with the original solution, it was demonstrated that the particles could be printed successfully. These tests were performed by printing onto a glass slide and polymerizing using the same conditions as described in Section 5.2.2.3.

The next steps to complete the testing of the prototype are to print the solution with nanoparticles into the wells and test their response using an external magnetic coil. It would also be useful to characterize the amount of heating delivered by the nanoparticle as functions of concentration, time, and magnetic field frequency although this has been done to some extent in the literature [4, 61, 63, 64, 66, 72].

7.2 Alternative Fabrication Process

Fabrication of the prototype elucidated many problems that should be fixed when fabricating a second generation device. As was discussed in Section 5.2.2.1, careful control over the lateral to vertical etch rates is difficult to achieve using a metal hard mask. Even though the wafers were thoroughly cleaned prior to evaporation, the adhesion was still not perfect. A better approach is to use a polysilicon hard mask. For this process, the polysilicon would be deposited after cleaning using low pressure chemical vapor deposition (LPCVD). It can then be patterned using dry etching such as reactive ion etching with SF_6 . Since the silicon atoms can form covalent bonds with the oxygen on the surface of the glass, the adhesion is incredible good and the etch rates are essentially uniform in all directions.

The use of SU-8 also presented many problems in the fabrication. The nonuniformity of the layer across a wafer made it impossible to predict the height of any well without measuring it directly. This was a significant problem when printing because the volume

of prepolymer needed could not be predicted and thus the well had to be constantly monitored during filling. Furthermore, as was discussed in Section 6.2, the prepolymer has a much larger contact angle on SU-8 than on glass. This may have been the reason for the space between the poly(NIPAAm) and the well near the top surface. Finally, PDMS cannot be bonded to SU-8 using oxygen plasma. This makes it near impossible to achieve a good seal between the channels and the substrate.

To address the issues regarding SU-8, one can replace it with a second glass wafer. One can create a well in glass using a variety of techniques that include mechanical drilling, laser drilling, and wet etching. The use of polysilicon also aids in this process because the glass can then be anodically bonded to the polysilicon on the surface of the original wafer. This would fix all of the problems presented by the SU-8 since the surface would be uniform, has a smaller contact angle with the prepolymer, and can be covalently bonded to PDMS.

In the final device, one should include the planar MEMS magnetic coil that was mentioned in the design chapters. To make this coil, one can pattern and etch chromium and gold on the back of the wafer using the same method as was described in Chapter 5 for fabricating the hard mask for the anchor structures. Due to the small feature size of the coil, it would be necessary to use a chrome mask rather than a transparency as was used for all of the masks on the prototype.

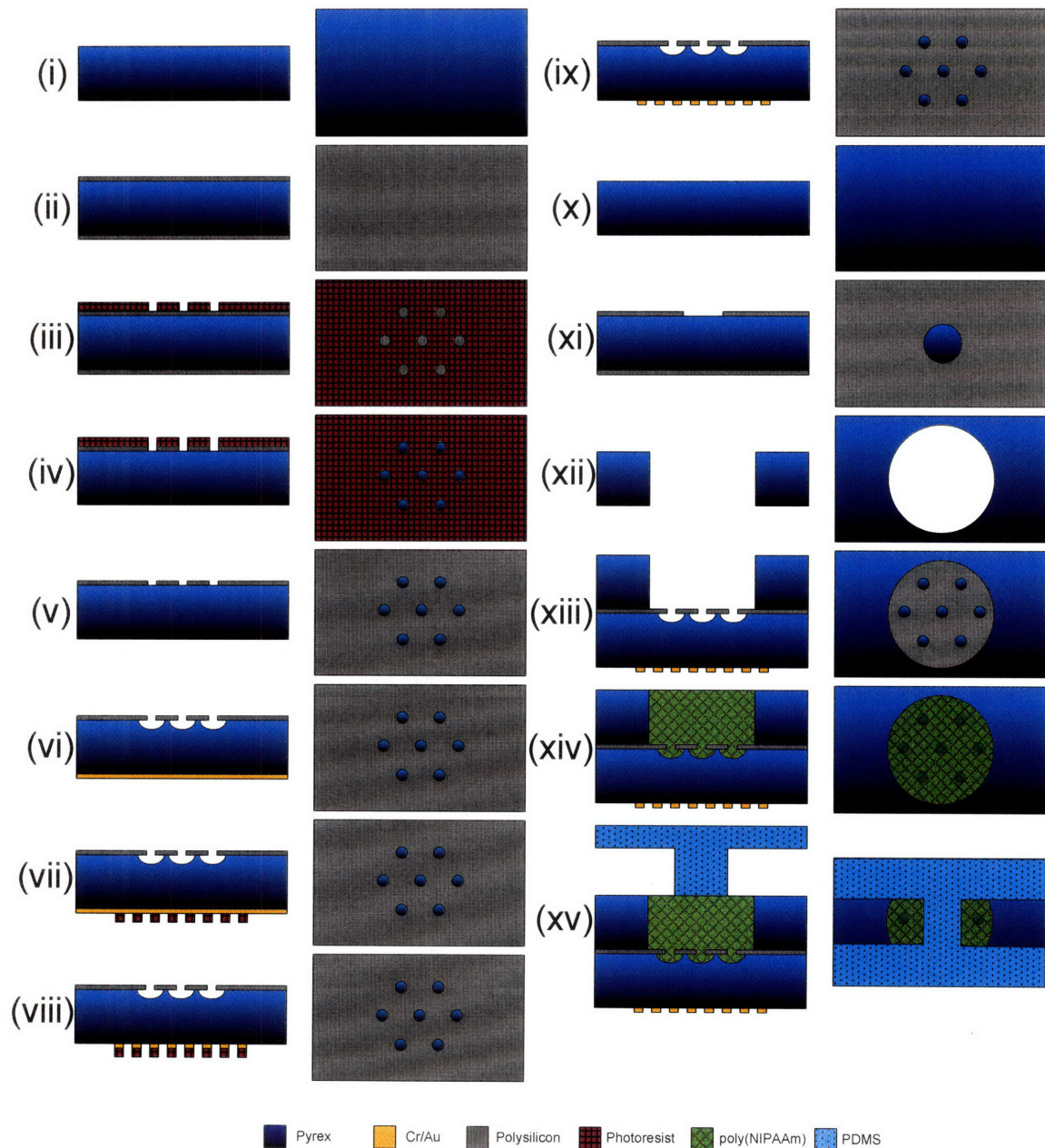


Fig. 7.2 – Revised fabrication process flow: (i) clean pyrex; (ii) LPCVD polySi; (iii) spin and pattern resist; (iv) RIE polySi from top and bottom; (v) ash resist and piranha clean; (vi) evaporate Cr and Au and wet etch glass with HF; (vii) spin and pattern resist; (viii) wet etch Cr and Au; (ix) ash resist; (x) clean separate pyrex wafer; (xi) LPCVD polySi and pattern as in steps (ii)-(v); (xii) etch through wafer; (xiii) anodically bond 2nd wafer to front of first; (xiv) print NIPAAm prepolymer and polymerize with UV light; (xv) bond PDMS channel (fabricated as before) by exposure to oxygen plasma.

Furthermore, because it would be desirable to have the anchor parts of the hydrogel shrink less than the body of the gel, it would be ideal to not have the magnetic nanoparticles in those areas, but have them everywhere else. To achieve this, one would first have to print the prepolymer without the nanoparticles into the bottom, and then

print the solution with them into the top. The current setup, however, makes this very difficult because separate tips must be used to for the two solutions. Since there is only one controller, the first tip has to be removed and the second one replaced before printing the solution with the nanoparticles. Unfortunately, when the new tip is installed, it has to be aligned to the camera. As previously mentioned this process can take hours, and during this time, the original solution would likely dry or evaporate leaving a residue like that shown in Fig. 5.21. Additionally, the current optics make it difficult to discern how filled the well is at any given time. It may be possible, however, to avoid these issues, by polymerizing immediately after the first solution is printed, and by improving the optics. The use of glass over SU-8 will also aid in making the filling volumes more predictable since the thickness is known.

A revised process flow based upon the aforementioned changes is shown in Fig. 7.2. In general it remains the same with the exceptions that the chromium-gold hard mask has been replaced with a LPCVD polysilicon. The well is now made out of a glass wafer that is anodically bonded to the polysilicon. The MEMS magnetic coil is added by evaporation of chromium and gold and wet etching them. Also, the PDMS is bonded to the glass by exposure to oxygen plasma.

In Chapter 3, it was mentioned that multiple smaller poly(NIPAAm) plugs should be used to increase the response time without increasing the pressure drop. To do this, one could have the channel branch into multiple parallel channels and cross over multiple wells. This could either be achieved by altering the PDMS channels or by etching the split channels into the second glass substrate.

7.3 Tests in Applications

Ultimately, it would be desirable to test the valves in true microfluidic chips that are used for some purpose. The immediately obvious application is drug delivery. This makes

sense because the ability to actuate the valves remotely by means of an external magnetic field would be a huge benefit to the field of implantable drug delivery chips.

Simple tests of this application could be performed in vitro to determine the validity of the chip. One could radioactively label a drug with something such as ^{125}I and fill an on chip reservoir with it. Using a gamma counter, diffusive transport could be measured in a bath when the valve is both opened and closed. Additionally, it may be possible to pressurize the reservoirs so that convective fluid flow could occur when the valves are opened. Eventually, these valves could be implemented in current drug delivery chip designs such as those designed by MicroCHIPS.

Benchtop chips used for things such as PCR, cell culture, protein assays, or other common microfluidic devices would be another area where the chips could be applied. Additionally, areas such as toxin detection and total analysis systems would be very useful areas for the valves to be tested since those are applications where field inspectors and doctors respectively may not have access to the external equipment required to use conventional microfluidic valves. Experiments of transport using these valves in typical devices in those areas may help to elucidate some of their benefits and shortcomings.

8. Conclusion

This thesis presented a new design for microfluidic valves using a thermosensitive hydrogel. The design should advance the field of microfluidics by providing solutions to many important problems including the reliance upon large external equipment, difficulty of fabrication by researchers and doctors unfamiliar with micromachining technologies, inability to actuate each valve individually, and the reliance upon mechanical or electrical interconnects. Using poly(NIPAAm) as an actuation mechanism, the valves operate by local heating of the gels. Patterning these valves on a separate substrate allows end-users to create their devices using single-layer soft lithography. The gels are printed into wells that contain anchor structures at the bottom to ensure predictable shrinking. Using the valve structures presented in this thesis, researchers no longer have to choose between difficulty of fabrication and reliance upon limited valve designs and external equipment. Furthermore, this thesis suggests the use of magnetic nanoparticles as a means of heating the gels for remote actuation, increased response time, and limited heating of the working fluid.

Prototypes of the valves designed in this thesis have been built. Demonstration of shrinking and swelling of the hydrogels in the wells has been performed. Results suggest that the valves should operate as intended. Measurements quantifying flow rates and pressure drops across the open valves still need to be performed. Additionally, the time response of the valves needs to be quantified along with the maximum pressure the closed valves can withstand.

Future iterations of the valves should have changes made to the fabrication process. These changes include replacing the SU-8 microwells with a more structurally sound material such as glass or silicon. Additionally, it is important that it is possible to bond PDMS to whatever material is chosen so that soft lithography can still be used for the channel designs. Integration of the proposed magnetic coil should also be performed in

conjunction with the use of iron-oxide nanoparticles. Measurements regarding actuation times and remote heating can then be performed.

Appendices

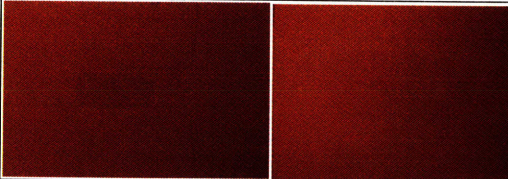

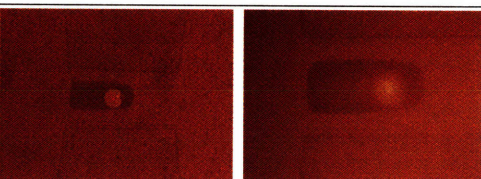

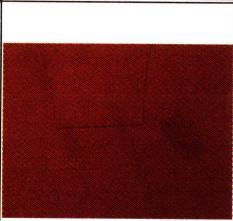
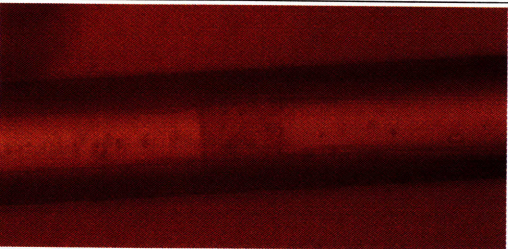

Appendix 1 – In-Channel Polymerization







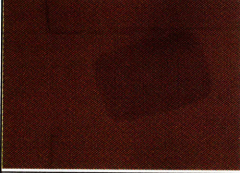

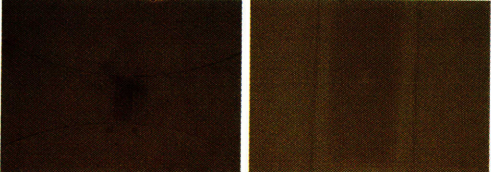
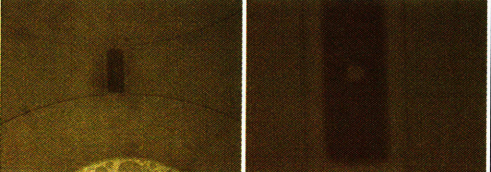
Appendix 2 – Fe₃O₄ Nanoparticle Data Sheet


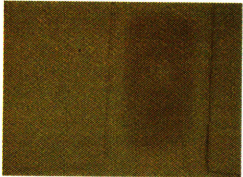
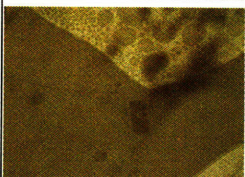

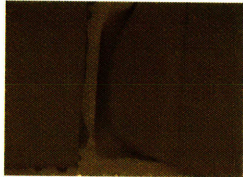

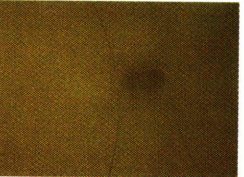

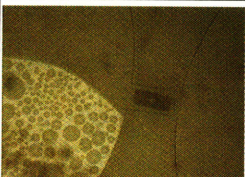


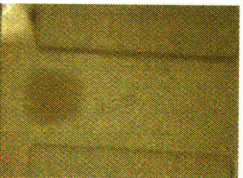
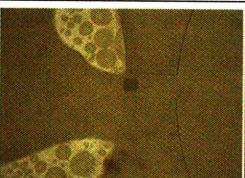
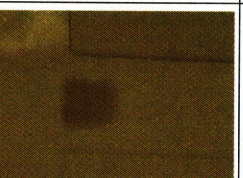
Appendix 3 – 2,2-Dimethoxy-2-phenylacetophenone Data

Appendix 4 – MJB3 Custom Chuck for Aligning PDMS/Glass Slide Structures

Appendix 1 – In-Channel Polymerization

Exp. Time	Exposure type	# Intervals	before heating	heating w/o water	heating w/ water	After heating and cooling
15s	Continuous	1				
15s	Continuous	1				
15s	Continuous In Glass Channel	1				
5s	Continuous	1				

7s	Continuous	1				
10s	Continuous	1				
15s	Continuous	1				
30s	Continuous	1				
6s	Interval	3				
6s	Interval	2				

7.5	Interval	3						
8s	Interval	4						
15	Interval	5						
20	Interval	10						

Appendix 2 – Fe₃O₄ Nanoparticle Data Sheet

Data table



EMG Ferrofluid

Name	carrier liquid	sat. magnetization J _s	viskosity @27°C	Ø Particle	beginning susceptibility	density @25°C	flash point	pH value	evaporation rate 1h @50°C	stock point	volume content Fe3O4	surfactant
		mT	mPa	nm		g /cm ³	°C			°C	Vol %	
EMG 308	water	6	5	10	0,25	1,05	0	8.9	0	0	1,1%	anionic
EMG 408	water	6	5	10	0,26	1,07	0	7	0	0	1,1%	anionic
EMG 507	water	10	2	10	0,38	1,15	0	8.9	0	0	1,8%	anionic
EMG 508	water	6	5	10	0,24	1,07	0	8.9	0	0	1,8%	anionic
EMG 509	water	3	5	10	0,12	1,02	0	8.9	0	0	0,5%	anionic
EMG 605	water	20	5	10	0,55	1,18	0	9.10	0	0	3,6%	cationic
EMG 607	water	10	2	10	0,36	1,1	0	9.10	0	0	1,8%	cationic
EMG 705	water	20	5	10	0,56	1,19	0	8.9	0	0	3,6%	anionic
EMG 707	water	10	5	10	0,36	1,1	0	8.9	0	0	1,8%	anionic
EMG 708	water	6	5	10	0,2	1,06	0	8.9	0	0	1,1%	anionic
EMG 805	water	20	3,5	10	0,49	1,19	0	6.7	0	0	3,6%	anionic
EMG 807	water	10	2	10	0,39	1,1	0	6.7	0	0	1,8%	anionic
EMG 900	synthetic isoparaffinic solvent	90	60	10	5,3	1,74	81	0	9,00%	-80	16,3%	anionic
EMG 901	synthetic isoparaffinic solvent	60	10	10	3	1,53	81	0	9,00%	-84	10,7%	anionic
EMG 905	synthetic isoparaffinic solvent	40	9	10	1,9	1,24	81	0	9,00%	-94	7,1%	anionic
EMG 908	water	6	5	10	0	0	0	0	0	0	0	
EMG 909	synthetic isoparaffinic solvent	20	6	10	0,8	1,02	81	0	9,00%	-94	3,6%	anionic
EMG 911	synthetic isoparaffinic solvent	10	4	10	0,38	0,89	81	0	9,00%	-94	1,7%	anionic

The particles consist of (Fe₃O₄) and are predominantly spherically. The particle diameter of 10nm (100Å) with standard types are average values of a log-normal size distribution. This average size can also be provided with 6nm on request. The half value width is with standard types about 5.6 nm and can be manufactured down to 3 nm on request.

The particles of water based Ferrofluid tend to agglomerate, therefore a shelf life of about half a year is the limit. Regularly ultrasonic applications may delay agglomerating, but do not fully compensate agglomeration. The shelf life is greatly extended by deep freezing. Dilution leads to increasing colloid instability, therefore only the needed volume of Ferrofluid should be diluted. Deionized or distilled water, as well as alcohol can be used for dilution of water based Ferrofluid.

Ferrofluids with different carriers (like cyclohexan, dodekan, heptan, toluen) can be provided with varying particle concentration.

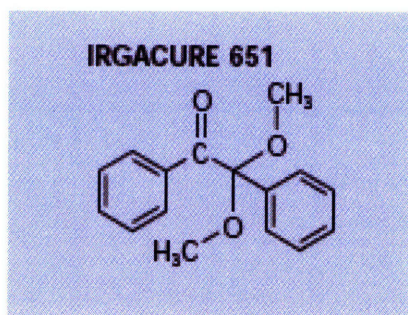
The dielectric number of all water based Ferrofluid is about 75.

Please note, that the notion "magnetization" in Gauss, named in most US literature (cgs-System) corresponds to the notion "Polarisation" according to DIN 1325 with the formula notion J and the unit Tesla.

Appendix 3 – 2,2-Dimethoxy-2-phenylacetophenone Data

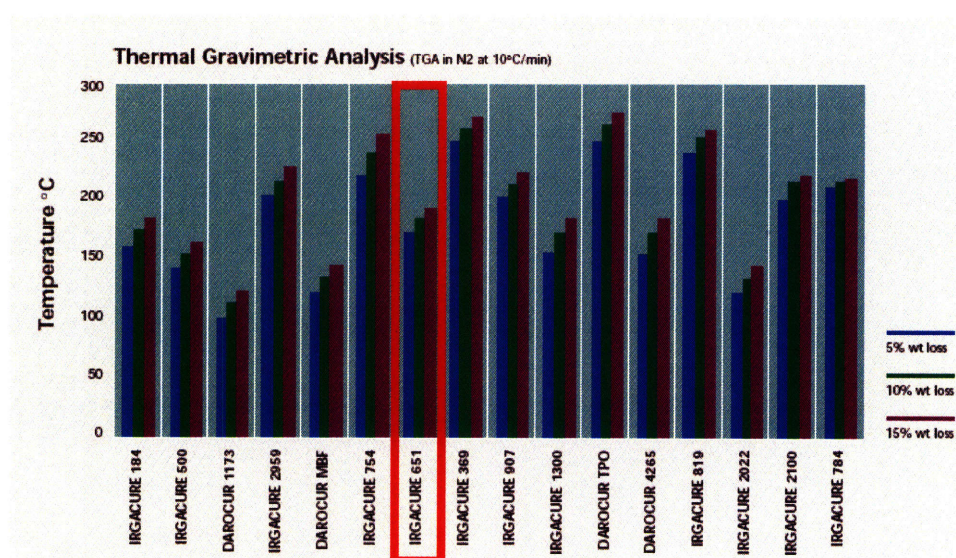
(From Ciba Specialty Chemicals: Photoinitiators for UV Curing: Key Products Selection Guide)

Typical physical properties Photoinitiators	Chemical class	Chemical Identity	Appearance	Freezing point (FP, °C) Melting point (MP, °C) Boiling point (BP, °C)	Specific gravity (water = 1)	UV/VIS Absorption peaks (nm) in methanol
IRGACURE 184	α-Hydroxyketone	1-Hydroxy-cyclohexyl-phenyl-ketone	white to off-white crystalline powder	MP 45–49 °C	1.1–1.2	246, 280, 333
IRGACURE 500	α-Hydroxyketone	IRGACURE 184 (50 wt%), Benzophenone (50 wt%)	clear, pale yellow liquid	FP < 0 °C recrystallization below 18 °C	1.1	250, 332
DAROCUR 1173	α-Hydroxyketone	2-Hydroxy-2-methyl-1-phenyl-1-propanone	clear, light yellow liquid	liquid at room temp. MP 4 °C, BP 80–81 °C	1.1	245, 280, 331
IRGACURE 2959	α-Hydroxyketone	2-Hydroxy-1-[4-(2-hydroxyethoxy)phenyl]-2-methyl-1-propanone	off-white powder	MP 86–90 °C	1.3	276
DAROCUR MBF	Phenylglyoxylate	Methylbenzoylformate	clear liquid	liquid at room temp. MP 17 °C BP 246–248 °C	1.2	255, 325
IRGACURE 754	Phenylglyoxylate	oxy-phenyl-acetic acid 2-[2 oxo-2 phenyl-acetoxy-ethoxy]-ethyl ester and oxy-phenyl-acetic 2-[2-hydroxy-ethoxy]-ethyl ester	light yellow liquid	liquid at room temp. MP < -22 °C	1.2	255, 325
IRGACURE 651	Benzylidimethyl-ketal	Alpha, alpha-dimethoxy-alpha-phenylacetophenone	white to light yellow powder	MP 64–67 °C	1.2	250, 340
IRGACURE 369	α-Aminoketone	2-Benzyl-2-(dimethylamino)-1-[4-(4-morpholinyl) phenyl]-1-butanone	slightly yellow powder	MP 110–114 °C	1.2	233, 324
IRGACURE 907	α-Aminoketone	2-Methyl-1-[4-(methylthio)phenyl]-2-(4-morpholinyl)-1-propanone	white to light beige powder	MP 70–75 °C	1.2	230, 304
IRGACURE 1300	α-Aminoketone	IRGACURE 369 (30 wt%) + IRGACURE 651 (70 wt%)	light yellow powder	MP 55–60 °C	1.2	251, 323
DAROCUR TPO	Mono Acyl Phosphine (MAPO)	Diphenyl (2,4,6-trimethylbenzoyl)-phosphine oxide	light yellow powder	MP 88–92 °C	1.2	295, 368, 380, 393

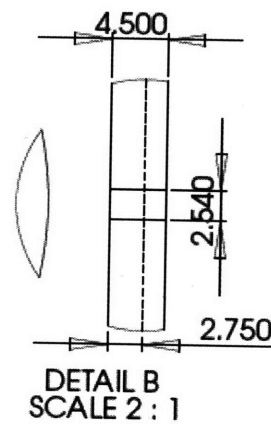
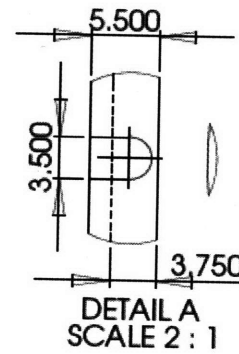
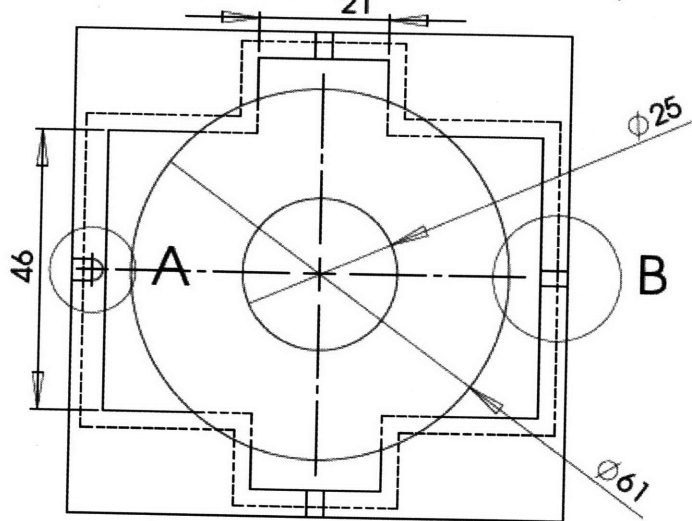
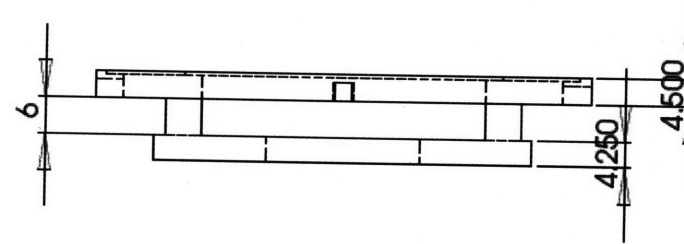
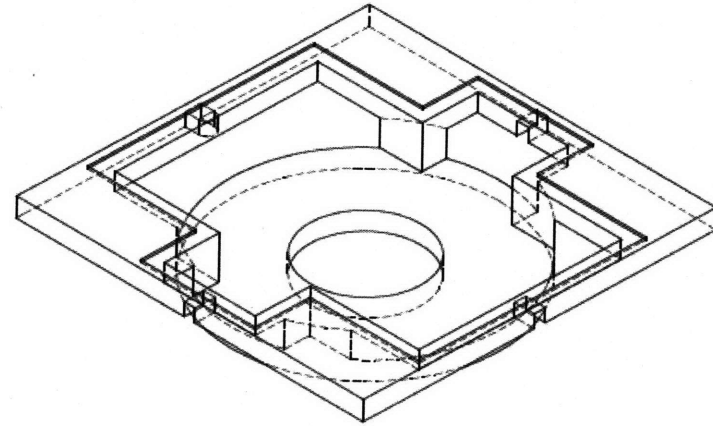
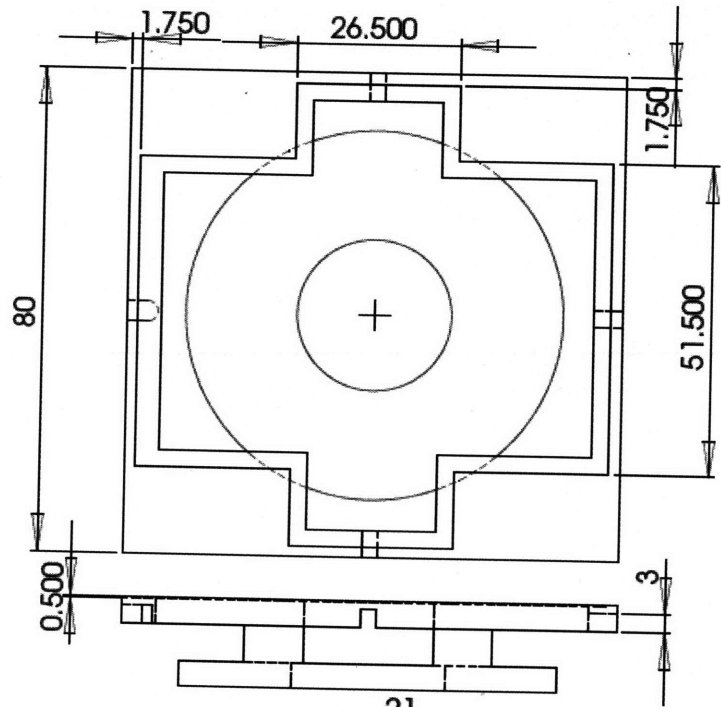


Photoinitiator (Solubility, Weight %)	Acetone	n-Butyl Acetate	IBOA	IDA	PEA	HDDA	TrPGDA	TMPTA	TMPEOTA	DAROCUR 1173
IRGACURE 184	> 50	> 50	> 50	> 50	> 50	> 50	> 50	> 50	> 50	> 50
IRGACURE 500	> 50	> 50	> 50	> 50	> 50	> 50	> 50	> 50	> 50	> 50
DAROCUR 1173	> 50	> 50	> 50	> 50	> 50	> 50	> 50	> 50	> 50	
IRGACURE 2959	19	3	5	5	5	10	20	5	5	35
DAROCUR MBF	> 50	> 50	> 50	> 50	> 50	> 50	> 50	> 50	> 50	> 50
IRGACURE 754	> 50	> 50	> 50	> 50	> 50	> 50	> 50	> 50	> 50	> 50
IRGACURE 651	> 50	> 50	40	30	> 50	40	25	> 50	45	> 50
IRGACURE 369	17	11	10	5	15	10	6	5	5	25
IRGACURE 907	> 50	35	35	25	45	35	22	25	20	> 50
IRGACURE 1300	> 50	45	> 50	35	> 50	> 50	35	25	25	> 50
DAROCUR TPO	47	25	15	7	34	22	16	14	13	> 50
DAROCUR 4265	> 50	> 50	> 50	> 50	> 50	> 50	> 50	> 50	> 50	> 50
IRGACURE 819	14	6	5	5	15	5	5	5	> 5	30
IRGACURE 2022	> 50	> 50	> 50	> 50	> 50	> 50	> 50	> 50	> 50	> 50
IRGACURE 2100	> 50	> 50	> 50	> 50	> 50	> 50	> 50	> 50	> 50	> 50
IRGACURE 784	30	10	5	NA	15	10	5	5	NA	7

IBOA = isobornyl acrylate; IDA = isodecyl acrylate; PEA = 2-phenoxyethyl acrylate; HDDA = hexane diol diacrylate; TrPGDA = tripropyleneglycol diacrylate; TMPTA = trimethylolpropane triacrylate; TMPEOTA = trimethylolpropane ethoxytriacrylate.



Appendix 4 – MJB3 Custom Chuck for Aligning PDMS/Glass Slide Structures (all units in mm)



References

1. Unger, M.A., et al., *Monolithic Microfabricated Valves and Pumps by Multilayer Soft Lithography*. Science, 2000. **288**(5463): p. 113-116.
2. Thorsen, T., S.J. Maerkl, and S.R. Quake, *Microfluidic Large-Scale Integration*. Science, 2002. **298**(5593): p. 580-584.
3. Santini, J.T., M.J. Cima, and R. Langer, *A controlled-release microchip*. Nature, 1999. **397**(6717): p. 335-338.
4. Dong, L. and H. Jiang, *Autonomous microfluidics with stimuli-responsive hydrogels*. Soft Matter, 2007. **3**(10): p. 1223-1230.
5. Eddington, D.T. and D.J. Beebe, *Flow control with hydrogels*. Advanced Drug Delivery Reviews, 2004. **56**(2): p. 199-210.
6. Beebe, D.J., et al., *Functional hydrogel structures for autonomous flow control inside microfluidic channels*. Nature, 2000. **404**(6778): p. 588-590.
7. Wang, J., et al., *Self-Actuated, Thermo-Responsive Hydrogel Valves for Lab on a Chip*. Biomedical Microdevices, 2005. **7**(4): p. 313-322.
8. Figeys and Pinto, *Lab-on-a-chip: a revolution in biological and medical sciences*. Analytical Chemistry, 2000. **72**(9): p. 330A-335A-330A-335A.
9. Manz, A., et al., *Planar chips technology for miniaturization and integration of separation techniques into monitoring systems : Capillary electrophoresis on a chip*. Journal of Chromatography A, 1992. **593**(1-2): p. 253-258.
10. Whitesides, G.M., *The origins and the future of microfluidics*. Nature, 2006. **442**(7101): p. 368-373.
11. Ng, J.M.K., et al., *Components for integrated poly(dimethylsiloxane) microfluidic systems*. Electrophoresis, 2002. **23**(20): p. 3461-3473.
12. Whitesides, G.M. and A.D. Stroock, *Flexible Methods for Microfluidics*. Physics Today, 2001. **54**(6): p. 42-48.
13. Xia, Y. and G.M. Whitesides, *Soft Lithography*. Annual Review of Materials Science, 1998. **28**(1): p. 153-153.
14. Zhao, X.-M., Y. Xia, and G.M. Whitesides, *Soft lithographic methods for nano-fabrication*. Journal of Materials Chemistry, 1997. **7**(7): p. 1069-1074.
15. Kopp, M.U., A.J.d. Mello, and A. Manz, *Chemical Amplification: Continuous-Flow PCR on a Chip*. Science, 1998. **280**(5366): p. 1046-1048.
16. Atencia, J. and D.J. Beebe, *Controlled microfluidic interfaces*. Nature, 2005. **437**(7059): p. 648-655.
17. Yager, P., et al., *Microfluidic diagnostic technologies for global public health*. Nature, 2006. **442**(7101): p. 412-418.
18. Thorsen, T., et al., *Dynamic Pattern Formation in a Vesicle-Generating Microfluidic Device*. Physical Review Letters, 2001. **86**(18): p. 4163-4163.
19. Anna, S.L., N. Bontoux, and H.A. Stone, *Formation of dispersions using 'flow focusing' in microchannels*. Applied Physics Letters, 2003. **82**(3): p. 364-366.
20. Okushima, S., et al., *Controlled Production of Monodisperse Double Emulsions by Two-Step Droplet Breakup in Microfluidic Devices*. Langmuir, 2004. **20**(23): p. 9905-9908.
21. Dertinger, S.K.W., et al., *Generation of Gradients Having Complex Shapes Using Microfluidic Networks*. Analytical Chemistry, 2001. **73**(6): p. 1240-1246.

22. Shikida, M., et al., *Electrostatically driven gas valve with high conductance*. *Microelectromechanical Systems, Journal of*, 1994. **3**(2): p. 76-80.
23. Fu, C., Z. Rummeler, and W. Schomburg, *Magnetically driven micro ball valves fabricated by multilayer adhesive film bonding*. *Journal of Micromechanics and Microengineering*, 2003. **13**(4): p. S96-S102-S96-S102.
24. Papavasiliou, A.P., D. Liepmann, and A.P. Pisano, *Electrolysis-Bubble Actuated Gate Valve*, in *Technical Digest of the IEEE Solid State Sensor and Actuator Workshop*. 2000: Hilton Head Island, SC. p. 48-51.
25. Li, H.Q., et al., *Fabrication of a high frequency piezoelectric microvalve*. *Sensors and Actuators A: Physical*, 2004. **111**(1): p. 51-56.
26. Takei, G., et al., *Tuning microchannel wettability and fabrication of multiple-step Laplace valves*. *Lab on a Chip*, 2007. **7**(5): p. 596-602.
27. Nguyen, N.-T. and S.T. Wereley, *Fundamentals And Applications of Microfluidics, Second Edition*. 2006: Artech House Publishers. 497.
28. Park, J.-M., et al., *Multifunctional microvalves control by optical illumination on nanoheaters and its application in centrifugal microfluidic devices*. *Lab on a Chip*, 2007. **7**(5): p. 557-564.
29. Gui, L. and J. Liu, *Ice valve for a mini/micro flow channel*. *Journal of Micromechanics and Microengineering*, 2004. **14**(2): p. 242-246.
30. Fluidigm. *Fluidigm Nanoflex Technology*. [cited; Available from: <http://www.fluidigm.com/nanoflex.htm>].
31. Chilkoti, A., et al., *Targeted drug delivery by thermally responsive polymers*. *Advanced Drug Delivery Reviews*, 2002. **54**(5): p. 613-630.
32. Doorty, K.B., et al., *Poly(N-isopropylacrylamide) co-polymer films as potential vehicles for delivery of an antimetabolic agent to vascular smooth muscle cells*. *Cardiovascular Pathology*, 2003. **12**(2): p. 105-110.
33. Khademhosseini, A., et al., *Tissue Engineering Special Feature: Microscale technologies for tissue engineering and biology*. *Proceedings of the National Academy of Sciences*, 2006. **103**(8): p. 2480-2487.
34. Peppas, N.A., et al., *Hydrogels in Biology and Medicine: From Molecular Principles to Bionanotechnology*. *Advanced Materials*, 2006. **18**(11): p. 1345-1360.
35. Needham, D. and M.W. Dewhurst, *The development and testing of a new temperature-sensitive drug delivery system for the treatment of solid tumors*. *Advanced Drug Delivery Reviews*, 2001. **53**(3): p. 285-305.
36. Peppas, N.A., et al., *Hydrogels in pharmaceutical formulations*. *European journal of pharmaceuticals and biopharmaceutics : official journal of Arbeitsgemeinschaft für Pharmazeutische Verfahrenstechnik e.V*, 2000. **50**(1): p. 27-46.
37. Robert Langer, N.A.P., *Advances in biomaterials, drug delivery, and bionanotechnology*. *AICHE Journal*, 2003. **49**(12): p. 2990-3006.
38. Roos, A., et al., *Development of a temperature sensitive drug release system for polymeric implant devices*. *Biomaterials*, 2003. **24**(24): p. 4417-4423.
39. Sershen, S. and J. West, *Implantable, polymeric systems for modulated drug delivery*. *Advanced Drug Delivery Reviews*, 2002. **54**(9): p. 1225-1235.
40. Zhang, L., T. Xu, and Z. Lin, *Controlled release of ionic drug through the positively charged temperature-responsive membranes*. *Journal of Membrane Science*, 2006. **281**(1-2): p. 491-499.
41. Tanaka, T. and D.J. Fillmore, *Kinetics of swelling of gels*. *The Journal of Chemical Physics*, 1979. **70**(3): p. 1214-1218.

42. Matsuo, E.S. and T. Tanaka, *Patterns in shrinking gels*. Nature, 1992. **358**(6386): p. 482-485.
43. Hirokawa, Y. and T. Tanaka, *Volume phase transition in a nonionic gel*. The Journal of Chemical Physics, 1984. **81**(12): p. 6379-6380.
44. Feil, H., et al., *Effect of comonomer hydrophilicity and ionization on the lower critical solution temperature of N-isopropylacrylamide copolymers*. Macromolecules, 1993. **26**(10): p. 2496-2500.
45. Flory, P.J., *Principles of Polymer Chemistry*. 1953: Cornell University Press. 688.
46. Hino, T. and J.M. Prausnitz, *Molecular thermodynamics for volume-change transitions in temperature-sensitive polymer gels*. Polymer, 1998. **39**(14): p. 3279-3283.
47. Hirotsu, S., Y. Hirokawa, and T. Tanaka, *Volume-phase transitions of ionized N-isopropylacrylamide gels*. The Journal of Chemical Physics, 1987. **87**(2): p. 1392-1395.
48. Hitoshi Kubota, A.F., *Photopolymerization synthesis of poly(N-isopropylacrylamide) hydrogels*. Journal of Applied Polymer Science, 1997. **65**(7): p. 1313-1318.
49. Hua Li, X.W., *Multiphysics Modelling of Volume Phase Transition of Ionic Hydrogels Responsive to Thermal Stimulus*. Macromolecular Bioscience, 2005. **5**(9): p. 904-914.
50. Lee, K.K., et al., *Pressure-dependent phase transitions in hydrogels*. Chemical Engineering Science, 1990. **45**(3): p. 766-767.
51. Monika M. Prange, H.H.H., *Thermodynamics of aqueous systems containing hydrophilic polymers or gels*. AIChE Journal, 1989. **35**(5): p. 803-813.
52. Otake, K., et al., *A new model for the thermally induced volume phase transition of gels*. The Journal of Chemical Physics, 1989. **91**(2): p. 1345-1350.
53. Otake, K., et al., *Thermal analysis of the volume phase transition with N-isopropylacrylamide gels*. Macromolecules, 1990. **23**(1): p. 283-289.
54. Ringsdorf, H., J. Venzmer, and F.M. Winnik, *Fluorescence studies of hydrophobically modified poly(N-isopropylacrylamides)*. Macromolecules, 1991. **24**(7): p. 1678-1686.
55. Schild, H.G., *Poly(N-isopropylacrylamide): experiment, theory and application*. Progress in Polymer Science, 1992. **17**(2): p. 163-249.
56. Schild, H.G. and D.A. Tirrell, *Microcalorimetric detection of lower critical solution temperatures in aqueous polymer solutions*. J. Phys. Chem., 1990. **94**(10): p. 4352-4356.
57. Shibayama, M., et al., *Simple Scaling Rules on Swollen and Shrunken Polymer Gels*. Macromolecules, 1997. **30**(23): p. 7307-7312.
58. Shibayama, M. and T. Tanaka, *Volume phase transition and related phenomena of polymer gels, in Responsive Gels: Volume Transitions I*. 1993. p. 1-62.
59. Shirota, H., N. Endo, and K. Horie, *Volume phase transition of polymer gel in water and heavy water*. Chemical Physics, 1998. **238**(3): p. 487-494.
60. You Han Bae, T.O., *Temperature dependence of swelling of crosslinked poly(N,N'-alkyl substituted acrylamides) in water*. Journal of Polymer Science Part B: Polymer Physics, 2003. **28**(6): p. 923-936.
61. Wijaya, A., et al. *Selective heating of multiple nanoparticles*. in 2005 MRS Fall Meeting, Nov 28-Dec 2 2005. 2005: Materials Research Society, Warrendale, PA 15086, United States.
62. Berry, C.C. and A.S.G. Curtis, *Functionalisation of magnetic nanoparticles for applications in biomedicine*. Journal of Physics D: Applied Physics, 2003. **36**(13): p. R198-R206-R198-R206.
63. Kato, N., Y. Takizawa, and F. Takahashi, *Magnetically Driven Chemomechanical Device with Poly(N-isopropylacrylamide) Hydrogel Containing $\{\gamma\}$ -Fe₂O₃*. Journal of Intelligent Material Systems and Structures, 1997. **8**(7): p. 588-595.
64. Lao, L.L. and R.V. Ramanujan, *Magnetic and hydrogel composite materials for hyperthermia applications*. Journal of Materials Science: Materials in Medicine, 2004. **15**(10): p. 1061-1064.

65. Qiang, Y., et al., *Iron/iron oxide core-shell nanoclusters for biomedical applications*. Journal of Nanoparticle Research, 2006. **8**(3): p. 489-496.
66. Wakamatsu, H., et al., *Preparation and characterization of temperature-responsive magnetite nanoparticles conjugated with N-isopropylacrylamide-based functional copolymer*. Journal of Magnetism and Magnetic Materials, 2006. **302**(2): p. 327-333.
67. Donald J. Buckley, M.B., *The swelling of polymer systems in solvents. II. Mathematics of diffusion*. Journal of Polymer Science, 1962. **56**(163): p. 175-188.
68. Gehrke, S., *Synthesis, equilibrium swelling, kinetics, permeability and applications of environmentally responsive gels*, in *Responsive Gels: Volume Transitions II*. 1993. p. 81-144.
69. Truskey, G.A., F. Yuan, and D.F. Katz, *Transport Phenomena in Biological Systems*. 2004: Prentice Hall. 816.
70. Rosensweig, R.E., *Heating magnetic fluid with alternating magnetic field*. Journal of Magnetism and Magnetic Materials, 2002. **252**: p. 370-374.
71. Fannin, P.C. and S.W. Charles, *On the calculation of the Neel relaxation time in uniaxial single-domain ferromagnetic particles*. Journal of Physics D: Applied Physics, 1994. **27**(2): p. 185.
72. Khushrushahi, S., *A Quantitative Design and Analysis of Magnetic Nanoparticle Heating Systems*, in *Electrical Engineering*. 2005, Massachusetts Institute of Technology: Cambridge. p. 89.
73. Popplewell, J., R.E. Rosensweig, and R.J. Johnston, *Magnetic field induced rotations in ferrofluids*. Magnetics, IEEE Transactions on, 1990. **26**(5): p. 1852-1854.
74. Incropera, F.P., et al., *Fundamentals of Heat and Mass Transfer*. 2006: Wiley. 1024.
75. Senturia, S.D., *Microsystem Design*. 2004: Springer. 720.
76. Tilmans, H.A.C., *Equivalent circuit representation of electromechanical transducers: I. Lumped-parameter systems*. Journal of Micromechanics and Microengineering, 1996(1): p. 157.
77. Tilmans, H.A.C., *Equivalent circuit representation of electromechanical transducers: II. Distributed-parameter systems*. Journal of Micromechanics and Microengineering, 1997(4): p. 285.
78. Kinsler, L.E., et al., *Fundamentals of Acoustics*. 1999: Wiley. 560.
79. Beebe, D.J., G.A. Mensing, and G.M. Walker, *Physics and applications of microfluidics in biology*. Annual Review of Biomedical Engineering, 2002. **4**: p. 261-286.
80. Ward, I.M., *Mechanical Properties of Solid Polymers*. 1983: John Wiley & Sons Inc. 492.
81. Fung, Y.C., *Biomechanics: Mechanical Properties of Living Tissues*. 1993: Springer. 568.
82. Darling, E.M., S. Zauscher, and F. Guilak, *Viscoelastic properties of zonal articular chondrocytes measured by atomic force microscopy*. Osteoarthritis and cartilage / OARS, Osteoarthritis Research Society, 2006. **14**(6): p. 571-579.
83. Decker, C. and A.D. Jenkins, *Kinetic approach of oxygen inhibition in ultraviolet-and laser-induced polymerizations*. Macromolecules, 1985. **18**(6): p. 1241-1244.
84. Dendukuri, D., et al., *Continuous-flow lithography for high-throughput microparticle synthesis*. Nat Mater, 2006. **5**(5): p. 365-369.
85. Dendukuri, D., et al., *Stop-flow lithography in a microfluidic device*. Lab on a Chip, 2007. **4**(7): p. 818-28.
86. Pregibon, D.C., M. Toner, and P.S. Doyle, *Multifunctional Encoded Particles for High-Throughput Biomolecule Analysis*. Science, 2007. **315**(5817): p. 1393-1396.
87. Deen, W.M., *Analysis of Transport Phenomena*. 1998: Oxford University Press, USA. 624.
88. Einstein, A., *Investigations on the Theory of Brownian Movement*. Ann. der Physik, 1905. **17**: p. 549-549.

89. Li, J. and P.W. Carr, *Accuracy of Empirical Correlations for Estimating Diffusion Coefficients in Aqueous Organic Mixtures*. Analytical Chemistry, 1997. **69**(13): p. 2530-2536.
90. Suh, N.P., *Axiomatic Design: Advances and Applications*. 2001: Oxford University Press, USA. 528.
91. Chandler, D., *Introduction to Modern Statistical Mechanics*. 1987: Oxford University Press, USA. 288.
92. Boal, D., *Mechanics of the Cell*. 2002: Cambridge University Press. 406.
93. Dill, K.A., *Molecular Driving Forces: Statistical Thermodynamics in CHEMISTRY & Biology*. 2002: Routledge. 704.
94. Benjamin, P. and C. Weaver, *The Adhesion of Evaporated Metal Films on Glass*. Proceedings of the Royal Society of London. Series A, Mathematical and Physical Sciences, 1961. **261**(1307): p. 516-531.
95. Lin, H.H. and Y.L. Cheng, *In-Situ Thermoreversible Gelation of Block and Star Copolymers of Poly(ethylene glycol) and Poly(N-isopropylacrylamide) of Varying Architectures*. Macromolecules, 2001. **34**(11): p. 3710-3715.
96. Dong, L., et al., *Adaptive liquid microlenses activated by stimuli-responsive hydrogels*. Nature, 2006. **442**(7102): p. 551-554.
97. Payer, K., *Wet Etching of Glass with HF*. 2008.
98. *The Merck Index*. 11th ed. 1989.
99. Hoffmann, J., et al., *Photopatterning of thermally sensitive hydrogels useful for microactuators*. Sensors and Actuators A: Physical, 1999. **77**(2): p. 139-144.
100. Kuckling, D., M.E. Harmon, and C.W. Frank, *Photo-Cross-Linkable PNIPAAm Copolymers. I. Synthesis and Characterization of Constrained Temperature-Responsive Hydrogel Layers*. Macromolecules, 2002. **35**(16): p. 6377-6383.
101. Abhishek K Agarwal, D.J.B. and J. Hongrui, *Integration of polymer and metal microstructures using liquid-phase photopolymerization*. Journal of Micromechanics and Microengineering, 2006. **16**(2): p. 332.
102. Kim, D. and D.J. Beebe, *Hydrogel-based reconfigurable components for microfluidic devices*. Lab on a Chip, 2007. **7**(2): p. 193-198.